The Thesis Committee for Andrew Marshall Davidson
Certifies that this is the approved version of the following thesis:

Magnetic Induction Heating of Superparamagnetic Nanoparticles for Applications in the Energy Industry

APPROVED BY
SUPERVISING COMMITTEE:

Supervisor: _____
Steven L. Bryant

Co-Supervisor: _____
Chun Huh

Magnetic Induction Heating of Superparamagnetic Nanoparticles for Applications in the Energy Industry

by

Andrew Marshall Davidson, B.S.Ch.E.

Thesis

Presented to the Faculty of the Graduate School of

The University of Texas at Austin

in Partial Fulfillment

of the Requirements

for the Degree of

Master of Science in Engineering

The University of Texas at Austin

December 2012

Acknowledgements

I would like to thank Dr. Bryant and Dr. Huh for their unwavering support and enthusiasm throughout this research endeavor. Our discussions of research ideas and results showed me an aspect of higher intellectual thought that I had previously been unexposed to. They showed me that sometimes the road less traveled is riddled with challenges, but rich in reward. I would also like to thank Glen Baum for his advice and expertise in setting up my research apparatus, SeungYup Ryoo for sharing his expertise in electromagnetic experimental systems, Ki Yool Yoon for his aid in analytical testing and imaging of samples, Amirreza Rahmani for his invaluable support throughout the COMSOL modeling work and electromagnetic theoretical explanations, and Dr. Milner for lending his advice, time, and experimental equipment.

Abstract

Magnetic Induction Heating of Superparamagnetic Nanoparticles for Applications in the Energy Industry

Andrew Marshall Davidson, M.S.E.

The University of Texas at Austin, 2012

Supervisors: Steven Bryant and Chun Huh

A novel method of delivering thermal energy efficiently for flow assurance and for improved heavy oil production/transport is described. The method, an improved form of magnetic induction heating, uses superparamagnetic nanoparticles that generate heat locally when exposed to a high frequency magnetic field oscillation, via a process known as Neel relaxation. This concept is currently used in biomedicine to locally heat and ablate cancerous tissues.

Dependence of the rate of heat generation by commercially available, single-domain Fe_3O_4 nanoparticles of ~10 nm size, on the magnetic field strength and frequency was quantified. Experiments were conducted for nanoparticles dispersed in water, in hydrocarbon liquid, and embedded in a thin, solid film dubbed "nanopaint". For a stationary fluid heat generation increases linearly with loading of nanoparticles. The rate of heat transfer from the nanopaint to a flowing fluid was up to three times greater than the heat transfer rate to a static fluid. Dispersion models indicated that the thermal

conductivity of the dispersing fluid did not greatly influence the heat transfer results, whereas differences in size between hydrophilic and hydrophobic nanoparticles did. The model of static fluid in a nanopainted tube verified that the nanoparticle loading in the paint was ~30wt% and the nanopaint thickness was 600 μm. The model of flowing fluid in a nanopainted tube showed that internal mixing in the system, even at laminar flow rates, improved heat transfer to the center of the flowing fluid. A waveguide model verified the feasibility of using steel hydrocarbon transport pipelines as a means to guide electromagnetic energy to target heating locations along the pipeline if the energy is transmitted at frequencies above the cutoff frequency.

Heating of nanopaint with external magnetic field application has immediate potential impact on oil and gas sector, because such coating could be applied to inner surfaces of pipelines and production facilities. A nanoparticle dispersion could also be injected into the reservoir zone or gravel pack near the production well, so that a thin, adsorbed layer of nanoparticles is created on pore walls. With localized inductive heating of those surfaces, hydrate formation or wax deposition could be prevented; and heavy oil production/transport could be improved by creating a ‘slippage layer’ on rock pore walls and inner surfaces of transport pipes.

Table of Contents

List of Tables

List of Figures

Chapter 1: Introduction

The work presented in this thesis is divided into seven chapters. In the first, introductory chapter, a brief overview of some energy industry applications where heating is necessary are discussed, as well as the potential advantages of using magnetic induction heating as an alternative to these methods. Then, the objectives of this research work are presented. In the second chapter, the background and inspiration for the magnetic nanoparticle heating concept are presented; the relevant magnetic and nanoparticle heating principles are discussed; and the basic transport phenomena concepts necessary for understanding the modeling portion of the work are described. The third chapter discusses the experimental materials, methods, apparatus, and results for the magnetic nanoparticle dispersion experiments performed. The fourth chapter describes the process of embedding nanoparticles into a composite dubbed "nanopaint," and the experimental results yielded from using a nanopainted tube to heat a static and flowing fluid. The dispersion and nanopaint experimental models generated using COMSOL are presented in the fifth chapter; they help to improve the understanding of some of the physical phenomena from the experiments as well as highlight important design variables for scale up. The sixth chapter presents the concept of using a pipeline as a waveguide for remote delivery of magnetic energy to target zones in a pipeline and the associated modeling work. The final chapter outlines the general conclusions from this thesis and future work necessary to advance the large scale deployment of the magnetic nanoparticle heating concept.

1.1 POTENTIAL APPLICATIONS FOR MAGNETIC NANOPARTICLE HEATING IN THE ENERGY INDUSTRY

In the upstream oil and gas industry today, being able to locally heat a medium in a controlled and efficient manner is an extremely valuable tool. Heat can prevent the formation of methane hydrates in deep sea pipelines, and other high pressure, low temperature flow lines. It can also be used to reduce the viscosity of heavy oil or melt paraffin buildup in well pumping equipment. In all of these situations it can be difficult to convey heat efficiently and precisely to the target zone. In many cases heating is inefficient because of losses to neighboring medium (sand, seawater, steel, etc).

The current primary form of heating for deep sea pipelines to prevent methane hydrate formation is direct electrical heating (DEH). Heating by this method introduces various challenges due to the large amounts of power required, as well as electromagnetic and mechanical barriers. One of the key problems with DEH is the requirement of the cable to be bare in order to heat the pipeline from the outside. This renders the cable vulnerable to mechanical damage, such as stretching or crushing. Large power consumption can become a problem since loads increase with distance of the cable from the pipeline; flow systems can reach power requirements of up to 1500 A and 52 kV (Roth, 2011; Urdahl et al., 2003). Electrical heating is also employed to heat the high-viscosity oil in heavy oil reservoirs for its enhanced recovery (Hascakir et al., 2008). Inductive heating of the heavy oil reservoirs has also been investigated and tested (Sierra et al., 2001). The latter technique heats reservoirs by oscillating water molecules in the reservoir which locally heats the fluids. Disadvantages of these electromagnetic (EM) methods include an uneven distribution of heating due to sparse water saturation, and poor propagation of heat beyond the wellbore (Das, 2008).

Magnetic induction heating utilizing superparamagnetic nanoparticles provides a potential solution to these problems arising for the pipeline heating and reservoir heating applications. For example, the magnetic energy for heating can be delivered wirelessly and remotely. The nanoparticle heating can also be carried out in the absence of water. The nanoparticles can be selectively placed in regions where heat is necessary, and stimulated to generate the desired amount of heat in a controlled manner. The general principles underlying how the nanoparticles convert magnetic energy to heat are discussed in the second chapter of this thesis. The advantage of this technique is that the heat-generating nanoparticles are in direct contact with the targeted fluid, so fast and efficient conductive heating can take place. Furthermore, the EM energy necessary to stimulate the nanoparticles can be directed to the desired locations via a waveguide in some applications. Current electromagnetic energy delivery technology restricts the immediate applicability of this technology to pipeline/riser heating and near-wellbore heating.

1.2 RESEARCH OBJECTIVES

Previous work in biomedical magnetic nanoparticle hyperthermia research inspired the work in this thesis. The work in the biomedical sector provided a foundation for understanding and evaluating the potential for application of the nanoparticle heating concept to oil and gas industry applications. The objectives of the early portions of this thesis work were to learn the properties of magnetic nanoparticles best suited for converting magnetic energy to heat and the electromagnetic requirements to maximize the production of heat. Next, efforts focused on (1) finding a commercially available magnetic nanoparticle that could be used for small scale experiments or mass produced

for field scale studies and (2) characterizing that type of particle's response to various frequencies and magnetic field strengths while dispersed in a fluid. The focus of the research work then shifted to exploiting the high frequency heating mechanism of the nanoparticles so that they could be embedded in a solid composite and painted on the inner walls of tubes ("nanopaint" experiments). The objective was to determine if reasonable amounts of heat could be generated in this manner, and to characterize the heat transfer properties of the experimental system for a static and flowing fluid. The research scope then expanded to model the dispersion and nanopaint experiments so that sensitive variables could be identified, and the physical phenomena taking place in the respective experimental systems could be better understood. COMSOL finite elemental analysis software was used to conduct the modeling work to interpret the experimental results. The final objective of this thesis research was to determine the feasibility of using a steel pipeline as a waveguide to deliver magnetic energy long distances to target heating locations. COMSOL was once again used to gain a better understanding of the optimum conditions for which steel pipelines could be used as waveguides.

Chapter 2: Theoretical Background

2.1 HYPERTHERMIA OVERVIEW

Hyperthermia, or thermotherapy, is a process by which cancerous cells are destroyed by elevating their temperature above 43 – 45 °C, the minimum protein denaturation temperature (Roti et al., 1998). Hyperthermia involves injecting magnetic particles into the affected organ or tissue and exposing these particles to electromagnetic waves which stimulate heat from the particles. This method of treatment was first considered by Gilchrest et al. in the 1940's after a medical warning stated that metallic objects within the body were heated upon exposure to a magnetic induction field. Gilchrest injected micron sized particles of iron oxide (Fe2O3 in this case) into lymph tissue to destroy metastasized tissue. Gilchrest's team was able to determine that the heat generation of the particles was dependent on the magnetic field frequency, strength, and the size of the injected particles. The groundbreaking work of Gilchrest's team has led to a full scale research effort across the world to determine the potential of hyperthermia as a viable means of cancer treatment.

The advancement of nanotechnology over the past 20 years has greatly contributed to the improvement of hyperthermia techniques and its effectiveness. The key

advantage of hyperthermia is the ability to locally heat cancerous tissue in a highly controlled manner. Nanoparticles (NPs) of a desired material can be synthesized with a very narrow size distribution, which contributes to controlled heating as well as transport within the body (Batlle and Labarta, 2002; Hergt et al., 2006). Engineered "smart" nanoparticle coatings have enabled NPs to target specific tumor cells and bind to their receptors, thus making heating of the proper tissues even more precise.

2.2 RELEVANT MAGNETIC PRINCIPLES

Magnetic nanoparticle heating (MNH) is possible due to a few basic magnetic principles. First, the magnetic energy must be delivered to the nanoparticles. Experimentally, a solenoid was used to deliver the magnetic energy to the nanoparticles. A solenoid is a series of circular wire turns through which current flows. The circular flow of current generates a magnetic field that is nearly uniform at the center of the wire turns, and rapidly reduces to zero outside of the wire turns. The electromagnetic (EM) wave produced by a solenoid is a transverse electric wave, which means that there is no electric field in the direction of wave propagation, and the magnetic field propagates in the direction of the EM wave (Kong, 1986). The induced magnetic field within the solenoid can be calculated using Ampere's law shown in Eq. (1).

$$B = \frac{\mu N I}{L} \tag{1}$$

where B is the induced magnetic field within the solenoid [T], μ is the relative magnetic permeability of the material [dimensionless], N is the number of solenoid wire turns, I is the current flowing through the wire turns [A], and L is the axial length of the solenoid

[m]. Equivalently, the induced magnetic field can be calculated if the magnetic field strength, H, is known.

$$B = \mu_0(H + M) \tag{2}$$

$$H = \mu B \tag{3}$$

where μ_0 is the magnetic permeability of free space [$4\pi \cdot 10^{-7}$ H m^{-1}], H is the magnetic field strength (amplitude) [A m^{-1}], and M is the magnetization of the material [A m^{-1}]. The experimental magnetic field strength was found using Eqs. (1) – (3) as will be demonstrated in the experimental methods section.

Correlating the material response to the application of a magnetic field with its magnetic properties is essential for magnetic induction heating processes. There exists paramagnets, whose magnetic moment, m, aligns in the direction of the applied magnetic field, but magnetism is lost once the applied field is removed. Paramagnets have a susceptibility less than one, which generally falls in the range of 10^{-6} – 10^{-1} (Morissh, 2001). There also exists diamagnets whose magnetic moments align opposite to a magnetic field when applied, then disappear once it is removed. Ferromagnets contain multiple domains in which the spins of free electrons within the material align, thus creating a permanent magnetic moment within each domain (Callister, 2007). The spin alignment direction of each domain within the material is random, so the net magnetic moment of ferromagnets is typically small; however, in the presence of a magnetic field, the magnetic moment of all of the domains align which generates a larger magnetization than for other types of magnetic materials, as well as increases the magnetic field amplitude. The amount that a magnetic material increases the magnetic field amplitude is

the relative permeability of the material, which is large for materials with large magnetizations (Callister, 2007).

The type of magnetic material most important for this work is a form of paramagnetism known as superparamagnetism. Superparamagnetism is found in ferromagnetic materials in the size range 3 – 50 nm in diameter. Superparamagnetic nanoparticles have a single magnetic domain due to the particles being so small that they cannot support a wall; this contributes to a much larger magnetic moment in the presence of a magnetic field than in typical paramagnetic materials. Thus, they also have much higher magnetic susceptibilities than typical paramagnets (Gubin, 2009). Superparamagnets have zero coercivity and remanence. Coercivity is the magnetization required to reduce a magnetized material back to zero after reaching saturation. In agreement with paramagnetic theory, zero coercivity means that once the applied magnetic field is removed, the internal magnetic moment of the material will once more randomize with no reverse magnetization necessary. Furthermore, zero remanence means that after removal of the external magnetic field, randomization of the internal magnetic moment of the superparamagnet reduces the magnetization of the material to zero, which is also a property of standard paramagnets. Because of these two principles, superparamagnetic materials do not undergo magnetic hysteresis cycles, which will be discussed more in the next section. The superparamagnetic nanoparticle state gives rise to relaxation modes that generate large amounts of heat given the proper conditions.

2.3 SUPERPARAMAGNETIC NANOPARTICLE RELAXATION MODES

There are three primary mechanisms by which magnetic nanoparticles dissipate heat: Neel relaxation, Brown relaxation, and hysteresis. Magnetic nanoparticle heating (MNH) is dependent on the alternating current (AC) frequency of the applied electromagnetic energy as well as the size of the nanoparticles. The frequency determines if the particles undergo Neel or Brown relaxation mechanisms, and the particle size determines if particles dissipate heat via a relaxation mechanism or hysteresis. Determination of the dominant relaxation mechanism and the magnetic principles that contribute to each relaxation mechanism will be discussed next.

Magnetic nanoparticles rarely have magnetic moments which are energetically equivalent, which gives them magnetic anisotropy. There are several types of magnetic anisotropy, but surface anisotropy and volume anisotropy are most important for nanoparticle relaxation. Surface anisotropy is proportional to the particle surface area and arises due to fluctuations in the crystalline magnetic field. These field fluctuations result from asymmetry on the particle surface and act on ions on the surface of the particle (Laurent et al., 2011). Volume anisotropy results from a non-isotropic internal crystal structure which gives rise to energetically unequivalent magnetic moments within the nanoparticle (NP). The contributions of surface and volume anisotropy sum to the uniaxial anisotropy as shown in Eq. (4).

$$E(\theta) = (K_V V + K_S SA)\sin^2\theta \tag{4}$$

where K_v is the volume anisotropy constant [kJ m^{-3}], V is the NP volume [m^3], K_s is the surface anisotropy constant [kJ m^2], SA is the NP surface area [m^2], and θ is the angle

between the anisotropic axis and the particle's magnetic moment vector (Laurent et al., 2011). Discussion of the NP anisotropic energy barrier usually ignores the surface contribution to simplify the analysis. In the absence of an external magnetic field, the magnetic moment aligns itself with the easy magnetocrystalline anisotropy axis, or "easy axis," in order to achieve a minimum energy. Two neighboring energy minima are separated by K_vV, so in the presence of an external AC magnetic field, the particle must overcome an energy barrier equivalent to K_vV to attain a minimum energy state (alignment of M with the easy axis; Laurent et al., 2011).

For a given temperature, there is a finite probability that thermal fluctuations in the particle will induce the magnetic moment to surpass the anisotropic energy barrier, and then relax back to its original state. The time required for the magnetic moment to excite and relax is known as the Neel relaxation time and is described by Eq. (5).

$$\tau_N = \tau_0 e^{\left(\frac{K_vV}{k_bT}\right)} \tag{5}$$

where τ_N is the Neel relaxation time [s], τ_0 is the pre-exponential factor [s], k_b is Boltzmann's constant [1.3806503 × 10^{-23} m^2 kg s^{-2} K^{-1}], and T is the measurement temperature [K]. The pre-exponential factor is a measure of a particle's anisotropic energy and is a function of variables such as the anisotropic constants, temperature, saturation magnetization, and height of energy barrier among others. The pre-exponential factor is generally considered a constant in the range of 10^{-9} – 10^{-13} s, and has been found to be ~ 10^{-9} s for iron oxide nanoparticles (Neel, 1949; Moskowitz et al., 1997). The Neel relaxation time, or characteristic time, represents the time required for a system of non-interacting particles to reach thermal equilibrium, which will occur faster at higher

temperatures (smaller τ_N). The time required to magnetize a nanoparticle to saturation is the characteristic measurement time, τ_m. If $\tau_m >> \tau_N$, then the magnetic moment will rotate several times (excite and relax) within the Neel relaxation time and the particle magnetization during the measurement period will average to zero. Contrarily, if $\tau_N >> \tau_m$ then the particle does not have time to excite and relax, thus its magnetic moment appears blocked. The temperature at which this occurs is known as the blocking temperature. The blocking temperature can be found by setting $\tau_N = \tau_m$, and solving for T; this is the minimum temperature at which superparamagnetic NP heating experiments should be performed.

Nanoparticles dispersed in a fluid can also exhibit Brown relaxation. The characteristic Brown relaxation time is calculated via Eq. (6).

$$\tau_B = \frac{4\pi\eta r_h^3}{k_b T} \tag{6}$$

where τ_B is the Brown relaxation time [s], η is the viscosity of the fluid [Pa-s], and r_h is the hydrodynamic radius of the particles [m]. Brown relaxation occurs when the magnetic moment of the particle is locked to the easy axis, and alternation of the magnetic field results in the particle physically rotating. This particle rotation causes friction between the particle and the fluid, which in turn generates heat. As the viscosity of the fluid increases, particle rotation becomes hindered, thus producing less heat until the point at which the viscous force of the fluid overcomes the rotational force of the particle and particle motion ceases.

In some frequency ranges, Neel and Brown relaxation mechanisms compete, but the faster relaxation mechanism dominates. **Fig. 1** demonstrates the particle size dependence of relaxation time constants.

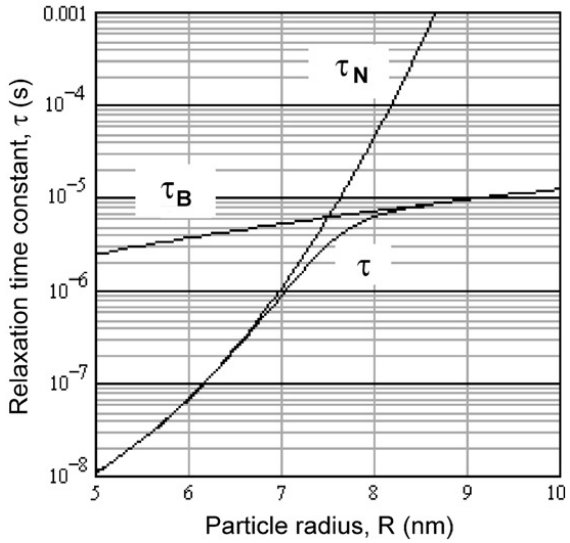

Figure 1—Nanoparticle size dependence of relaxation time constants (Rosensweig, 2002).

The transition from Brown relaxation being the dominant time constant to Neel relaxation is shown at approximately 7.5 nm. For experiments or applications that are tailored to utilize Neel relaxation, NP diameter is an important design parameter that must be controlled accordingly during the synthesis process. In Fig. 1, τ represents the effective time constant, which is calculated using Eq. (7).

$$\tau = \frac{1}{\tau_N} + \frac{1}{\tau_B} \tag{7}$$

where τ is the effective relaxation time constant [s]. The form of Eq. (7) is that of a parallel process because the two relaxation mechanisms occur in parallel (Rosensweig, 2002). The value of the effective time constant represents the value of the dominant relaxation time constant (the smaller of the two τ's represented).

Researchers have also demonstrated that the dominant relaxation mechanism is also dependent on the AC frequency of the magnetic field. Experimentally, this was determined by exploiting that Brown relaxation requires a particle to have mobility, while Neel relaxation does not. By embedding superparamagnetic iron oxide nanoparticles (SPIONs) into a highly viscous polymer gel in one experiment and in a non-viscous fluid in another, researchers were able to determine the dominant relaxation mechanism as a function of frequency. Hergt (2004) used the specific loss power (SLP) of the particles, which is an implicit measurement of the temperature rise in the fluid/gel, to gauge the response of the particles with frequency. The actual quantity measured in the experiments was the susceptibility spectrum. The specific loss power represents the amount of energy dissipated by the particles per gram of iron oxide nanoparticles during the time length of the experiment. **Fig. 2** demonstrates the results of the experiment performed by Hergt et al. (2004).

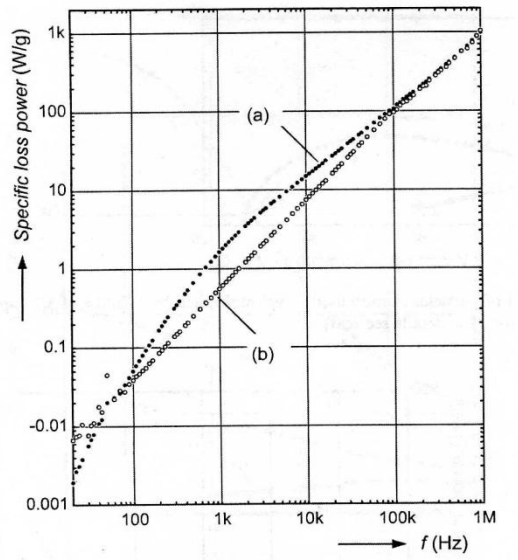

Figure 2—Frequency dependence of specific loss power deduced from the measured imaginary part of susceptibility for original ferrofluid (a) and suspension gel (b) (Hergt et al., 2004).

Figure 2 indicates that the ferrofluid has a larger SLP in the frequency range of 10 Hz – 100 kHz, which demonstrates that Brown relaxation was the dominant relaxation mechanism. At a frequency of 100 kHz the ferrofluid and gel curves merge together, which is the point at which Neel relaxation begins to dominate. For experiments and applications where the NPs are embedded in a solid media, it is essential to maintain the frequency above 100 kHz for optimal results. Neel relaxation continues to have a dominant heating affect until it passes through a specific loss maximum around 1 GHz due to ferromagnetic resonance as demonstrated by Fannin et al. (1999).

Another loss mechanism that is not characterized by NP relaxation is hysteresis. As mentioned previously, hysteresis does not occur in superparamagnetic nanoparticles, but some early experiments were done on larger particles where it is applicable. Furthermore, hysteresis is an important consideration if particles with a large size distribution are used for experiments or applications. Hysteresis losses occur due to the

presence of domain walls in multi-domain magnetic particles. As the particles are magnetized and demagnetized, the induced magnetic field lags behind the applied magnetic field, which results in a hysteresis loop. This is a result of the ferromagnetic nature of the larger particles: a coercive force is required to demagnetize the particles and they also have a remnant magnetization. As the particles are magnetized and demagnetized, their magnetic domains expand and contract due to movement of the domain walls. As the domain walls move past one another, they produce friction, which is dissipated as heat (Kronmuller and Fahnle, 2003). The amount of energy dissipated per magnetization/demagnetization cycle can be calculated by integrating the area of the hysteresis loop (Bertotti, 1998).

2.4 CALCULATION OF THE POWER LOSS FOR SUPERPARAMAGNETIC NANOPARTICLES

Rosensweig (2002) provides a power equation which predicts the energy dissipated by superparamagnetic NPs when subjected to oscillating magnetic field for the Neel relaxation mechanism. Rosensweig assumes an adiabatic system, and from the first law of thermodynamics derives the change in internal energy of the system based on the magnetic work done on the system.

$$\Delta U = -\mu_o \oint MdH = 2\mu_0 H_0^2 \chi'' \int_0^{2\pi/\omega} sin^2 \omega t dt \tag{8}$$

where H_0 is the maximum magnetic field strength; and χ'' is the out-of-phase component of the magnetic susceptibility (also known as the "loss" component), which depends significantly on τ_N. Integration and multiplication by the cyclic frequency (f) yields the

power dissipated, P, in terms of the magnetic properties of the system and the loss component (as given by Eq. (8) above).

$$P = f\,\Delta U \tag{9}$$

Rosensweig further manipulates the power dissipation in terms of the magnetic NP properties. Equation (10), below, is based strictly on properties of the NPs themselves and is independent of the environment in which the NPs are placed. This may introduce some error into predictions of the energy gained by fluids in contact with the particles, unless the experiments are performed in a completely adiabatic system and allowed to reach thermal equilibrium. A slightly modified form of Eq. (9) is used due to Rovers et al. (2009) to estimate theoretically the expected energy gained by fluids in contact with the nanoparticles:

$$P = \frac{2(\pi m H f \tau_N)^2}{\tau_N k_B T V (1 + (2\pi f)^2 \tau_N{}^2)} \tag{10}$$

$$m = \frac{\pi \mu_0 M d_c^3}{6} \tag{11}$$

where m is the magnetic moment of the particles [A m^2], and d_c is the diameter of the NP core [m]. The energy dissipated by the particles has a strong dependence on the magnetite core diameter, so small variations in particle diameter can cause large differences in the amount of heat generated. This will be discussed in detail in the following section which describes relevant particle properties. For a unique NP size, the energy dissipated by the

particles is quadratically dependent on frequency when $(2\pi f)^2\tau^2 << 1$, and independent of frequency when $(2\pi f)^2\tau^2 >> 1$. The energy dissipated is quadratically dependent on the magnetic field strength (Hergt, 2004). Deviations from this experimental result have also been observed by other researchers.

2.5 NANOPARTICLE PROPERTIES IMPORTANT FOR HEATING

Several nanoparticle properties directly affect the effectiveness of the heating process. The influence of these properties on the heat generated is interpreted via the specific loss power/ specific absorption rate, or the measured susceptibility, depending on which method the researcher preferred. The specific loss power is the amount of energy emitted by the nanoparticles per unit time per unit mass of particles, and the specific absorption rate is the amount of energy absorbed by the target heated fluid per unit time per mass of nanoparticles. The two primary NP properties that will be discussed are the chemical composition and NP diameter. The NP shape, which is determined by the synthesis process, has been reported to also affect the type of loss process and heating rate (Hergt et al., 1998). The NP shape is most relevant for heating cases where Brown relaxation dominates, so the shape influences the friction between the NP and the fluid.

Nanoparticles composed of various chemical species have been synthesized and tested for their effectiveness in generating heat for hyperthermia applications. Experiments performed by Rosensweig indicated that the heating rate of the NPs is heavily dependent on the magnetic anisotropy constant and magnetization of the material. Nanoparticles with a higher saturation magnetization and a lower anisotropy constant exhibit higher heating rates (all other properties being equivalent; Rosensweig, 2002).

Due to its high magnetization relative to other common magnetic NP materials, magnetite (Fe_3O_4) NPs were selected for the experimental portion of the work described in this thesis. In addition to its excellent magnetic properties, magnetite is commonly used for various magnetic NP applications, so commercial suppliers of magnetite NPs were easily found.

Nanoparticle diameter is an important design variable to investigate because it has a significant influence on the heating rate. Hergt et al. (2006) observed that mean particle diameter coupled with a narrow size distribution are the most important parameters for maximizing specific loss power. Quantification of the SLP of the NPs for fluid experiments is performed by measuring the amount of heat absorbed by the fluid for a given NP concentration; this quantification is known as the specific absorption rate (SAR) and is considered equivalent to the SLP. From Fig. 1, NP diameter greatly influences which relaxation mode dominates. Equation (10) was used to evaluate the relationship between SLP (SAR) and NP diameter at frequencies of 430, 900, and 1800 kHz and a magnetic field strength of 5 kA/m; this is shown in **Fig. 3**.

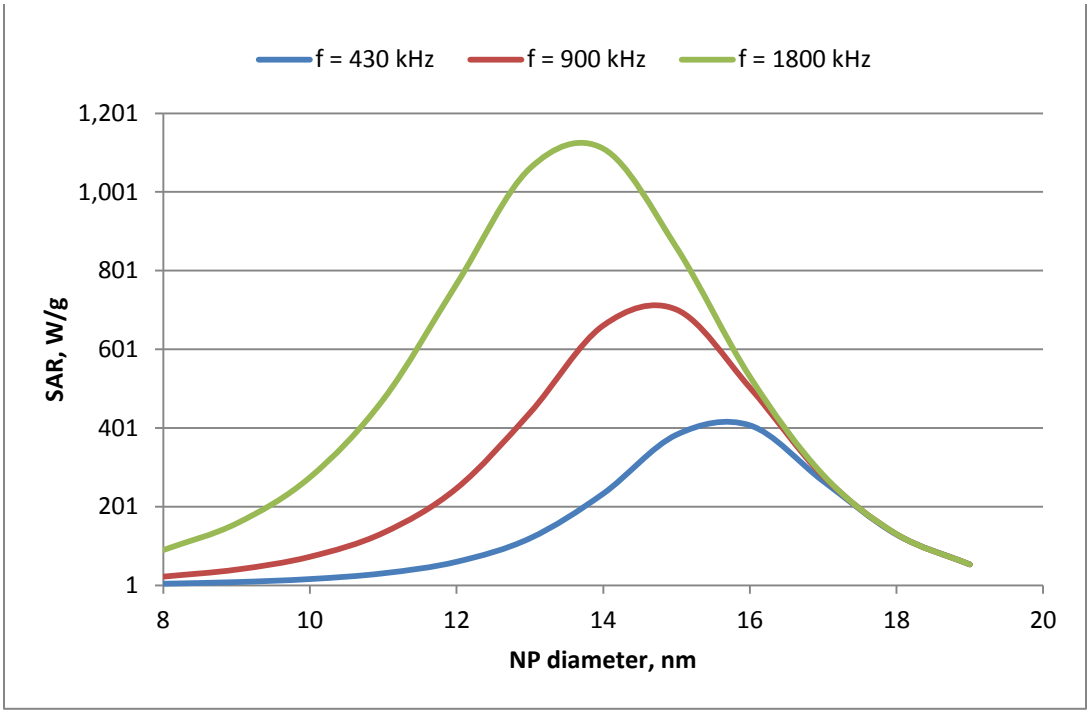

Figure 3—Influence of NP diameter on SAR at a frequency of 430, 900, and 1800 kHz and a magnetic field strength of 5 kA/m.

Inspection of Fig. 3 indicates a maximum SAR value for a given frequency exists at a specific NP diameter. While not obvious from Eq. (10), a maximum in SAR at a specific NP diameter occurs because at this diameter, τ_N (which is exponentially dependent on NP volume) begins to dominate in the denominator of Eq. (10). Monodisperse NP samples with a mean NP size corresponding to the maximum SAR frequency produces the best heating response. However, since it is very difficult to control the distribution of NP sizes within a given sample, the NP size distribution shape, mean, and standard deviation were investigated.

The following NP size distribution analysis was performed at a magnetic field strength of 5000 A/m and a frequency of 430 kHz. The SAR values were calculated using Eq. (10) as in Fig. 3, but for distributions, a cumulative SAR was calculated based on the

contribution of each NP size in the distribution. First, a lognormal distribution was used to demonstrate how a long tail can influence the resulting heating rate. **Figure 4** shows the lognormal distribution for NPs with a mean of 12.1 nm and a standard deviation of 3.0 nm; this is the size distribution reported by Rovers et al. (2009).

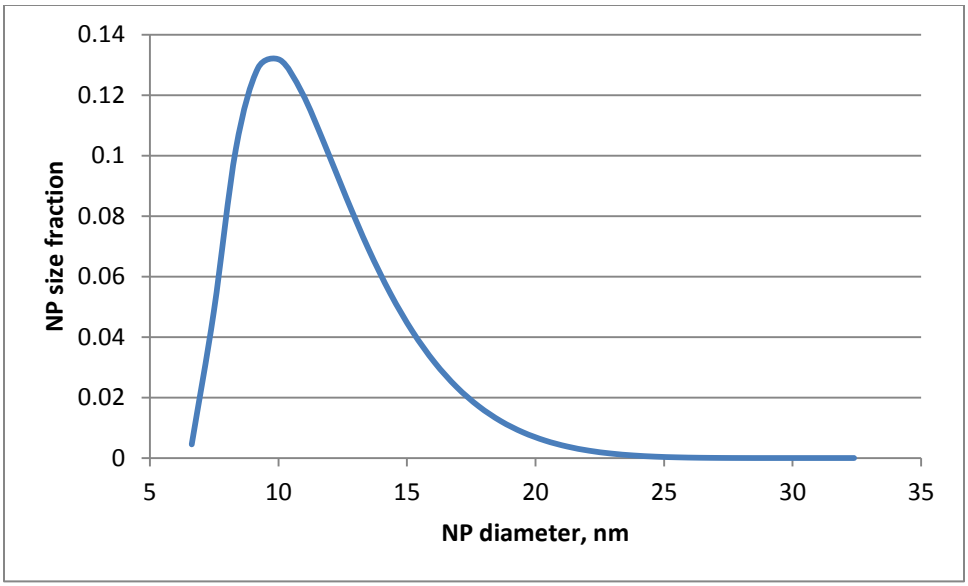

Figure 4—Lognormal NP size distribution with a mean of 12.1 nm and a standard deviation of 3.0 nm.

Since this analysis was performed with respect to relaxation mechanisms, the contribution of NPs greater than 20 nm (the limit of superparamagnetic behavior) was not considered. A SAR calculated purely based on a monodisperse NP size of 12.1 nm yields 65.4 W/g. A SAR calculated using the distribution shown in Fig. 4 yields 89.3 W/g, which represents a 36% increase in SAR by introducing the lognormal size distribution. Next, the same distribution shape was used, but the mean NP size was increased slightly to 13.8 nm (a 14% size increase) and the standard deviation was kept at 3.0 nm; this is shown in **Fig. 5**.

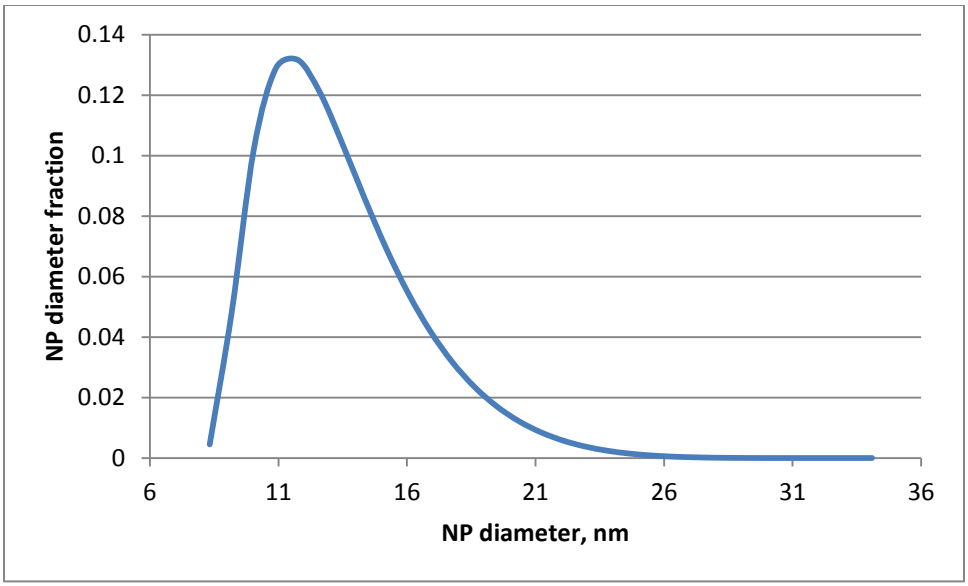

Figure 5—Lognormal NP size distribution with a mean of 13.8 nm and a standard deviation of 3.0 nm.

A SAR calculated using the distribution in Fig. 5 yields a SAR of 135.2 W/g, whereas the SAR calculated from just the mean NP size of 13.8 nm yields a SAR of 206.5 W/g (a 35% decrease). The NP size distribution resulted in a decrease in SAR in this case because the ideal NP size for a frequency of 430 kHz is 15.6 nm, so the large fraction of NPs around 12 nm reduces the cumulative SAR relative to a non-distributed mean NP size of 13.8 nm. A monodisperse particle distribution around 15.6 nm, or a mean shifted toward 15.6 would greatly improve the heating rate of NPs at a frequency of 430 kHz. Comparison of the distribution curves for a mean NP size of 12.1 and 13.8 nm indicates that increasing the mean by 14% (towards the ideal NP size of 15.6 nm) increases the SAR by 51%, which is significant for such a small change in NP diameter. Comparison of the SAR for monodisperse NP sizes at 12.1 and 13.8 nm shows a significant increase

from 65.4 to 206.5 W/g. This large sensitivity in NP diameter is due to the SAR's linear dependence on τ_N at some frequencies, and τ_N exponentially dependent on NP volume.

Now, the effect of changing the distribution shape, but keeping a mean NP diameter of 13.8 nm, and a standard deviation of 3.0 nm will be investigated. In **Fig. 6**, a negatively skewed Johnson moments distribution was used to represent the opposite of the lognormal distribution.

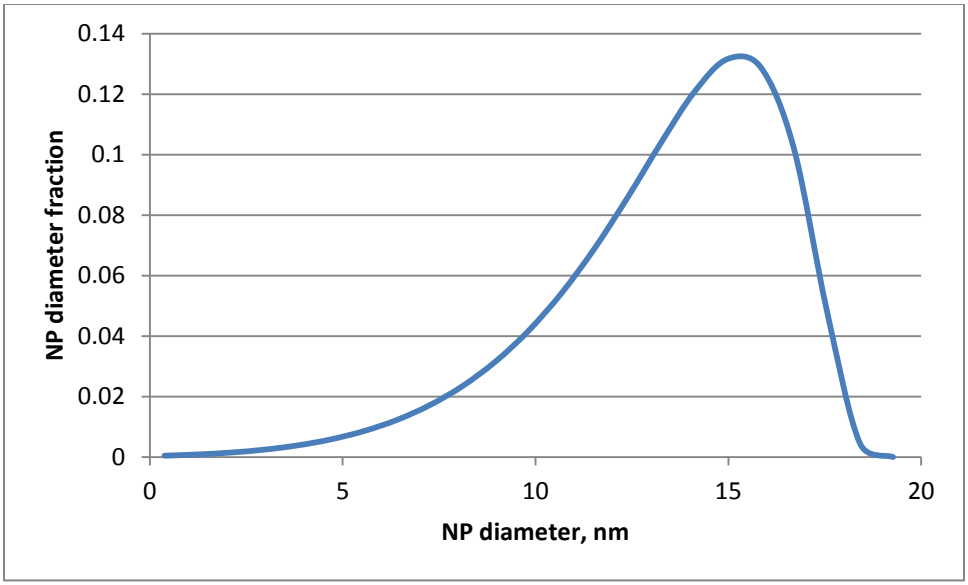

Figure 6—Negatively skewed Johnson moments NP size distribution with a mean of 13.8 nm and a standard deviation of 3.0 nm.

In Fig. 6, it is apparent that a much higher frequency of particles is localized around 15.6 nm (the ideal NP size). As expected, the contribution of the smaller NPs does skew the SAR downward slightly; the NP distribution yields a SAR of 203.8 W/g compared to the SAR for the Johnson moments size distribution of 206.5 W/g (a 1% decrease). By shifting from a positively skewed distribution to a negatively skewed distribution with

more particles localized around the ideal SAR NP size, a 51% increase in SAR results. This analysis indicates the immense importance of maintaining a controlled NP synthesis process where the largest fraction of particles fall near the ideal NP size based on the expected operating frequency.

2.6 TRANSPORT PHENOMENA IMPORTANT FOR INTERPRETATION OF HEAT AND MOMENTUM TRANSFER

The work discussed in this thesis focuses on transformation of energy from magnetic to heat, thus it is important to look at the physics that define how that heat is transferred. The transfer of heat by conduction is driven by a temperature gradient, which is described by Fourier's law in three dimensions.

$$q = -k\nabla T \tag{12}$$

where q is the heat flux [W m^{-2}], k is thermal conductivity of the medium [W m^{-1} K^{-1}], and ∇T is the temperature gradient [K m^{-1}]. The heat flux describes the flow of heat per unit area. Often, temperature changes with respect to time as well as a spatial dimension, thus a differential equation with respect to both is used to describe the system. The diffusive heat equation in Eq. (13) is a common 2nd order partial differential equation used to describe conservation of energy in systems with a heat source.

$$\rho C_p \frac{\partial T}{\partial t} = k\nabla^2 T + Q \tag{13}$$

where T is temperature, t is time, and Q is the heat source. The diffusive heat equation will be used to solve transient heat conduction for a system of nanoparticles in a fluid medium. It will also be used to describe the transient flow of heat from an annular heat source in contact with a cylinder of fluid.

In systems where a fluid is in motion, momentum transfer is necessary to describe the flow of energy. For fluids in the turbulent flow regime, the Navier-Stokes equation is used to consider momentum transfer within the system. The theoretical background for the turbulent flow solutions for the Navier-Stokes equation (15) is given in Bird, Stewart, and Lightfoot (2007). The specific turbulent stress expression employed for the COMSOL simulation is described later in Chapter V. The Navier-Stokes equation describes the change in velocity in both the time and spatial domains. A general form of the Navier-Stokes equation is shown in Eq. (14).

$$\rho \frac{Dv}{Dt} = -\nabla p + \nabla \cdot \sigma + F \tag{14}$$

where Dv/Dt is the material derivative of velocity, σ is the deviatoric stress tensor, and F is the body force per unit volume acting on the fluid. Equation (15) is the r-component of Eq. (14) in cylindrical coordinates with Newtonian viscosity, which will be used for modeling purposes later in this thesis.

$$\rho\left(\frac{\partial v_r}{\partial t} + v_r \frac{\partial v_r}{\partial r} + v_z \frac{\partial v_r}{\partial z}\right) = -\frac{\partial p}{\partial r} + \eta\left[\frac{1}{r}\frac{\partial}{\partial r}\left(r\frac{\partial v_r}{\partial r}\right) + \frac{\partial^2 v_r}{\partial z^2} - \frac{v_r}{r^2}\right] \tag{15}$$

where v_z is the velocity in the z-coordinate, v_r is the velocity in the r-coordinate, η is the fluid viscosity [Pa s], ρ is the density of the fluid [kg m^{-3}], and g is the gravitational

constant [m s^{-2}]. The radial velocity terms were kept in this equation because they were used to determine if radial flow and mixing were significant around constrictions and expansions using computational software.

Newton's law of viscosity relates the flow velocity with stress, e.g., τ_{yx}, due to a fluid moving in x-direction on a unit area perpendicular to the y-direction, given in the form shown in Eq. (16; Bird, Steward, and Lightfoot, 2007).

$$\tau_{yx} = -\eta \frac{dv_x}{dy} \tag{16}$$

where τ_{yx} is the shear stress in the x direction [Pa], and η is the Newtonian viscosity [Pa s] which will be a function of T.

Also important for understanding nanoparticle heating in steady state flowing fluid systems is the energy balance based on the law of conservation of energy. An energy balance is employed to understand the flow heat from a source (the NPs) to a flowing fluid. Thus, it accounts for the flow of energy in the form of heat and momentum. For the work presented, the energy balance in cylindrical coordinates is of interest. The derivation of this energy balance can be found in Bird, Stewart, and Lightfoot (2007), and the final, unsimplified form of the equation is shown in Eq. (17).

$$\rho \hat{C}_p v_z \frac{\partial T}{\partial z} = k\left[\frac{1}{r}\frac{\partial}{\partial r}\left(r\frac{\partial T}{\partial r}\right) + \frac{\partial^2 T}{\partial z^2}\right] + \eta\left(\frac{\partial v_z}{\partial r}\right)^2 + v_z\left[-\frac{\partial p}{\partial z} + \eta\frac{1}{r}\frac{\partial}{\partial r}\left(r\frac{\partial v_z}{\partial r}\right)\right] \tag{17}$$

where $\widehat{C_p}$ [J kg^{-1} K^{-1}] is the specific heat capacity at constant pressure. Further simplification and discussion of this equation will occur in the specific modeling sections where it is used to describe an experimental or field scale system.

Chapter 3: Dispersed Nanoparticle Experiments

In the following chapter, we will discuss in detail the dispersed nanoparticle heating experiments conducted for this thesis work. The dispersion heating experiments were performed in two parts: (1) early feasibility experiments with a low power, rudimentary apparatus; and (2) extensive characterization experiments with a high power induction heating apparatus. The materials and material properties will be discussed, as well as the sample preparation and apparatus used for each group of experiments. A discussion of the relevant results and comparison to expected trends based on the discussed theory will also ensue.

3.1 Experimental Materials and Methods

The experimental work has focused on establishing the effectiveness of the nanoparticle heating behavior in varying magnetic field strengths and at different frequencies. It is necessary to establish particle behavior in "ideal" experimental conditions so that future experiments involving extensions from these conditions can still be analyzed and compared to the results from these "ideal cases." An "ideal" experiment with the current apparatus involves placing a sample at the location of maximum magnetic field strength where it is assumed that the field is uniform.

The magnetic NPs used for all of the experiments discussed were purchased from a commercial supplier (Ferrotec, Germany). Particles with both hydrophilic and hydrophobic coatings were purchased to determine if particle coating and solvent properties affect particle heating behavior. The particles have an iron oxide core, Fe_3O_4

or magnetite, and the core diameter for both types of particles was said to be 10 nm. Further study of the nanoparticle core sizes for both hydrophilic and hydrophobic samples was performed via transmission electron microscopy (TEM). To perform TEM imaging on the samples, the NPs, hydrophilic or hydrophobic, were dispersed in a suitable solvent and the dispersion was applied to a substrate plate. The plate was then baked to induce evaporation of the dispersing fluid. From there the NP samples could be imaged without solvent interference in the images.

First, the hydrophilic NPs, EMG700, were characterized via TEM imaging. For the imaging process, the NPs were dispersed in water. The most representative image of the hydrophilic NPs is shown in **Fig. 7**.

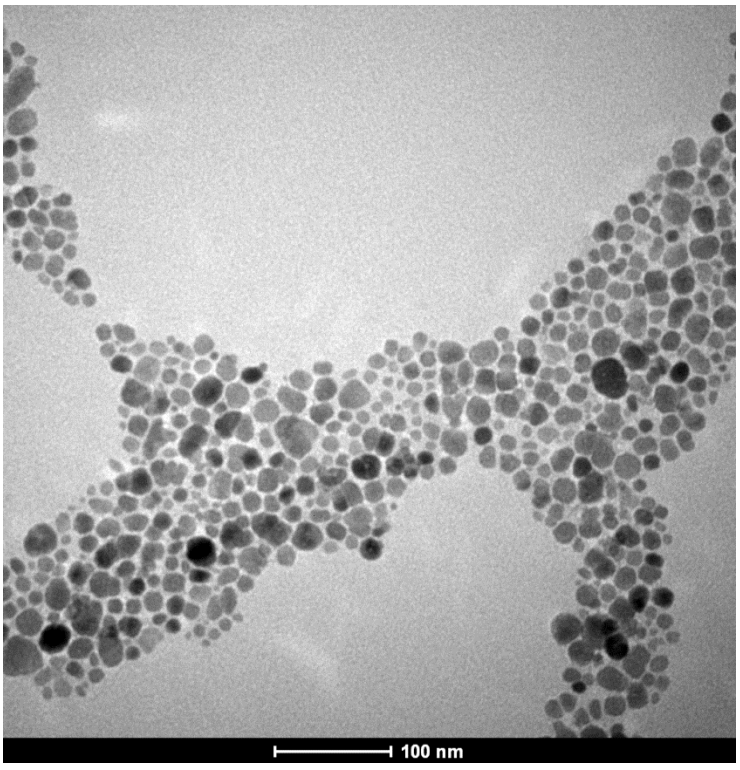

Figure 7–TEM image of hydrophilic NPs dispersed in water.

The image shows mild aggregation in some areas, but overall, good separation of the NPs due to the hydrophilic surface coating. Analysis of the NP size and distribution was performed using the Java based image processing software, ImageJ. Nanoparticle size analysis was performed by adjusting the color threshold of the image to include the most representative NPs, while excluding the particle aggregates. Via qualitative inspection, NPs with a circularity of 0.75 – 1.00 were considered for the size analysis. Also, the range of NP diameters considered for the analysis was 2 nm < D_p < 30 nm. This range was set based on the minimum and maximum particles measured using the image scale and image zooming where necessary. Statistical analysis of the NP diameter distribution was also performed and is characterized in **Table 1**.

Statistical quantity	**Value, nm**
Mean	14.28
St. Dev.	4.87
Min.	5.06
Max	24.70
Mode	15

Table 1— Summary of statistical characteristics for hydrophilic NPs from the TEM image in Fig. 9.

The statistical analysis also included generating a NP size distribution for use in SAR calculations (**Fig. 8**).

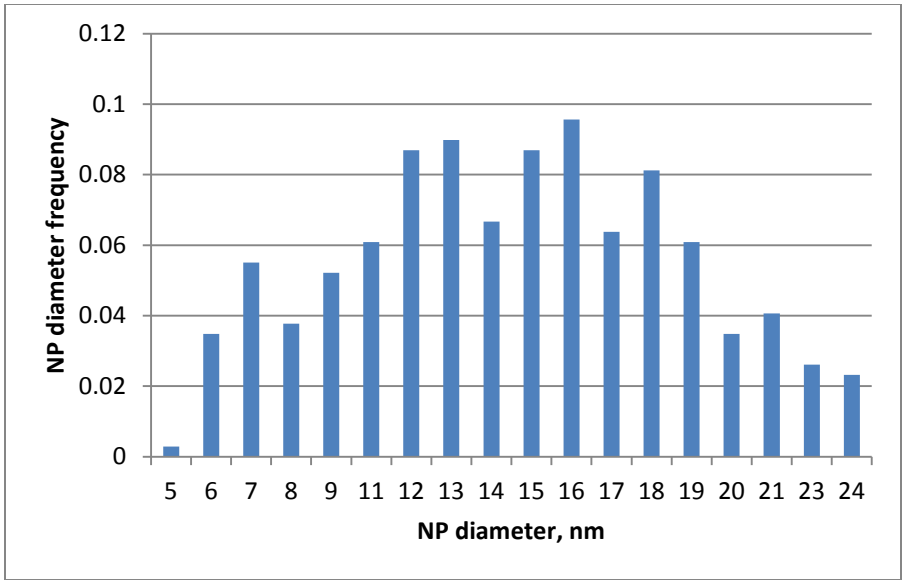

Figure 8—Hydrophilic NP size distribution for TEM image shown in Fig. 7.

The large standard deviation of NP sizes with respect to the mean is exhibited by the broad width of the Gaussian-like distribution. Ideally, the NPs would be more monodispersed with a mean size centered around 15 - 16 nm for maximum heating results, as discussed in the theoretical background section.

A similar analysis was performed for the hydrophobic NPs, EMG1400, purchased from Ferrotec. TEM images were taken for hydrophobic particles distributed in tetrahydrofuran (THF; **Fig. 9**).

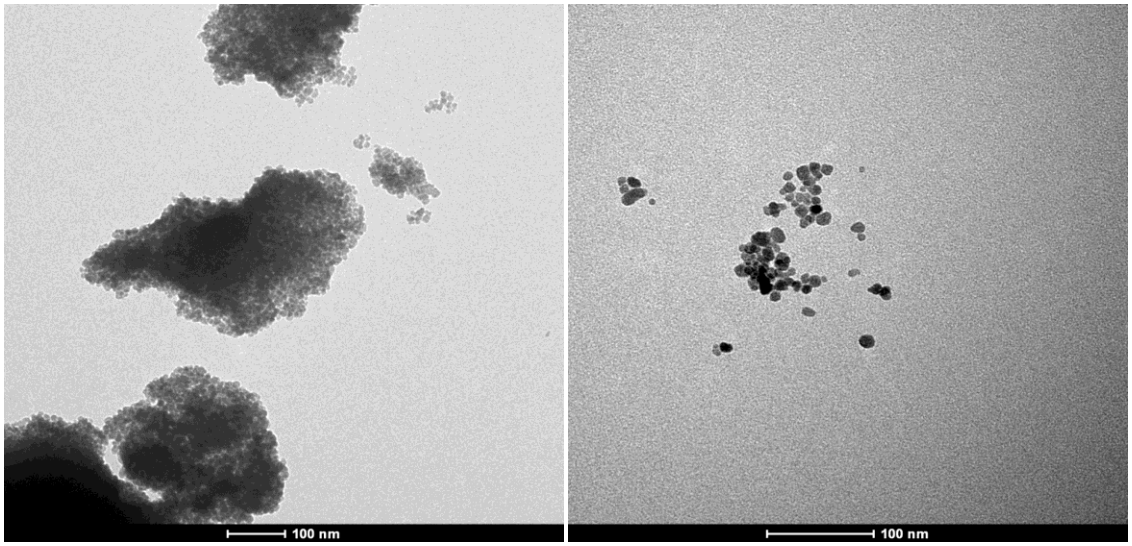

Figure 9—TEM images of hydrophobic NPs dispersed in THF. An image of large NP aggregates is shown on the left, and a zoomed in image of a less concentrated NP cluster is shown on the right.

Inspection of the images in Fig. 9 demonstrates that the hydrophobic NPs aggregate much more than the hydrophilic NPs (even in a good hydrophobic dispersant for the NPs, THF), which made image processing more difficult. The image on the left in Fig. 9 was used for particle size analysis due to the much larger population of resolvable NPs on the edges of the aggregates. **Table 2** shows the statistical characteristics of the hydrophobic NPs generated from ImageJ.

Statistical quantity	Value, nm
Mean	8.28
St. Dev.	4.34
Min.	2.25
Max	19.98
Mode	3

Table 2— Summary of statistical characteristics for hydrophobic NPs from the TEM image in Fig. 9.

The large standard deviation with respect to the mean is even more pronounced for the hydrophobic NPs than the hydrophilic NPs; the standard deviation is ~50% of the mean. One contributor to the large standard deviation is likely the high degree of aggregation and difficulty in resolving NP boundaries. **Figure 10** summarizes the NP size distribution of the sample population shown in Fig. 9.

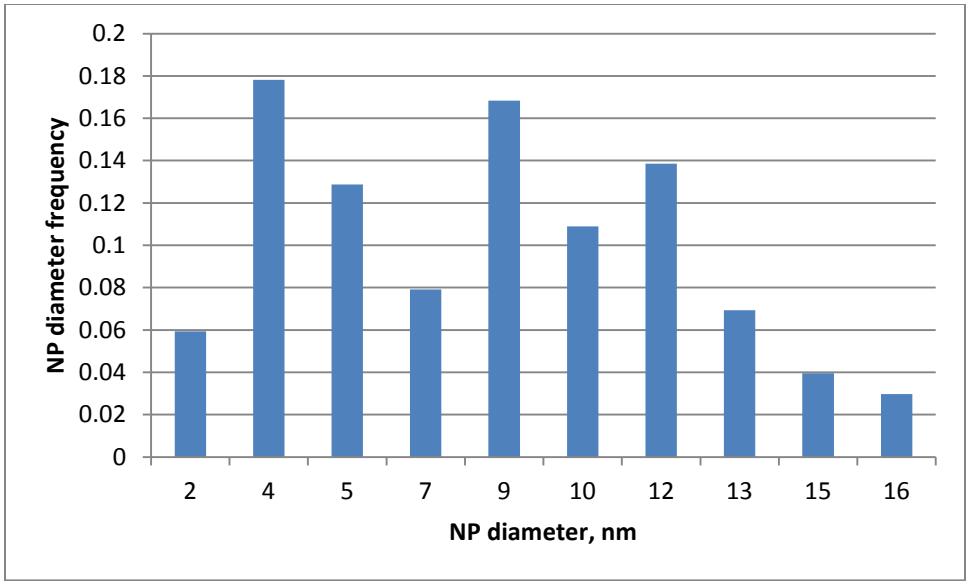

Figure 10–Hydrophobic NP size distribution for TEM image shown in Fig. 9 (left).

In contrast with the hydrophilic NP size distribution, the hydrophobic NPs have a bimodal distribution with peaks at ~4 nm and ~9 nm, with the second peak exhibiting positive skew. As with the hydrophilic NPs, a more monodisperse sample with a larger mean NP size close to 15 nm would be ideal for heating at the experimental conditions to be discussed. The image on the right shows an area of the hydrophobic NP sample with much less aggregation. The mean NP size of this image is is 9.4 ± 4.0 nm. Analysis of another TEM image (**Fig. A1** in Appendix A) indicated a mean NP size of 11.4 ± 6.6 nm, which further shows the huge variance in the hydrophobic NP sample, as well as the difficulties in size analysis created by the heavy aggregation. The latter mean NP sizes will be used for experimental model matching.

Particles with a hydrophilic coating were dispersed in water for characterization experiments, and particles with a hydrophobic coating were dispersed in hexane for characterization experiments. Using a uniformly stable dispersion in characterization

studies is important; suspension homogeneity ensures that the solvent is properly loaded with the prescribed NP weight percentage. The hydrophilic NPs disperse well in water with no sedimentation problem, and the hydrophobic particles disperse reasonably well (~ 5 minute suspension times prior to mild sedimentation, which is sufficient for the short duration heating experiments) in hexane. THF was also found to be a very good solvent for dispersing the hydrophobic NPs. While settling did not occur for the hydrophobic NPs dispersed in THF, the TEM images showed that heavy aggregation still occurred. For the "nanopaint" experiments, toluene was used as the initial particle-dispersing solvent as the hydrophobic NPs disperse well in it also, and because it is known that an aromatic like toluene would work as a good diluent for the epoxy paint resin used.

To monitor liquid temperature changes, an IR camera with digital temperature recording software was used for the low frequency feasibility studies, and a fluoroptic fiber optic temperature sensing unit called NOMAD by Neoptix, Canada LP was used for the subsequent high frequency experiments. The IR camera enabled temperature readings at the surface of the dispersion sample, and the usage of a fiber optic temperature sensor enabled readings within the fluid sample; these methods prevented magnetic/electric field interference of measurements which would occur when using standard thermocouples. When performing experimental heating trials using dispersion samples, a plastic, insulated cuvette (4 mL max volume) was used as a sample holder. When taking temperature measurements with the IR camera, the sample was placed at the center of a solenoid coil (to be explained in the following section), and the whole surface of the dispersion was imaged. When using the fiber optic temperature sensor, the probe was placed at the center (relative to height and area) of the fluid sample to measure the local temperature. The only difference between these two methods is that the IR camera

measured surface temperatures more susceptible to convective cooling, and the temperature probe measured internal sample temperatures.

3.2 Low Frequency Apparatus and Feasibility Experiments

The initial feasibility studies for this work were performed to determine if the purchased commercial NPs would be able to generate heat via the expected relaxation mechanisms The experiments were performed at low frequencies (<20 kHz) relative to the later dispersion experiments, so Brown relaxation was the expected relaxation heating mechanism.

The core of the experimental apparatus for the low frequency feasibility experiments was an 87 turn homemade solenoid. The solenoid was constructed by wrapping insulated, copper magnet wire around a 2 in. (5.08 cm) ID plastic spool. The spool measured 10 cm in length. The spool was connected to a power supply and amplifier so that currents of 0 – 15 Amperes could be flowed through the solenoid, thus generating the magnetic field. While performing experiments, the solenoid was placed in a DI water cooling bath to remove heat released from current flow through the wire. The interior of the solenoid was sealed from the bottom to prevent water from contacting and interfering with the heating results of the dispersion samples. An oscilloscope was connected in series with the amplifier so that the frequency of the alternating current could be controlled between 1 and 20 kHz. Equation (1) was used to estimate the induced magnetic field strength (B-field) in the samples. The relative magnetic permeability of the dispersion was estimated to be ~1 for the feasibility studies. This introduced a slight error into the calculations since magnetite NPs in the size range used (10 – 20 nm) have

been shown to have an effective real magnetic permeability of ~1.2 – 1.4 for the dispersion volume fractions tested (Hallouet, Wetzel, and Pelster, 2007). Equations (2) and (3) were used to estimate the theoretical magnetic field strength following the calculation of the *B*-field.

The samples were placed inside of the magnetic field for 4 minutes, and the temperature change was monitored using the IR camera. Two trials of a water control experiment were performed in which no NPs were dispersed in the sample to demonstrate that the frequency is not high enough to heat water via dipole rotation. Ferrotec sold the NPs as a 29 wt% dispersion. The dispersion was diluted down to 20 wt% and 10 wt% for two of the experiments to be reported to demonstrate the effect of NP concentration on the heating rate. The experimental trials resulting in the best heating rates for the low frequency range occurred at a frequency of 1 kHz, and a field amplitude of 11.2 kA m^{-1} (correspondingly a *B*-field of 0.015 T). The results of the heating trials are shown in **Fig. 11**.

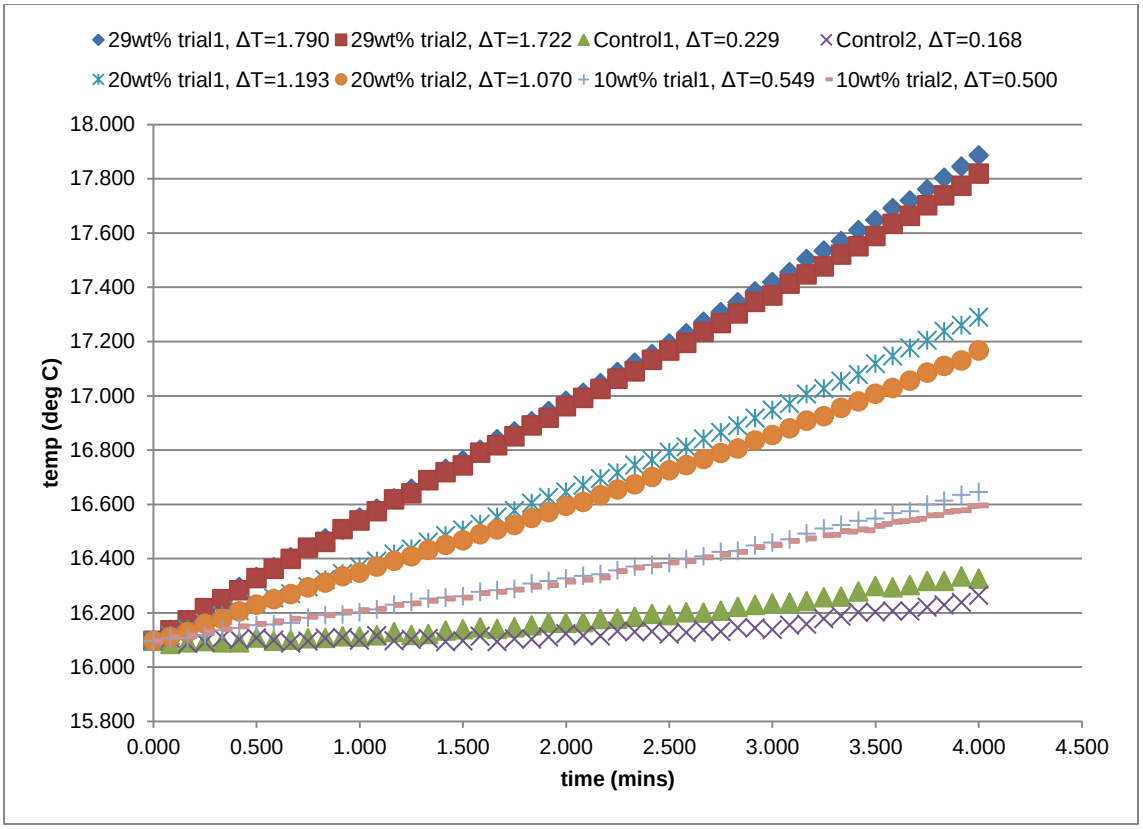

Figure 11–Heating rate for various hydrophilic NP wt%s of EMG700 (Ferrotec) at 1 kHz and 11.2 kA m^{-1}.

Figure 11 clearly shows a positive trend in NP concentration and temperature change. The heat released by the NPs is evident compared to the water control sample, which increased slightly in temperature due to environmental affects – likely residual heat in the solenoid.

To quantify the heating rate from experiment to experiment for different fluids and wt%s the SAR values were calculated for each experimental trial. SAR whose units are $^{W/g_{Fe_3O_4}}$, or the thermal energy absorbed by the dispersing fluid per unit time per gram of iron oxide in the dispersion, is given in a simplified form in Eq. (18).

$$SAR_{static} = \frac{c_p \Delta T}{\Delta t w_{Fe_3O_4}} \tag{18}$$

where c_p is the specific heat capacity of the solvent [J/g °C], ΔT is the change in temperature [°C], Δt is the time elapsed during the experiment [s], and $^{w_{Fe_3O_4}}$ is the weight fraction of magnetite in the dispersion. The SAR for each trial in Fig. 11 should be approximately the same since it is a specific quantity, independent of NP concentration. **Table 3** summarizes the SAR calculations for the experimental trials shown in Fig 11.

Conc., wt%		**ΔT, °C**	**SAR, W g^{-1} Fe_3O_4**
29	Trial 1	1.79	0.108
	Trial 2	1.722	0.104
20	Trial 1	1.193	0.104
	Trial 2	1.07	0.093
10	Trial 1	0.549	0.096
	Trial 2	0.5	0.087

Table 3–Sumary of experimental SAR values obtained for hydrophilic NP dispersions (EMG700 from Ferrotec) at 1 kHz and 11.2 kA m^{-1}.

The largest variance in SAR occurred between the 10 wt% and 29 wt% cases with ~19% difference between trials 2 and 1, respectively. The small overall changes in temperature coupled with the sensitivity of the IR camera to environmental disturbances are likely explanations for this variance. The dominant relaxation mode in these experiments was Brown due to the experimental frequency being at 1 kHz. The usefulness of Brown relaxation at high frequencies is not guaranteed. Overall, these experiments verified that

the Ferrotec NPs are suitable for future induction heating experiments and warranted the scale up of the apparatus.

3.2 High Frequency Apparatus and Dispersion Heating Characterization Experiments

The next stage of the experimental work focused on characterizing the NP heating potential at varying magnetic field strengths and frequencies greater than 100 kHz. A new induction heating apparatus was necessary to achieve frequencies between ~390 kHz and 1000 kHz. The experimental apparatus is an induction heating unit made by Superior Induction, Pasadena, California. The induction heater is the SI-10KWHF model, which has a 10 kilowatt power supply, operates at up to 230 volts, and has an alternating frequency range of approximately 400 – 1000 kHz. The induction heater generates an alternating magnetic field by cycling an alternating current through a coil with a specific number of loops (**Fig. 12**).

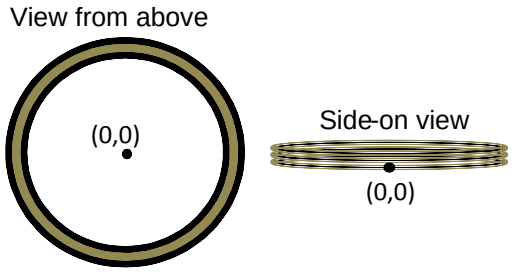

Figure 12—Schematic of batch dispersion sample loading within coil at a relative point of (0,0). All coils used are 10 cm in diameter. The one-turn coil has a vertical height of 1.2 cm; the two-turn coil has a height of 1.8 cm; the three-turn coil has a height of 2.7 cm.

Experiments at different frequencies require switching to different coils with a different number of turns. All coils currently being used have the turn-diameter of 10 cm and have either one, two, or three turns. The one turn coil has a coil vertical length of 1.2 cm; the two turn coil has a length 1.8 cm; the three turn coil has a length of 2.7 cm. The current can be modulated from 3 to 44 Amps depending on the coil being used. The induction heater works in conjunction with a 15 gallon water cooling unit, which circulates chilling water through the coil to prevent overheating and equipment damage.

The heating induced by both types of particles, hydrophilic and hydrophobic, was characterized for frequencies of 390, 540, and 920 kHz at magnetic field strengths ranging from approximately 430 – 5000 A m^{-1} depending on the coil used. For these experiments, the sample was placed at the point (0,0), used as a reference point for the discussion below. A point (r, z) describes the radial position and the height of the sample relative to the bottom of the coil, respectively. Figure 1a demonstrates the location of samples for batch dispersion experiments. Samples were placed here because the field is theoretically strongest at the center of the coil, radially, and at the midway point of the height of the coil. While the sample is placed at the z = 0 location (shown in Fig. 12), it passes through the coil's midway height point since it has a height dimension of about 1 – 2 cm depending on the sample size. After placing the sample at the (0,0) position, it is exposed to the magnetic field for 10 – 30 seconds depending on the strength of the field. The field strength limits the experiment time because samples in a larger magnetic field heat up faster. A dispersion of 10 wt% magnetite NPs in water boils in approximately 10 seconds (100 °C), and a dispersion of 10 wt% particles in hexane boils in approximately 30 seconds (69 °C). In order to modulate the magnetic field strength, the current sent to the coil is varied. The current values used in this case were 5, 15, 25, 35, and 43 Amps. These values of current were used to calculate the magnetic field strength depending on

the number of coil turns and coil length using Eqs. (1) - (3) as was the case in the low frequency experiments.

It is thought that the magnetic field strengths estimated from Eq. (3) are greater than the actual field strengths being produced by the experimental induction coil. (An error in the output current reading from the induction power supply would skew results to yield magnetic field strengths greater than actually present. Since it is believed that the error is inherent to the hardware used, the same error will be represented in future experiments.) An independent measurement of the field strength at the location of the samples was not carried out due to the unavailability of the appropriate equipment. Another potential contributor to error in the magnetic field strength calculations is assuming the relative permeability of the dispersions is ~1. A more sophisticated setup would be necessary to measure the magnetic permeability of the particles.

The first group of experiments was conducted to characterize the heating behavior of the NPs dispersed in batch samples. The magnetic field was applied to each sample for a time up to 30 seconds, and the specific absorption rate (SAR, described in detail with Eqs. (8)) value was calculated for the amount of time that the field was applied. The samples were not allowed to thermally equilibrate since an adiabatic system was not used; thus the steady-state portion of the heating curve, rather than the transient portion was the experimental result of interest. The fluids and relevant fluid properties used for the batch dispersion experiments are shown in **Table 4**. A summary of the batch dispersion experiments performed on both hydrophobic and hydrophilic NPs is included in Tables 5, 6, and 7. **Table 5** contains experimental SAR values obtained for hydrophilic EMG700 NPs dispersed in water; **Table 6** contains experimental SAR values obtained for hydrophobic EMG1400 NPs dispersed in hexane; and **Table 7** contains experimental SAR values obtained for EMG1400 NPs dispersed in THF.

Fluid	ρ, kg/m^3	C_p, J/g K	k, W/m K
Water	999	4.19	0.58
Hexane	655	2.26	0.12
THF	889	1.73	0.14

Table 4—Properties of fluids used for batch dispersion experiments.

H-field, A m^{-1}	400 kHz, W/g	540 kHz, W/g	920 kHz, W/g
556	16.4	10.8	4.84
1667	83.1	48.0	17.8
2778	148	94.1	33.9
4667	199	130	62.7

Table 5—Summary of SAR values obtained for 10 wt% EMG700 (Hydrophilic) nanoparticles dispersed in water.

H-field, A m^{-1}	400 kHz, W/g	540 kHz, W/g	920 kHz, W/g
556	6.59	5.32	2.77
1667	12.1	12.9	9.14
2778	17.0	23.0	19.1
4667	24.8	33.5	28.8

Table 6—Summary of SAR values obtained for 10 wt% EMG1400 (Hydrophobic) nanoparticles dispersed in hexane.

***H*-field, A m^{-1}**	**400 kHz, W/g**	**540 kHz, W/g**	**920 kHz, W/g**
556	4.16	3.34	2.54
1667	12.2	9.43	8.71
2778	21.5	20.7	16.8
4667	27.5	28.2	22.5

Table 7—Summary of SAR values obtained for 10 wt% EMG1400 (Hydrophobic) nanoparticles dispersed in THF.

Next, follows a discussion of the experimental results of the batch heating experiments conducted with hydrophilic and hydrophobic nanoparticles dispersed in different fluids for a range of conditions. The first experimental result shows how the specific absorption rate (SAR) of a sample changes with magnetic field strength and frequency. **Figure 13** shows the results for a 10.5 wt% hydrophobic magnetite sample dispersed in hexane.

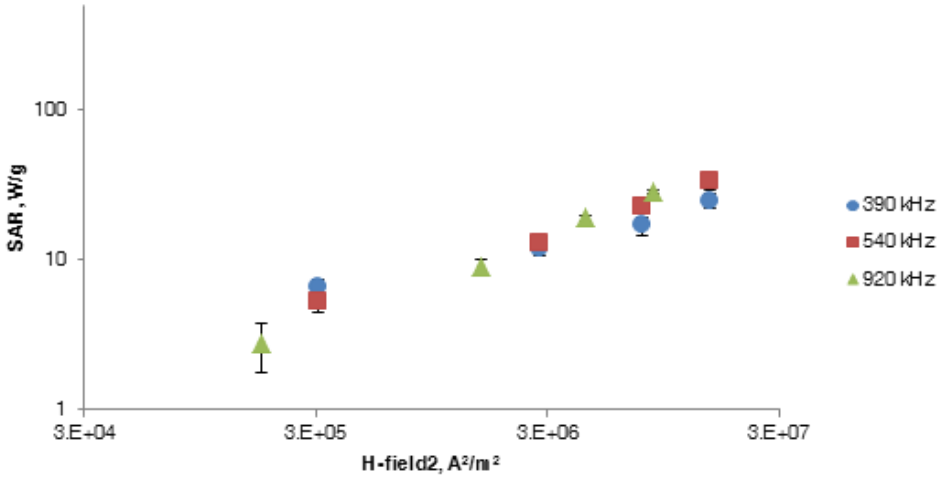

(a)

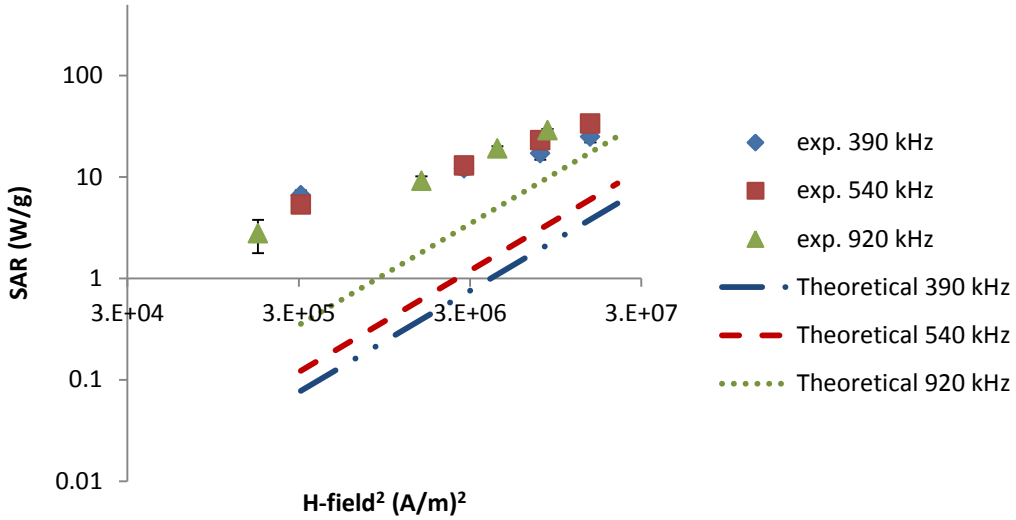

(b)

Figure 13—(a) Variance of experimental (exp.) SAR values with magnetic field strength squared for 10.5 wt% hydrophobic magnetite NPs dispersed in hexane. (b) Data from (a) with theoretical curves from Eq. (10) for a nanoparticle diameter of 8.28 nm.

A sample size of 1 mL was used. The theoretical curves shown in Fig. 5 were calculated using power Eq. (10). Equation (10) represents the energy lost by the NPs, and SAR represents the energy gained by the fluid containing the nanoparticles. It was

assumed that these quantities are equal. A NP core diameter of 8.28 nm was used to calculate theoretical SAR values. The NP core size was taken from the TEM analysis shown in Fig. 10 and summarized in Table 2.

The squared *H*-field values shown in Fig. 13 correspond to relatively small *H*-field values; comparable magnetic flux density values (*B*-field) for the *x*-axis are 0.4 to 6.3 milliteslas. The expected quadratic trends in magnetic field strength (**Fig. 14**) and frequency (**Fig. 15**) were not established.

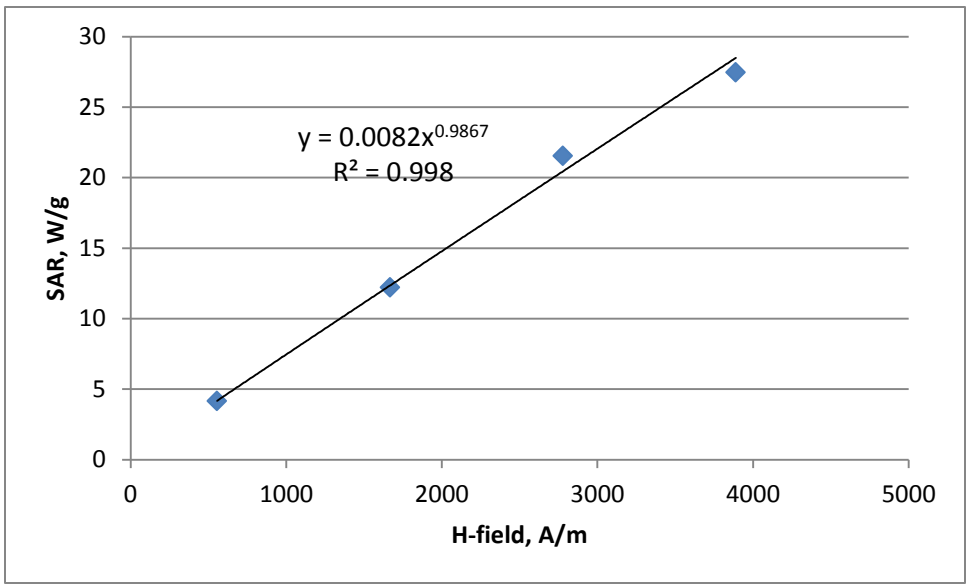

Figure 14–Experimental dependence of SAR on magnetic field strength for hydrophobic NPs dispersed in hexane at a frequency of 390 kHz. The experimental data indicates that SAR ~ H^1.

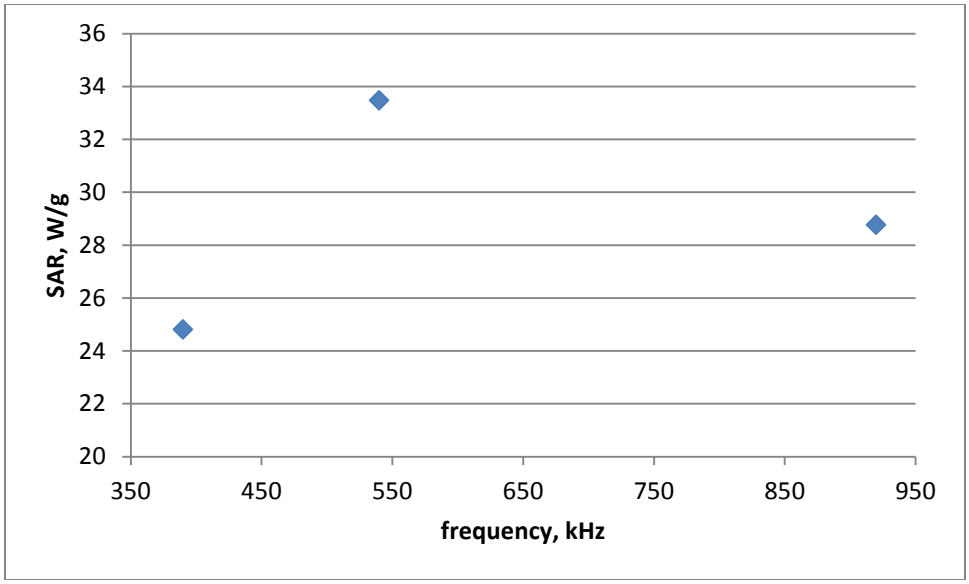

Figure 15–Experimental dependence of SAR on frequency for hydrophobic NPs dispersed in hexane at a magnetic field strength of 3888 A/m. The experimental data shows no correlation in frequency.

Figure 14 indicates a linear dependence of SAR on magnetic field strength as opposed to the theoretically predicted quadratic dependence. The trend is comparable at the higher frequencies. As mentioned in the methods section, an error in the estimated magnetic field strength values could have skewed the SAR values away from the quadratic trend. Figure 15 shows essentially no frequency trend in SAR among the data. A lack of a trend in frequency was also seen at the lower magnetic field strengths. If the 920 kHz data point were removed, an approximate the SAR would have a linear dependence in frequency, which still differs from the expected quadratic dependence in this frequency range. Unknown instabilities in power supply operation could have caused fluctuations in frequency during experimentation which would have scattered the data, however, this is unlikely. A large variation in particle size could also cause SAR values to deviate from the theoretical values (Hergt et al., 2008). Furthermore, it was discussed in Chapter 2.5,

the Theoretical Background chapter, how sensitive heating rate as a function of frequency is to NP size. Given the wide size distribution of the particles, some of the NPs contribute greatly to the overall SAR, while others give off negligible amounts of heat. This could be the reason for the weak trend in frequency compared with the expected theoretical trend. The magnitude of the experimental SAR values in all cases was within an order of magnitude of the theoretical values, and some of the lower frequency experimental SAR values were within error of the theoretically expected values which helps verify the validity of the results.

Next experiments were performed to characterize the hydrophilic magnetite nanoparticles dispersed in water. The EMG700 was diluted down to 10 wt% dispersion (originally 29 wt%). These experiments were performed in exactly the same manner as the hydrophobic NP experiments – by applying magnetic fields from 400 – 5000 A m^{-1} at frequencies of 390, 540, and 920 kHz for 1 mL samples placed at position (0,0). **Figure 16** shows the heating results for the hydrophilic NPs.

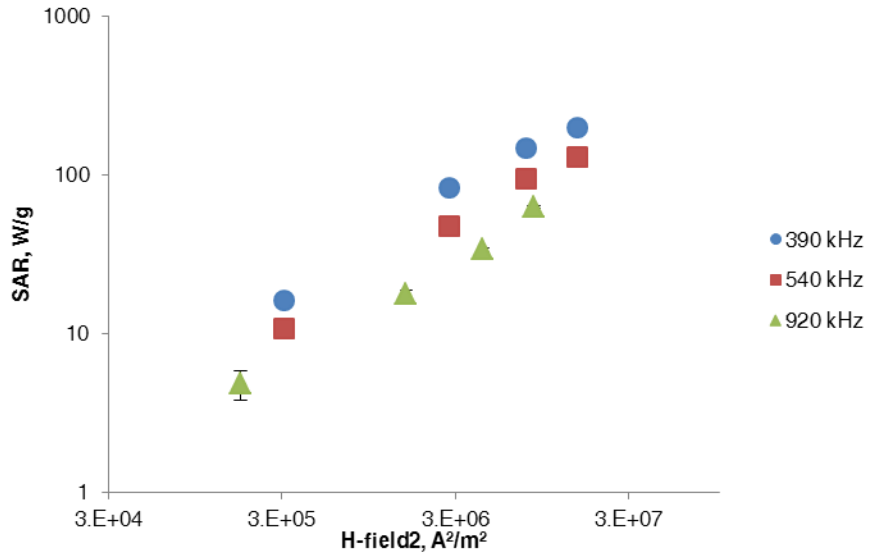

(a)

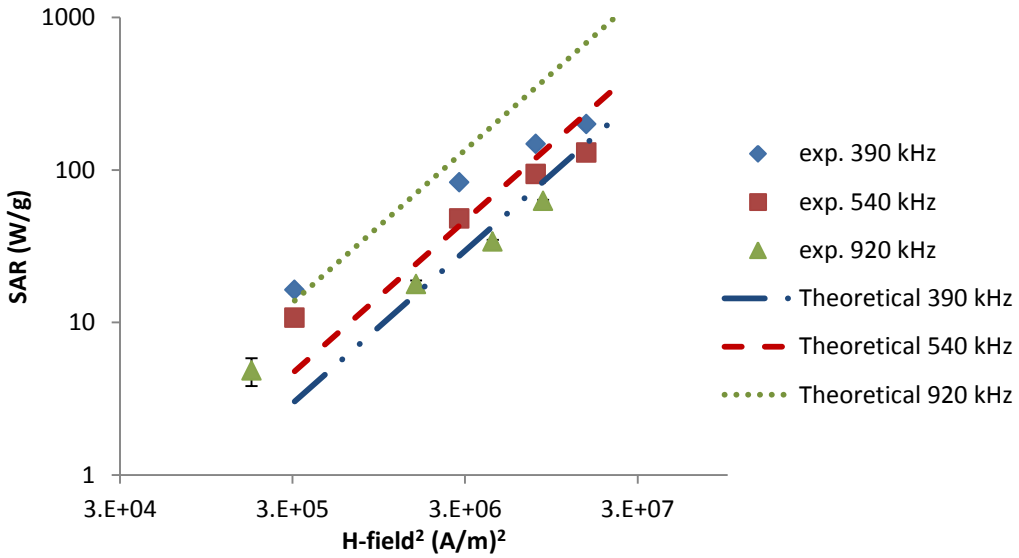

(b)

Figure 16—(a) Experimental SAR values for 10 wt% hydrophilic magnetite NPs in water at varying magnetic fields and frequencies. (b) Theoretical and experimental curves shown for a NP diameter of 14.3 nm.

For both the hydrophobic and hydrophilic NPs, the experimental SAR values did not follow the expected trends in magnetic field strength (**Fig. 17**) or frequency (**Fig. 18**).

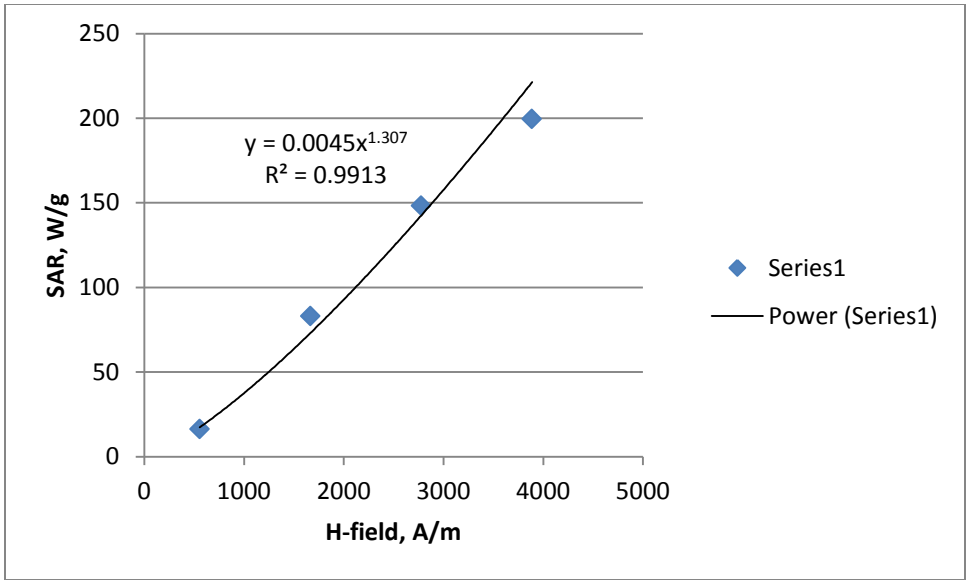

Figure 17–Experimental dependence of SAR on magnetic field strength for hydrophilic NPs dispersed in water at a frequency of 390 kHz. The experimental data indicates that SAR ~ $H^{1.3}$.

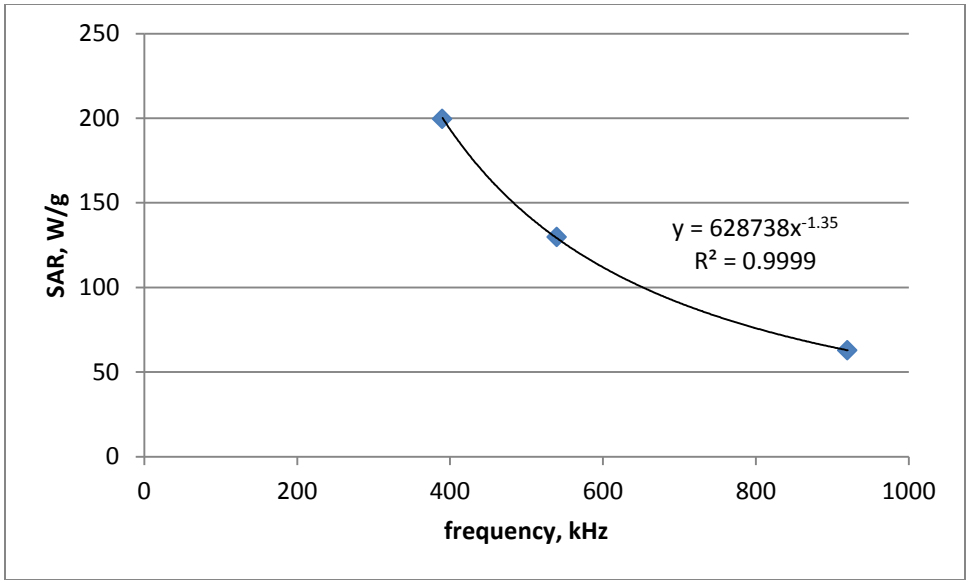

Figure 18–Experimental dependence of SAR on frequency for hydrophilic NPs dispersed in water at a magnetic field strength of 3888 A/m. The experimental data shows a negative correlation in frequency.

Figure 17 shows that once again, the dependence of SAR on magnetic field strength was closer to linear ($SAR \sim H^{1.3}$) than quadratic. The frequency dependence deviated even further from theory for the hydrophilic NPs than the hydrophobic NPs with a negative correlation between SAR and frequency (Fig. 18). The experimental deviation from theory could be attributed to the approximation that Eq. (10) predicts the energy dissipated for a single NP, whereas the experimental system contains a dispersion of multiple NPs. Heat transfer is an important aspect to consider when multiple NPs are dispersed in a fluid and transferring energy to that fluid; the theoretical model employed does not account for this aspect. A section of the modeling chapter of this thesis will analyze this topic.

The results for the hydrophilic and hydrophobic NP heating experiments are shown collectively in **Fig. 19**.

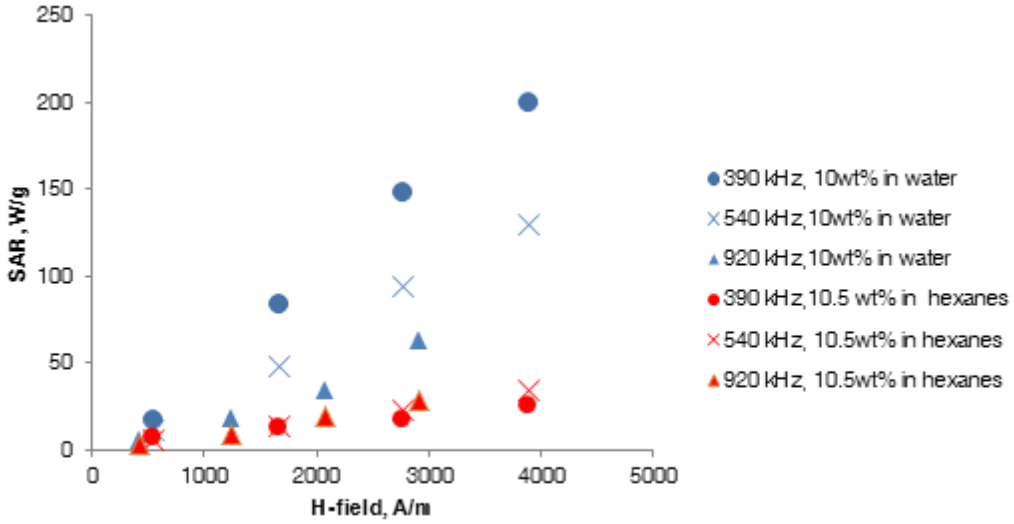

Figure 19—Comparison of SAR values between hydrophilic nanoparticles dispersed in water and hydrophobic nanoparticles dispersed in hexane.

Comparison of the hydrophilic and hydrophobic experimental sets indicates that ample differences in SAR existed between the hydrophilic and hydrophobic NPs regardless of frequency. At a frequency of 390 kHz and a field amplitude of 3888 A m^{-1}, the hydrophilic NPs exhibited a SAR ~8 times greater than the hydrophobic NPs in hexane, which translates to a heating rate increase of ~4 times for the hydrophilic NPs over hydrophobic NPs. The heating rate is the ratio of $\Delta T/\Delta t$. SAR is scaled by the specific heat capacity of the fluid and the NP fluid loading in addition to the heating rate. The specific heat capacity of water is ~2 times higher than hexane, which is why the hydrophilic NP heating rate is four times that of the hydrophobic NP heating rate. This

can be attributed to the large difference in NP size between the two types of particles; the core size of the hydrophobic particles was 8.3 ± 4.3 nm while the core size of the hydrophilic NPs was 14.3± 4.9 nm. A theoretical analysis using the NP size distributions in Figs. 9 and 11 was performed to determine how the large standard deviation and width of the distributions affected the effective theoretical SAR and to determine the validity of the large SAR difference between the two types of particles. The effective SAR for each NP type was calculating by weighing the SLP of each diameter bin by the relative frequency of that bin. By doing this, the SLP contribution of the various diameters was accounted for. An analysis was performed in this manner using Eq. (10) at a field amplitude of 3888 A m^{-1} and a frequency of 390 kHz. The results revealed that hydrophilic NPs with the size distribution shown in Fig. 9 should have an effective SAR of ~72 W/g, and the hydrophobic NPs should have an effective SAR of ~24 W/g. Experimental results at these conditions yielded SAR values of ~190 – 200 W/g and 22 – 28 W/g for the hydrophilic and hydrophobic NPs, respectively.

Performing sensitivity analysis on the hydrophilic TEM image in Fig. 8 yielded that a theoretical SAR of 199 W/g is possible if the NP size threshold were adjusted to 11 nm < D_p < 18 nm; meaning only NP sizes within this range were considered for the size analysis process. The original NP size analysis threshold range was set to 3 nm < D_p < 20 nm, so a much narrower size range was necessary to produce a SAR match. The mean NP diameter of the matched distribution fit yielding 199 W/g was 14.7 ± 2.3 nm. The sensitivity analyses show that the large standard deviation of the original size measurements seems to be contributing factor to the discrepancy between experimental and theoretical SAR values. While the particle size analysis via TEM cannot yield theoretical results that exactly match the experiments without some significant image threshold adjustments, it gives a good idea what the primary cause of the large SAR

variance between the two types of particles is; especially since there is a large degree of judgment that goes into choosing image processing parameters for TEM analysis. A sensitivity analysis was not necessary for the hydrophobic NPs since the experimental and theoretical values approximately matched.

Chapter 4: Nanopaint Experiments

This chapter will describe in detail the experiments in which nanoparticles were embedded in an epoxy resin, dubbed "nanopaint." Experiments were performed on fluids in both a static and flowing system to evaluate the transient and steady state heat transfer properties of the nanopaint. These experiments were also a useful tool to represent hydrocarbon flow through a pipeline as well as when flow has stopped within the pipeline.

4.1 MATERIALS AND METHODS

A solid/nanoparticle paint composite ("nanopaint") makes it possible to coat substrate surfaces for the heating experiments. The "nanopaint" was made in a stepwise manner so that the weight percentage of magnetite of the final product could be controlled. First, hydrophobic magnetite NPs were loaded into a known, superb dispersant for these hydrophobic NPs, toluene. Hydrophobic NPs were selected because it is necessary to keep them from re-dispersing into water after the paint treatment. Toluene was used not only because it is a good dispersant, but also because the epoxy resin used to complete the paint already contains 17 wt% in aromatics (it was assumed that the addition of an aromatic solvent would act as a resin diluent). The toluene loaded with particles was added to the epoxy resin (Sherwin-Williams Macropoxy 646) in proportions so that the end product gave a high weight percentage toluene while maintained a thick enough resin base. For this case, the final diluted, magnetite-loaded

resin product was estimated at 20.2 wt% magnetite. Mixing of the diluent with resin was promoted by stirring in a container. It is important to note that after curing, all of the toluene evaporates, so the magnetite weight percentage of the dry paint increased to ~30 wt% as shown by the experimental model. Paint weight percentages of magnetite from here pertain to the cured weight percentage. The thermal conductivity of the nanopaint was calculated using Maxwell's effective medium theory (Eq. (19); Bird, Stewart, and Lightfoot, 2007).

$$k_{N\text{paint}} = k_{epoxy} + \frac{\varphi_{NP}}{\frac{1}{k_{NP} - k_{epoxy}} + \frac{1-\varphi_{NP}}{3k_{epoxy}}} \tag{19}$$

where ϕ_{NP} is the volume fraction on NPs in the nanopaint, k_{epoxy} is the thermal conductivity of the epoxy resin (0.19 W m^{-1} K^{-1}), and k_{NP} is the thermal conductivity of the NPs (9.7 W m^{-1} K^{-1}). The calculated value of k_{NP} is 0.24 W m^{-1} K^{-1}.

With the nanopaint, a static heating experimental case was first performed. A 1.5-in. central section of the inside wall of a 1-in. ID PVC coupling tube was painted with 30 wt% magnetite nanopaint. Approximately 2.25 g of nanopaint (0.68 g of NPs) were added to the interior wall in as uniform a means as possible. The estimated nanopaint thickness is between 200 and 600 micrometers based on the curing properties of the epoxy resin. All static heating experiments were done using the three-turn coil restricting the measurement frequency to 430 kHz. This was considered necessary so that longer painted sections within the tube could be analyzed. The cylindrical, painted, PVC tube

was placed at the center of the magnetic induction coil with the center of the painted section within the length of the coil, as shown in **Fig. 20**.

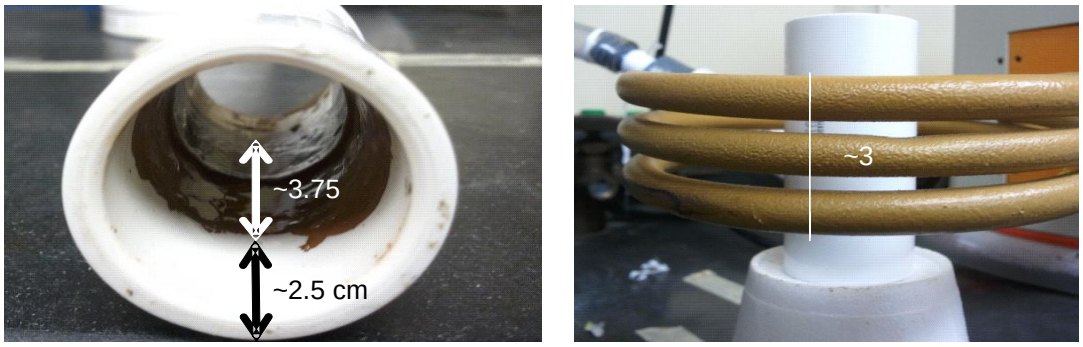

Figure 20—Painted tube positioning within coil for static SAR experiments. The internal painted length is centralized within the length of the coil.

The bottom of the PVC coupling was plugged and sealed using a silicon sealant so that it could be filled with water. For each experimental trial, 25 mL of water was filled in the tube, which placed the water level at the top of the painted section. The lower portion of the tube, outside of the coil length, was unpainted. The temperature measurement probe was placed at the radial center of the tube, and at the center of the painted section with respect to length to ensure consistency among trials (as shown in **Fig. 21**). The magnetic field for each trial was applied for 100 seconds.

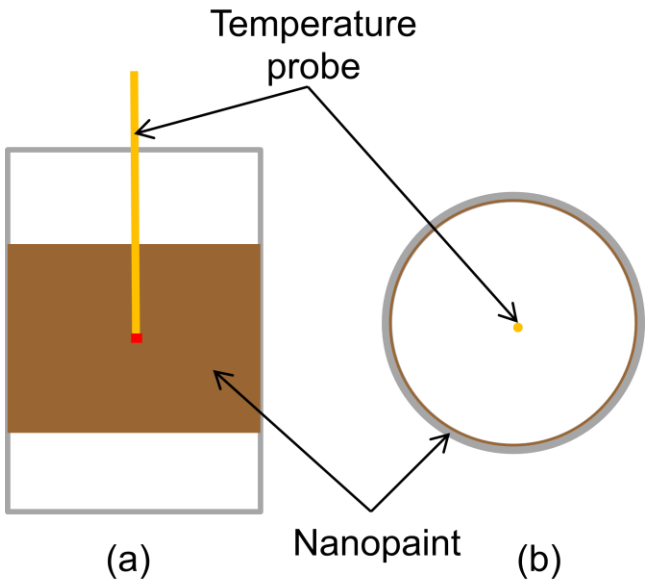

Figure 21—Positioning of the temperature probe for static nanopainted tube heating trials; (a) shows an interior 2D projection of the tube from the side, and (b) shows the cross-sectional view from above.

The next group of experiments was run using a one pass flow system. Tap water was flowed from a tap into a bucket with overflow outlets so that a constant head could be maintained at each desired flow rate to be tested. The bucket was connected to a flow line, which was connected to the flow tube. The flow tube, whose inner surface is coated with approximately 200 - 600 µm of nanopaint, was positioned within the coil in a diagonal fashion as shown in **Fig. 22** to prevent a kink in the tubing upstream of the nanopainted tube.

Figure 22—The painted tube was placed diagonally through the coil so that a slightly longer painted section could be stimulated by the magnetic field, and to prevent a kink in the tubing upstream of the tube. The white box shows where the nanopaint is within the tube. The white circle indicates the point where temperature measurements were taken.

A hole for the temperature probe was cored in a tubing connector, and the temperature of the flowing water was monitored 5 cm downstream of the nanopainted tube before and while the magnetic field was applied, so that a change in temperature due to heat generated by the nanopaint could be quantified. This is the equivalent of monitoring an upstream and downstream temperature since the inflow temperature is constant with time. All temperature differences reported as "ΔT" in the flow system results were measured in this way. Prior to each experiment, the system flow rate was verified as steady state by ensuring that the outlet flowrate did not vary by more than 5% for three measurements at one minute intervals. The temperature upstream of the nanopainted tube was also monitored until reaching a steady value. Once the flow rate and temperature were at steady state, the magnetic field was turned on and the downstream temperature was monitored for several minutes. The length of each experiment varied but lasted until a steady downstream temperature was maintained for 60 seconds.

Table 8 summarizes the range of flow rates, corresponding Reynolds numbers, and residence times through the painted section.

Flow Rate, mL/s	Fluid Velocity, cm/s	Re	Residence time, s
0	0.00	0	0.00
2.5	0.47	122	7.96
5	0.94	245	3.98
7.5	1.41	367	2.65
10	1.88	490	1.99
15	2.83	735	1.33
20	3.77	979	1.00
25	4.71	1224	0.80
35	6.59	1714	0.57
40	7.53	1959	0.50

Table 8—Summary of the range of flow rates and corresponding flow characteristics tested for flowing SAR experimental trials.

The length of painted tube is only ~1.5 inches. The key parameter to consider when inspecting Table 8 is the residence time. This is the amount of time that a given volume of flowing fluid is exposed to the heat-generating nanopaint section. The flow rates tested were all within the laminar regime, approaching the transition flow regime at the largest rates. The experiments were run in this manner so that measurable temperature changes could be detected by the temperature probe being used. If a longer coil were available, then correspondingly, a longer painted section could have been utilized, and a broader range of flow rates would be possible for testing.

For the flowing SAR experimental trials, temperature measurements were made at the wall and at the center of the flow pathway. Temperature measurement at two points was done as a secondary method to evaluate the flow regime, as well as the heat transfer taking place. **Table 9** contains a summary of the differential temperature in the flow system obtained for the temperature probe placed at the center of the flow pathway; **Table 10** contains the differential temperature in the flow system for the probe at the wall of the flow pathway. The positioning of the temperature probe is shown in **Fig. 23**.

***H*-field = 1667 A m^{-1}**		***H*-field = 2778 A m^{-1}**		***H*-field = 4667 A m^{-1}**	
Flow rate, mL/s	**Δ*T*, K**	**Flow rate, mL/s**	**Δ*T*, K**	**Flow rate, mL/s**	**Δ*T*, K**
3.3	1.5	3.67	2.5	5.7	2.4
8.2	0.94	11.9	1.1	13.7	1.2
13.2	0.21	21.9	0.25	19.9	0.25
20.9	0.08	27.3	0.21	27	0.13
42	0.08	34.4	0.20	55	0.08

Table 9—Summary of the differential temperatures in the flow system with the temperature probe at the center of flow pathway.

H-field = 1667 A m^{-1}		*H*-field = 2778 A m^{-1}		*H*-field = 4667 A m^{-1}	
Flow rate, mL/s	**Δ*T*, K**	**Flow rate, mL/s**	**Δ*T*, K**	**Flow rate, mL/s**	**Δ*T*, K**
3	2.6	5.3	5.6	4.8	6.9
5.8	2.9	8.4	3.4	10.1	4.0
11.4	0.35	13.3	0.45	13	0.41
16.5	0.12	23.8	0.12	17	0.37
-	-	36.6	0.12	34.4	0.16

Table 10— Summary of the differential temperatures in the flow system with the temperature probe at the wall of flow pathway.

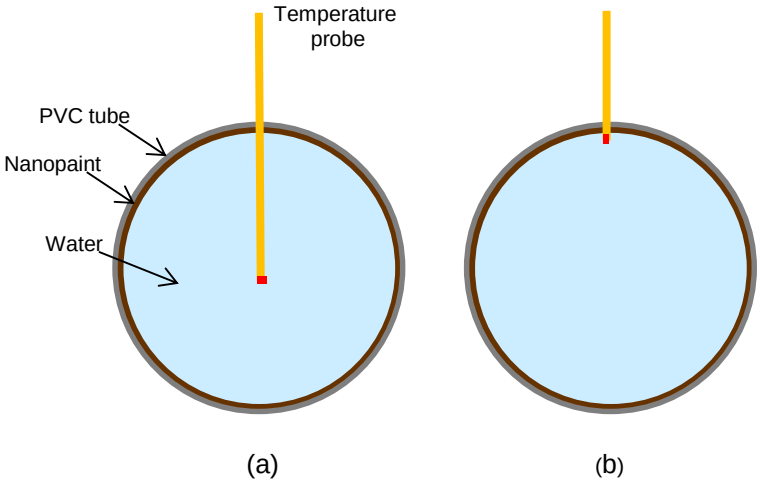

Figure 23—Cross section of the nanopainted flow tube showing the position of the temperature probe at the center of the flow pathway (a) and at the wall (b).

4.2 EXPERIMENTAL ANALYSIS OF NANOPAINTED TUBE HEATING OF A STATIC FLUID

The following experiments were performed to demonstrate the ability for the superparamagnetic NPs to be embedded in a solid, thus making them stationary, and still give off considerable amounts of heat. Water was selected as the fluid in all of the following experimental cases due to its high thermal conductivity.

First, static SAR experiments were performed using the nanopainted PVC tube as described in the methods section. **Figure 24** displays the static nanopaint transient heating curves for each magnetic field tested, and **Fig. 25** shows the SAR values obtained for the heating rates obtained from the transient curves.

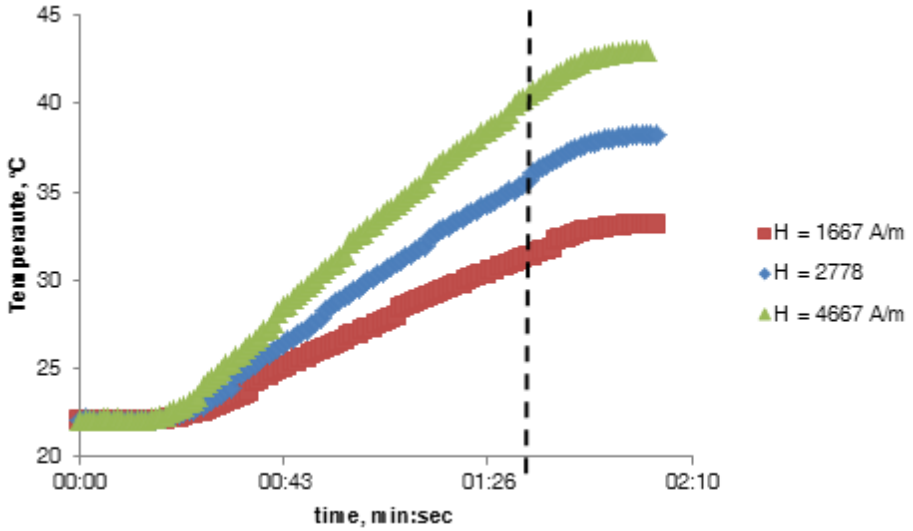

Figure 24—Transient heating curves for static water samples in nanopainted tube at a frequency of 430 kHz; magnetic field strengths shown are theoretical. The dotted line indicates the point in time when the magnetic field was turned off.

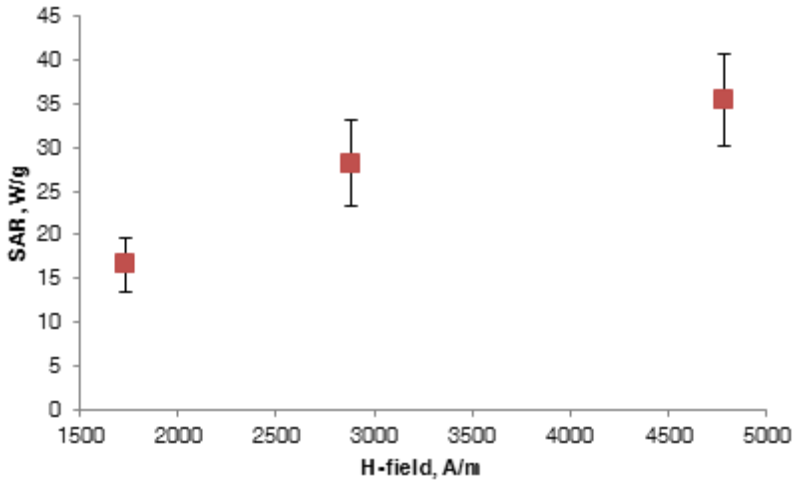

Figure 25—Static SAR as a function of magnetic field strength at a frequency of 430 kHz for a nanopainted tube filled with water.

The heating curves shown in Fig. 24 represent a single trial of the several run at each respective magnetic field strength. Static SAR values were calculated from the linear portion of the heating curve. The heating curves indicate that it takes slightly longer for heating behavior to exit the transient state for lower magnetic field amplitudes, but once a steady heating rate is reached, it is maintained until the magnetic power is turned off. Furthermore, the heating curves in Fig. 24 indicate a reduction in the effectiveness of heating at higher magnetic field strengths; this is interpreted qualitatively from the heating rates of the two upper magnetic field strengths being closer in value than the two lower magnetic field strengths.

Figure 25 also shows that there is a decrease in heating effectiveness as the magnetic field strength is increased. It is hypothesized that while the particles at the wall generate more heat at higher field amplitudes, the heat transfer is conduction and free-

convection limited since there is no mechanical mixing within the system. Also, the thermal conductivity of the nanopaint is approximately three times lower than that of water, which limits the heat transfer rate between the two. It is also possible that the actual magnetic field strength is not as high as calculated due to a difference in the relative permeability of the NPs as was mentioned in the methods section of the dispersion heating experiments.

Figures 24 and 25 show that the SAR values are not intrinsic to the NPs used, but also dependent on the heat transfer behavior of the system in which NPs are deployed or embedded. This is supported by the previous experiments in which the NPs were dispersed evenly throughout the solvent rather than embedded at the wall. When the particles were dispersed, each NP heated up a small differential volume of target fluid, and superposition of the heat generated in each differential volume resulted in a much larger overall fluid temperature, and thus larger SAR values. The spatial distribution of the particles and the thermal properties of the nanopaint and fluid greatly affect the resulting SAR values. The heat transfer properties of the system will be analyzed in the modeling section of this thesis to give a better understanding of the theoretical transport phenomena taking place.

4.3 Experimental Analysis of Nanopainted Tube Heating a Flowing Fluid

Next, the nanopainted tube was placed in the single pass flow system described in the experimental methods. The three-turn, 430 kHz coil was used for these experiments, as well, to increase the residence time of the fluid in contact with the nanopaint. Since all flow rates tested are within the laminar flow regime, the temperature probe was first

positioned within 1 mm of the wall for three different magnetic field strengths, and then the probe was moved to the center of the flow pathway for the same magnetic field strengths. Temperature measurements at these points enabled evaluation of the assumed flow regime, as well as an analysis of the heat transfer taking place. **Figure 26** illustrates the fluid temperature at the wall as a function of flow rate at varying magnetic field strengths.

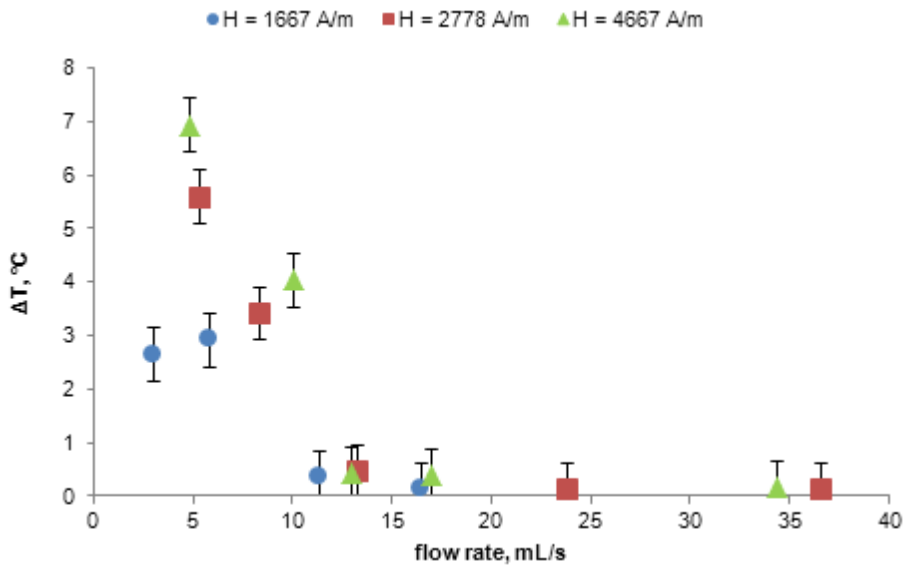

Figure 26—Temperature profiles at the nanopainted tube wall for water flowing at various flow rates and at varying magnetic field strength.

As expected, for all cases except the lowest magnetic field strength, the temperature of the fluid at the wall decreased as the flow rate was increased. The slight increase in temperature for the 1667 A m^{-1} case from a flow rate of 3 – 6 mL/s may be attributed to a measurement error. The fluid temperature at the center of the flow pathway is shown in

Fig. 27, in which the overlapping temperature profiles of the 2778 and 4667 A m^{-1} cases stand out.

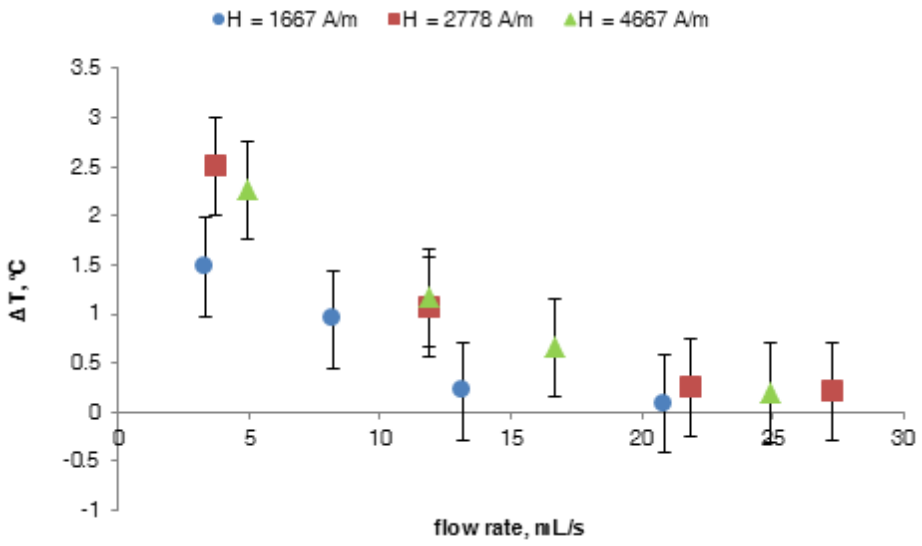

Figure 27—Temperature profiles at the center of the flow pathway for water heated by the nanopainted tube wall. The water flow rate and magnetic field strength were varied.

At flow rates approximately less than 12 mL/s, these magnetic field strengths exhibited a wall temperature increase with increasing magnetic field strength (Fig. 26). However, Fig. 27 shows that approximately the same amount of heat was transferred to the water at the center of the flow pathway for both magnetic field strengths. Above a flow rate of approximately 15 mL/s, the heat transferred to the water at the center of the flow pathway as well as near the wall steadily decreased until the heat transferred converged to a minimum. When compared to the temperature difference at the wall for each magnetic field strength, Fig. 27 indicates a constraint on the heat transfer taking place between the wall and the fluid. The laminar flow regime hinders mixing, and the

short residence time at higher flow rates prevents ample contact time between the fluid and the nanopaint. Increasing the heated surface area, as well as introducing heated surfaces at the center of the flow pathway would help to promote heating to the full flow profile in the absence of mixing; however, introducing objects to the center of flow pathway is not practical from field engineering standpoint.

Steady state flowing SAR values were calculated for each flow rate and magnetic field strength so that a comparison with static SAR values could be made. The flowing SAR values were calculated using the same principles as the static SAR values; the only difference being a flow rate instead of a static volume being heated over a time interval. The temperature at the center of the flow pathway was used to calculate the flowing SAR values defined below.

$$SAR_{flow} = \frac{\rho \dot{V} c_p \Delta T}{m_{Fe_3O_4}} \tag{20}$$

where ρ is the density of water [g mL^{-1}], $\dot{V}$ is the volumetric flow rate [mL s^{-1}], ΔT [K] is the change in temperature from the onset of the magnetic field until a steady state temperature is reached, and $m_{Fe_3O_4}$ [g] is the mass of magnetite nanparticles in the painted section.

Figure 28 shows the variation of flowing SAR values at various flow rates tested, as well as the ratio of the flowing SAR to static SAR.

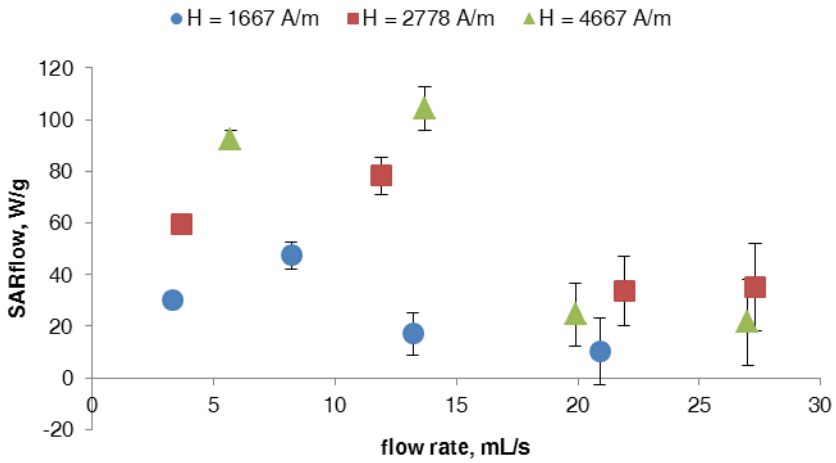

(a)

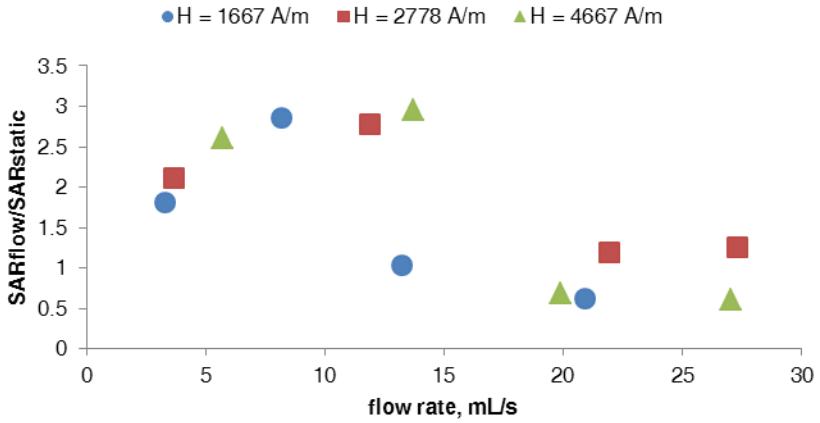

(b)

Fig. 28—(a) Variation of flowing SAR with flow rate; (b) ratio of flowing to static SAR for the same flow rates and for the three magnetic field strengths tested.

The flowing SAR curves in Fig. 28 indicate that the maximum heat transfer at the center of the flow pathway for the system took place between approximately 8 and 13 mL/s. This is unexpected for a purely laminar flow regime. The flowing SAR values are up to three times larger than static SAR values at their respective magnetic field strengths,

which indicates an increase in heat transfer in the flowing system. For purely laminar flow, the maximum amount of heat transfer should have occurred at the lowest flow rate since the largest residence time between the fluid and the heating wall is at this flow rate. A maximum SAR at an intermediate flow rate indicates that some mixing was induced, even at sub-turbulent flow velocities, which increased the rate of heat transfer from the wall to the interior fluid layers. Modeling of the flow system in the next chapter will indicate if this conjecture is correct.

Mixing could have been induced by a slight constriction in the system due to changing from 1-in. coupling to ¾-in. tubing, 1 cm upstream from the temperature measurement point (shown in Fig. 22). It is hypothesized that a flow rate between 8 and 13 mL/s was the minimum required to induce the eddy currents to form at the constriction in the flow pathway, which is why this maximum in SAR occurred here. At higher flow velocities, mixing continued to occur, but the residence contact time between the fluid and the heated wall decreased so much that sufficient heat transfer did not take place.

A longer 1in. ID PVC coupling tube could be nanopainted to ensure that the flow regime has fully developed, and constrictions/expansions are not close enough. In the flowing fluid experiments, a larger temperature gradient also existed between the nanopaint and the fluid layer contacting the nanopaint since the same fluid layer was not in contact with the nanopaint the whole experiment (as was the case for the static experiments). This could have also contributed to the increased heat transfer for the flow experiments.

Chapter 5: Computational Modeling of Dispersion and Nanopaint Experiments

This chapter will present the computational modeling work using COMSOL v4.1a, a finite element modeling software package, used to evaluate the physical phenomena that occurred during the experiments presented. The models help identify the most sensitive experimental variables and parameters, which is important knowledge for scaling up dimensions. The procedure for generating a model in COMSOL follows these basic steps:

1) Input of model parameters and definitions.
2) Build model geometry.
3) Assign appropriate boundary conditions.
4) Mesh model geometry.
5) Solve appropriate partial differential equations via finite elemental analysis.
6) Analyze and process results.

The key model inputs, equations, and boundary conditions will be described for each experimental model generated, as well as a discussion of the result.

5.1 DISPERSED NANOPARTICLE EXPERIMENTAL MODEL

The dispersed NP experiments are mathematically represented by the transient heat diffusion equation for conduction. We first investigated the problem of heat transfer from the heat-generating nanoparticle (assumed to be a sphere) to the surrounding dispersing medium. The physics of a macroscopic fluid dispersion can be described by a single spherical NP in a finite fluid sphere whose diameter scales with the wt% of the

NPs in the dispersion: In view of the small particle/solvent volume ratio, this simplified view of the problem adequate with a proper selection of the proper boundary conditions. COMSOL used a form of Eq. (13) in spherical coordinates to represent the conduction problem as shown in Eq. (21).

$$\rho C_p \frac{\partial T}{\partial t} - \frac{k}{r}\frac{\partial}{\partial r}\left(r^2 \frac{\partial T}{\partial r}\right) = Q_{NP} \tag{21}$$

where r is the radial position within the system [m], T is the temperature [K], k is the thermal conductivity [W m^{-1} K^{-1}], ρ is the density [kg m^{-3}], C_p is the specific heat capacity [J kg^{-1} K^{-1}], and t is time [s], and Q is the heat source [W m^{-3}]. An illustration of the NP within the fluid sphere is shown in **Fig. 29**:

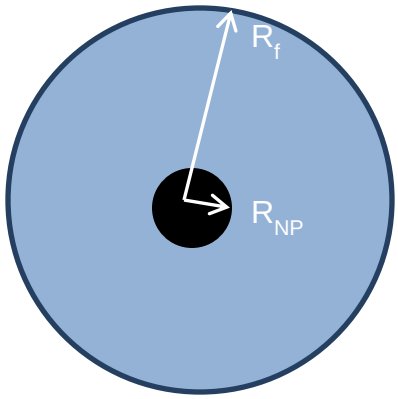

Figure 29–Illustration of the NP dispersion heating model, which is represented by a single NP with radius R_{NP} enclosed in a finite fluid sphere of radius R_f.

Selection of the appropriate boundary conditions is what enables a single NP in a finite fluid sphere to represent a dispersion of numerous NPs. At the NP-fluid sphere interface, $r = R_{NP}$, continuity of heat flux is maintained. Continuity of heat flux is

necessary at this boundary since heat is being produced within the NP, and any heat that leaves the NP is transferred to the surrounding fluid. This boundary condition is represented by Eq. (22).

$$k_{NP}\left(\frac{\partial T}{\partial r}\right)\Big|_{r=R_{NP}} = k_f\left(\frac{\partial T}{\partial r}\right)\Big|_{r=R_{NP}} \tag{22}$$

where k_{NP} and k_f represent the thermal conductivities of the NP and fluid, respectively. The second essential boundary condition describes the zero heat flux at the fluid sphere boundary.

$$q = 0\big|_{r=R_f} \tag{23}$$

This approximate model represents a dispersion of equal size NPs, each representing a heat generation source, and the heat travels to the fluid sphere boundary at the same rate for each sphere. Thus, at the fluid boundary of any neighboring NPs, the temperature will be equivalent, which eliminates the gradient and results in a no flux boundary condition. In the actual experimental case, there is a NP size distribution, so the no flux boundaries would vary based on position in the dispersion, but the simple case is adequate in describing the system.

For the experimental case of a 10 wt% dispersion of 13.8 nm diameter hydrophilic NPs in water, the water sphere diameter is 51.4 nm. A NP diameter of 13.8 nm was selected, since this mean size theoretically produced an SLP of 208 W/g, which is the SAR obtained for the experimental case to be matched. This mean size is also within 0.3 nm of the measured NP size distribution mean from TEM imaging. Converting the SAR

to a volumetric heat source using the density of bulk magnetite (5.18 g/mL) yielded a heat source term of $1.077 \cdot 10^9$ W m^{-3}. The COMSOL model inputs for the described experimental case are summarized in **Table 11**.

Parameter	Abbrev.	Value	Unit
NP radius	R_{NP}	6.9	nm
Fluid radius	R_f	25.7	nm
NP thermal conductivity	k_{NP}	9.7	W m^{-1} K^{-1}
water thermal conductivity	k_f	0.58	W m^{-1} K^{-1}
NP heat capacity	$C_{p,\,NP}$	0.653	J g^{-1} K^{-1} (25 C)
water heat capacity	$C_{p,\,f}$	4.186	J g^{-1} K^{-1} (25 C)
NP heat source	Q_{NP}	$1.08 \cdot 10^9$	W m^{-3}
frequency	f	430	kHz
H-field	H	4667	A m^{-1}
Exp. Time	t	100	s

Table 11–COMSOL model parameters for 10 wt% dispersion of hydrophilic NPs in water.

The thermal conductivity of the magnetite NPs is over an order of magnitude larger than that of water, so heat will quickly dissipate from the source to the surrounding

fluid; for this reason, the temperature profile within the NP should be nearly uniform as a function of radius.

Following meshing of the geometry similar to the one shown in Fig. 29, COMSOL solved Eq. 21 for each element in the mesh using the appropriate boundary conditions. An example of a resulting temperature surface plot for the experimental case described in Table 11 is shown in **Fig. 30**.

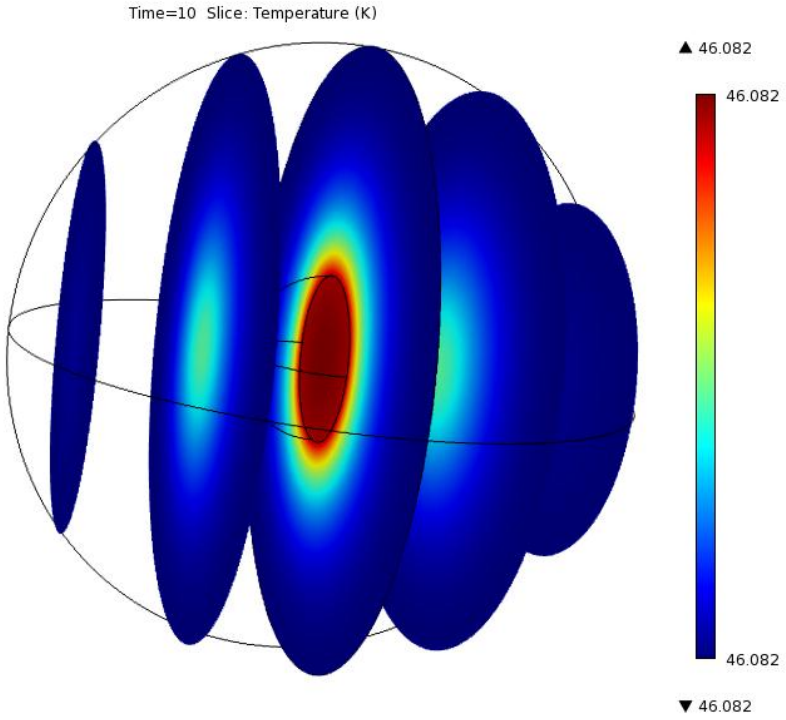

Figure 30–COMSOL temperature surface plot for simulation of 10 wt% hydrophilic NP dispersed in water for the experimental conditions described in Table 11. The temperature surface shown is for a time slice at 10s. Note the temperature scale varies by less than 0.001 °K.

The reason for the uniform temperature distribution as a function of radius throughout the model geometry can be explained by the scale of the model's geometry to the experimental time scale, as will be discussed. First, a comparison of the resulting model heating rate and experimental heating rate will be analyzed (**Fig. 31**).

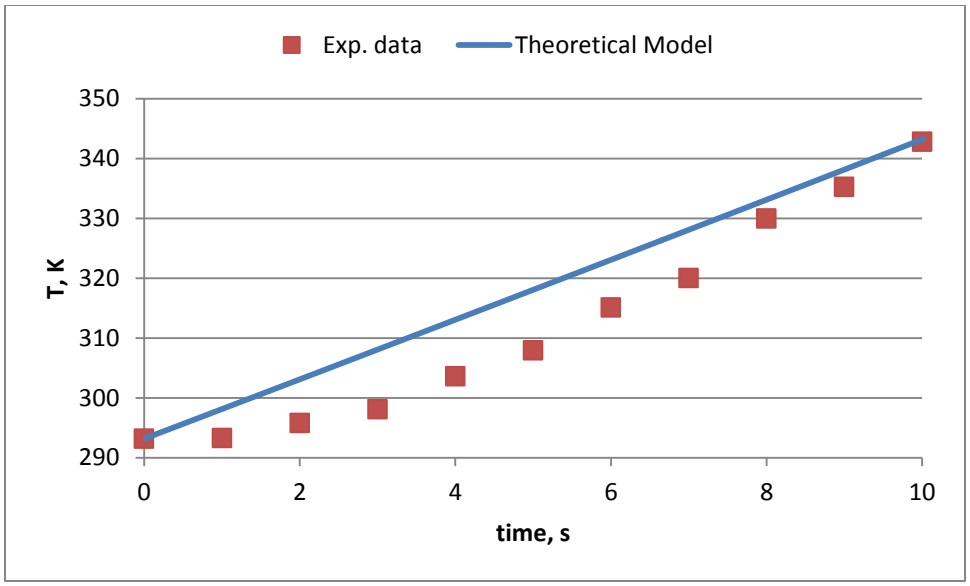

Figure 31–Comparison of experimental heating rate to theoretical COMSOL simulation heating rate for 10 wt% dispersion of 6.9 nm NPs in water (f = 430 kHz; H = 4667 A m^{-1}).

Figure 31 shows that the theoretical model cannot account for the delay in heating of ~1 second exhibited in the experiment. Such is likely due to describing the dispersion from the NP-fluid sphere perspective, rather than a full scale dispersion model with account of neighbor interactions. In doing this, the effects of NP aggregation and the NP size distribution on nanoscale heating could not be captured. The experimental heating rate "catches up" to the theoretical heating rate (which is constant for the time scale shown), which indicates that there is initially an experimental delay in the heating response of the

NPs to the magnetic energy, or the heat transfer of the NPs to the fluid is not as efficient at early times as theoretically expected.

An analysis of the theoretical NP heating rate at the nano and micro time scales will help reveal the effect of the fluid properties on the heating behavior of the system. The size of the fluid sphere surrounding the NP is a function of the NP wt% in the dispersion, so the heating response as a function of wt% will also be investigated. The temperature within the NP-fluid sphere system for a 1 wt% dispersion of 6.9 nm radii hydrophilic NPs in water at nano and micro time scales is shown in **Fig. 32**. The fluid sphere radius for a 1 wt% dispersion of 6.9 nm radii NPs is 55.4 nm.

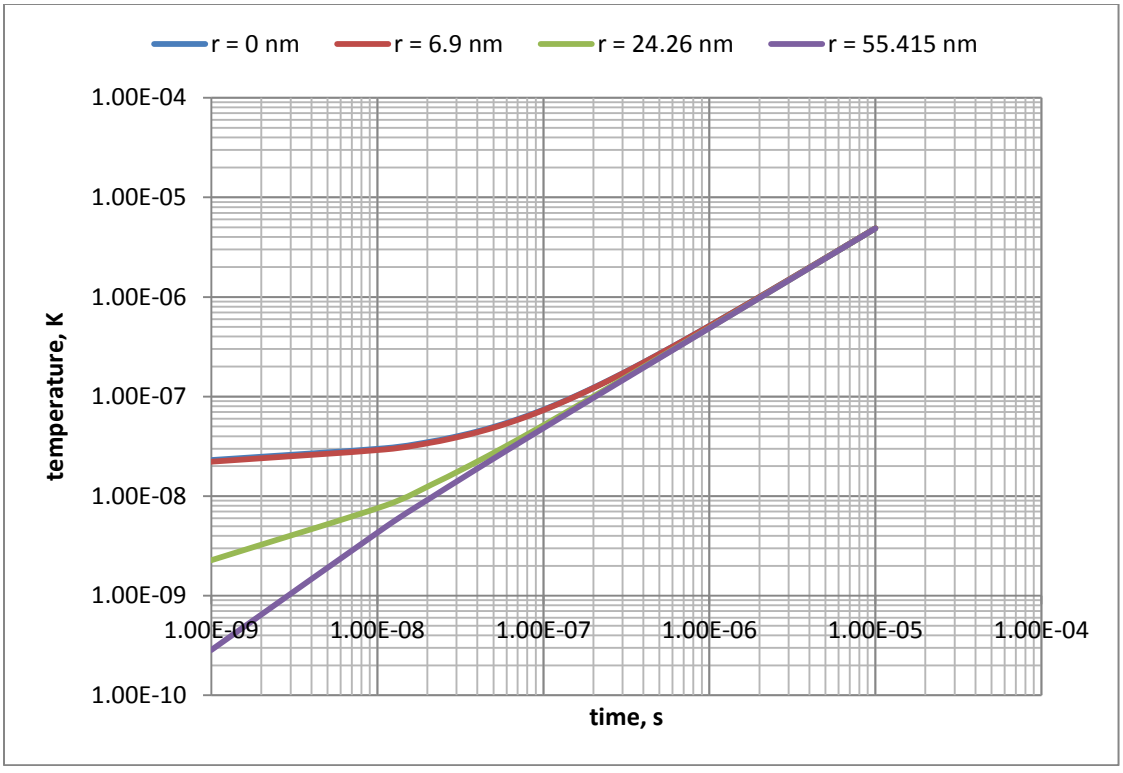

Figure 32–Theoretical NP-fluid temperature distribution for varying radial position within the 1 wt% hydrophilic NP in water dispersion system.

The r = 0 nm and r = 6.9 nm curves are at the center and edge of the NP, respectively. These curves indicate that, as expected, within the NP, regardless of the time, there is minimal temperature variation due to the large thermal conductivity of magnetite. Another essential observation is that there exists a temperature distribution within the water sphere as a function of radius until a critical time, at which point the radial temperature gradient becomes negligible. At this time, the temperature of the whole NP-fluid sphere system increases at approximately the same rate. The heat transfer rate within the fluid sphere is large such that the effect of the fluid thermal conductivity will not influence the macro-time temperature in the system. This further confirms that the significant difference in heating rate (SAR) between the hydrophilic and hydrophobic NPs (and hence Q_{NP}) in Fig. 19 was due to the large difference in mean particle size and distribution, not the difference in thermal conductivities of the fluids. To support the claim that the fluid sphere thermal conductivity has no influence on the resulting macro-time scale temperature rise of the dispersion, the thermal conductivity of the fluid was decreased by a factor of 4 in the simulation (**Fig. 33**).

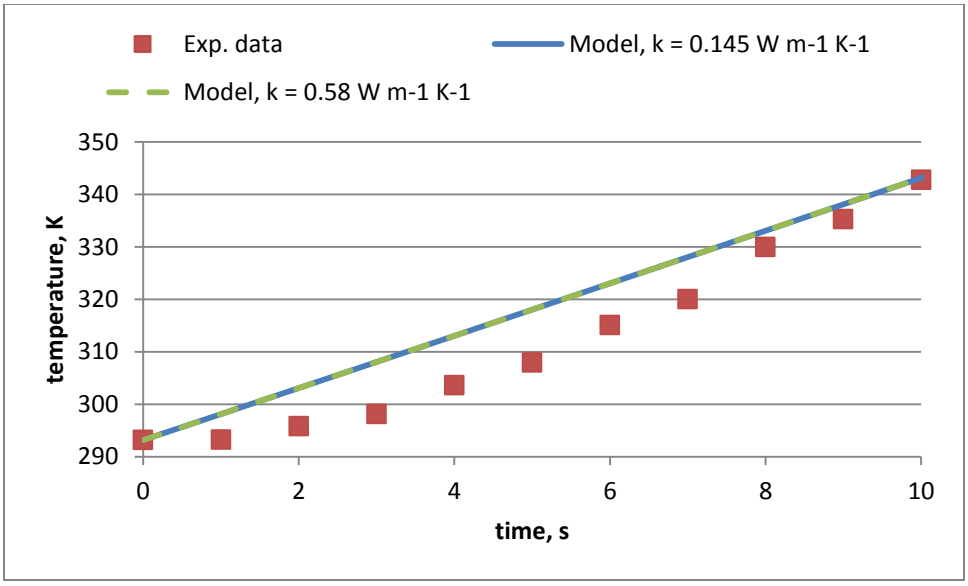

Figure 33–Comparison of 10 wt% NP dispersion experimental data to the representative model for a fluid sphere having two different thermal conductivities.

The two model curves fall directly on top of one another, which is why they are difficult to distinguish in the plot. By changing the thermal conductivity of the fluid by a factor of four, no effect on the temperature rise in the model dispersion resulted.

Since the volumetric dependence on sphere radius is cubic, a two-fold increase in radius results in a dispersion wt% reduction of eight assuming the mass is held constant. Thus, decreasing the NP dispersion wt% to 0.1 results in a fluid sphere radius increase of slightly more than two to 119.4 nm. The radial temperature distribution of the 6.9 nm radius NP dispersion at 0.1 wt% is shown in **Fig. 34**.

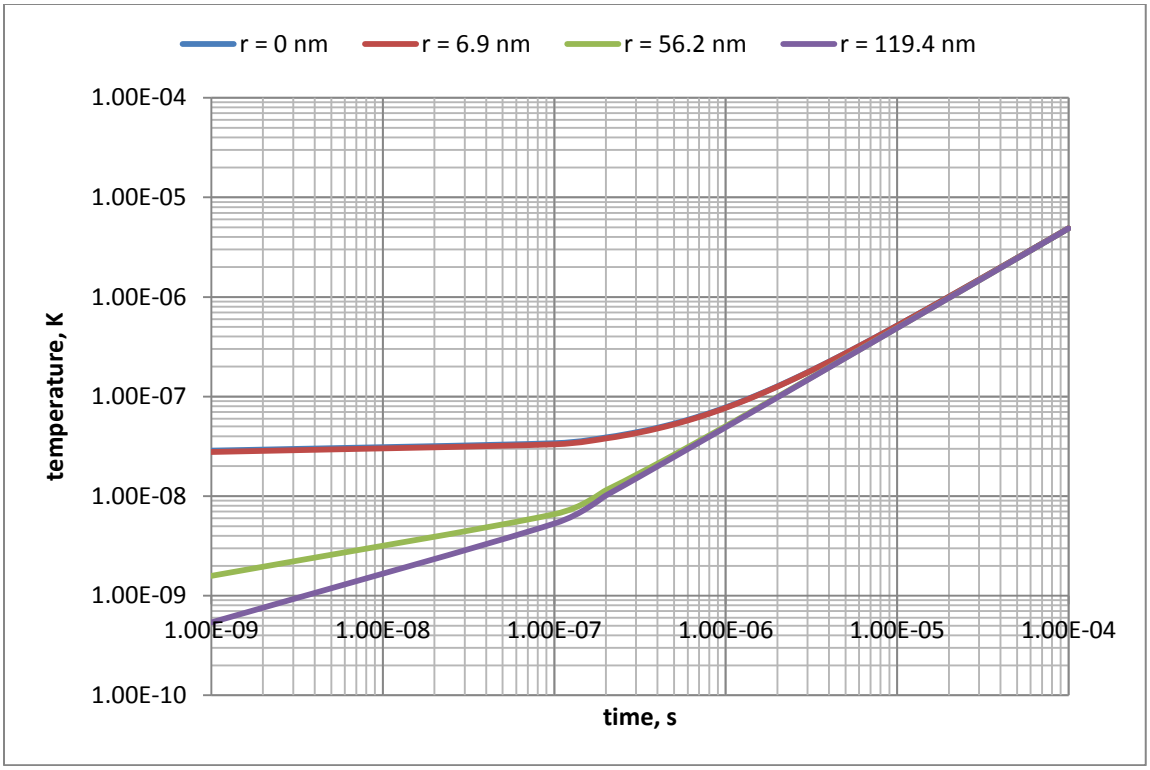

Figure 34–Theoretical NP-fluid temperature distribution for varying radial position within the 0.1 wt% hydrophilic NP in water dispersion system.

The response of the 0.1 wt% NP dispersion system is very similar to the 1 wt% case except for the time at which temperature difference with radial position becomes negligible. Via qualitative inspection, the critical equilibration time for the 0.1 wt% NP dispersion occurs just before $1 \cdot 10^{-5}$ s instead of $1 \cdot 10^{-6}$ s as was the case for the 1 wt% dispersion. Decreasing the NP wt% of the dispersion by 10 caused a delay in the critical time for negligible radial temperature difference by ~10 as well. So, the heat transfer rate is primarily a function of the dispersion wt% (model geometry) as well as the magnetic and NP properties.

The temperature rise in the system as a function of model geometry also holds true at the macro time scale. By increasing the fluid sphere radius from 25.7 nm to 102.8 nm (a four-fold increase, which represents a reduction in NP wt% by 64 times from 10 wt% to ~0.16 wt%), the equilibrated temperature of the system took 64 times as long to achieve the same temperature rise (**Fig. 35**).

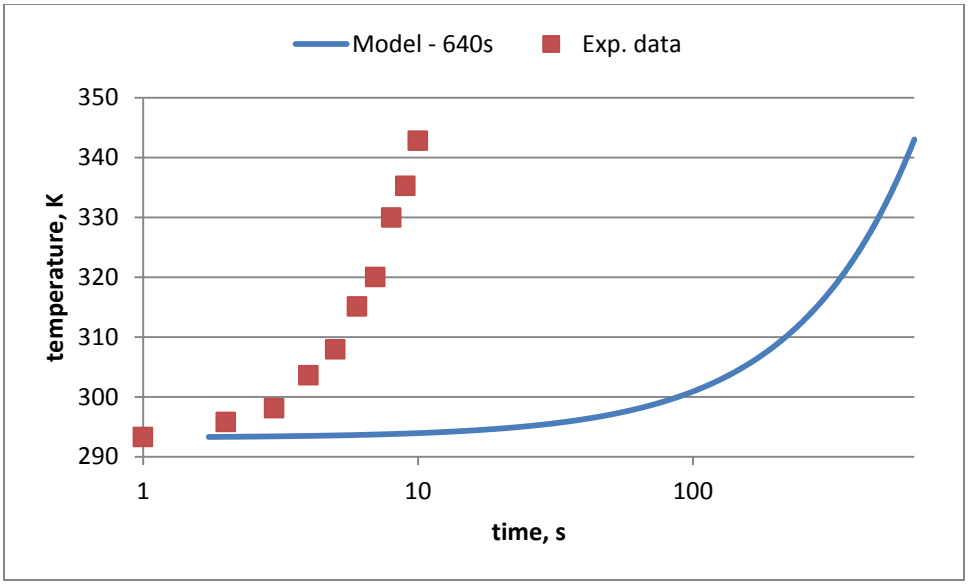

Figure 35–Comparison of 10 wt% NP dispersion (25.7 nm fluid sphere radius) to ~0.16 wt% NP dispersion (102.8 nm fluid sphere radius).

At 640 s, the model temperature rose to the same temperature as the experimental dispersion temperature at 10 s, 343 °K. Fig. 35 reiterates the importance of tailoring wt% to the process for a given set of NP and magnetic conditions so that the appropriate temperature increases are achieved for dispersion heating. To show that (1) the temperature change in the system shifts to linear dependence with time (non-transient behavior) at the macro time scale, and (2) the micro scale model can be applied to macro scale dispersion experiments the following proof was done:

Starting with Eq. (20)

$$\rho C_p \frac{\partial T}{\partial t} - \frac{k}{r}\frac{\partial}{\partial r}\left(r^2 \frac{\partial T}{\partial r}\right) = Q_{NP} \quad [\mathrm{W/m^3}]$$

which reduces to

$$(\rho_{NP} C_{p,NP} V_{NP} + \rho_w C_{p,w} V_w)\frac{\partial T}{\partial t} = \dot{E}_{NP} \quad [\mathrm{W}]$$

once the 2nd order conduction term is dropped (1st order conduction will dominate), and both sides of the equation are integrated by the total volume of the dispersion. Next, the total water volume in the dispersion was reduced to that of the model (microscale) using the following substitution:

$$V_w = V_{sp} - V_{NP}$$

where V_{sp} is the volume of the fluid sphere in Fig. 35.

$$[\rho_{NP} C_{p,NP} V_{NP} + \rho_w C_{p,w}(V_{sp} - V_{NP})]\frac{\partial T}{\partial t} = \dot{E}_{NP}$$

Both sides of the equation were multiplied by $1/(\rho_{NP} V_{NP})$ and reduce to yield the SAR on the right hand side.

$$\left[C_{p,NP} + \rho_w C_{p,w}\frac{(V_{sp} - V_{NP})}{V_{NP}}\right]\frac{\partial T}{\partial t} = SAR$$

The following values were plugged in for the variables: $C_{p,NP}$ = 0.653 J/g K, $C_{p,NP}$ = 4.186 J/g K, ρ_w = 1 g/cm^3, ρ_{NP} = 5.18 J/g K, $V_{sp} = 4.55 \cdot 10^{-21}$, $V_{NP} = 1.38 \cdot 10^{-24}$, ΔT = 50 °K, and Δt = 640 s. This yielded a SAR of 208.8 W/g (or $1.08 \cdot 10^9$ W/m^3 when multiplied by ρ_{NP}), which is the same SAR that was plugged into the model as the heat source term.

5.2 STATIC FLUID HEATING VIA NANOPAINTED TUBE MODEL

COMSOL was again used to generate a model representing the experimental heating of a static fluid via a nanopainted tube. Static fluid heating is mathematically represented by the transient heat conduction equation (Eq. (13)). While the physics of the dispersion heating model were described with respect to a single NP, the nanopainted tube model is physically described macroscopically. The nanopaint is treated as a thin film heat source. The value assigned to the heat source is the theoretical SLP of the NPs weighted by the volume fraction of particles in the nanopaint composite. The mean NP size of the hydrophobic NPs, 8.3 ± 4.3 nm, was used to calculate the distribution SLP.

Several variables in the model had a degree of uncertainty. Sensitivity analysis on these variables was used find their approximate value, as well as their overall influence on heat transfer at various points within the system. The experimental model using the final values will be discussed with some comments on variable sensitivity, followed by a discussion of the sensitivity analysis.

The nanopainted tube shown in Fig. 20 was modeled using an axi-symmetric 2D modeling approach to maximize computational efficiency in the meshing and calculation process. Such is possible due to the geometry of the tube, and the assumption that the

nanopainted film is uniform at all points in the tube. In contrast to the dispersion heating model, the conduction equation was solved in cylindrical coordinates due to the geometry. The model geometry and variables used in selection of boundary conditions are shown in **Fig. 36**.

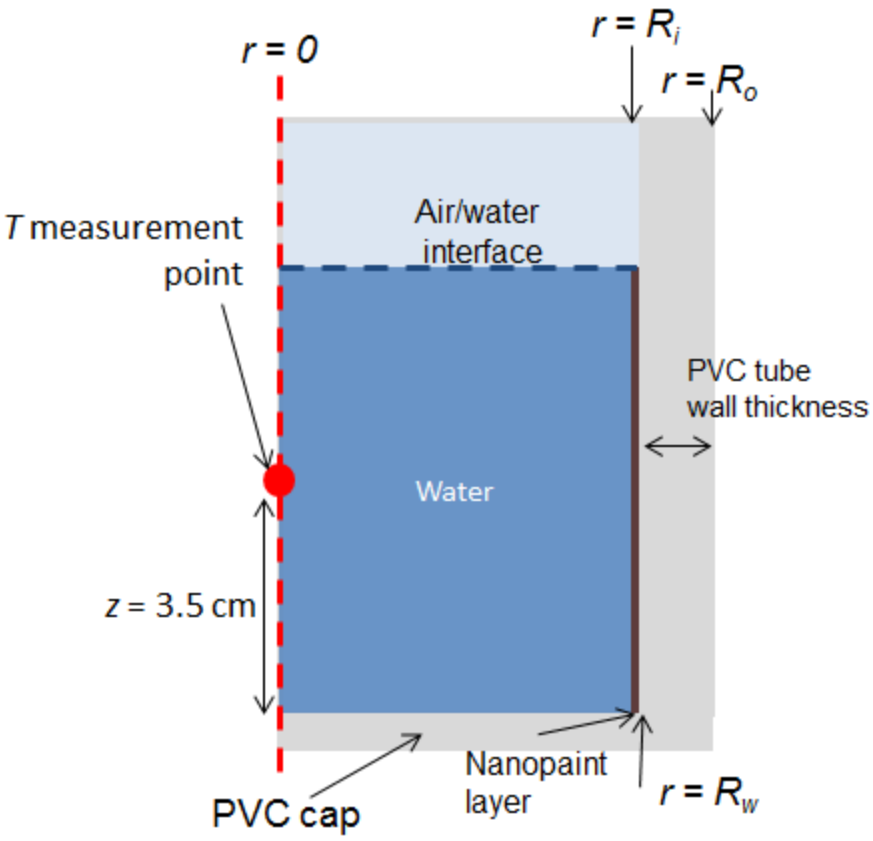

Figure 36–2D axial-symmetric illustration of the nanopainted tube geometry input into COMSOL for experimental modeling. The red dotted line represents the center of the nanopainted tube geometry (axially).

The model geometry was meshed in COMSOL using a triangular meshing scheme. A physics controlled meshing procedure was implemented so that a smaller mesh size

appears at smaller geometric features in the model. The final meshed geometry is shown in **Fig. 37**.

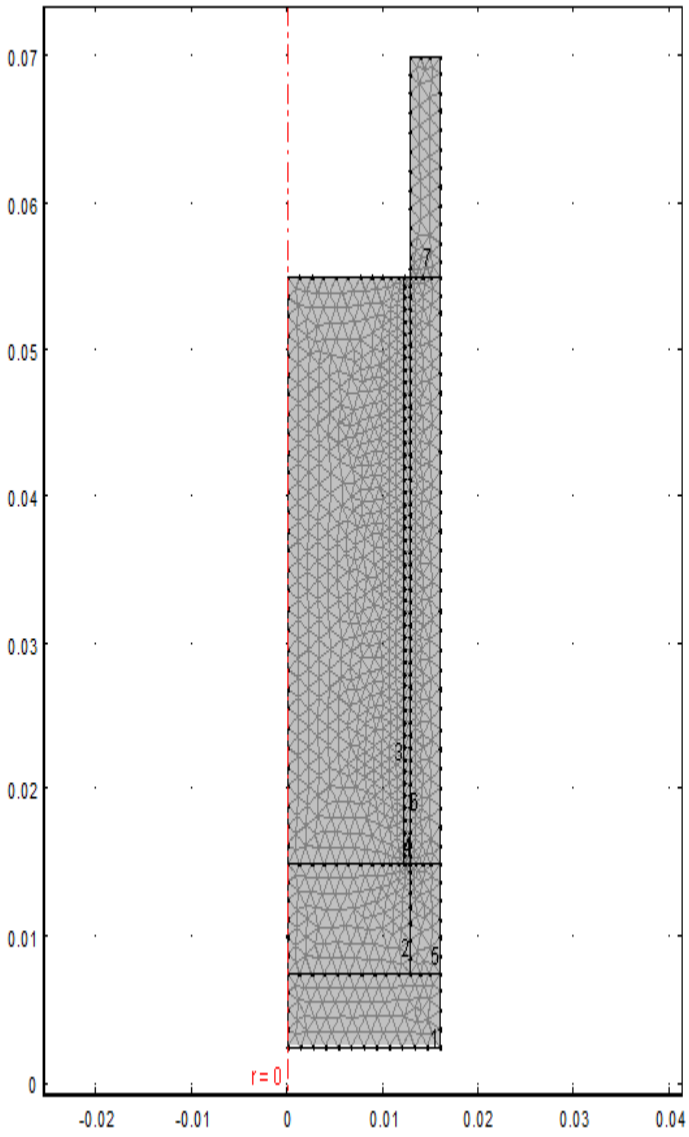

Figure 37–Meshed nanopainted tube geometry for the static fluid model.

The experiments were performed in an open air room with air circulation induced by the large fan in the induction heating power supply's water cooling unit. For this reason, a

convective cooling boundary condition was applied to the air/water interface between $r = 0$ and $r = R_i$, the upper surface of the tube between $r = R_i$ and $r = R_o$, and along the wall at $r = R_o$. The air/water interface at $0 < r < R_i$ has a temperature gradient with respect to r due to the heat source being at $R_i < r < R_w$. COMSOL accounts for this gradient by meshing along the boundary and calculating the temperature within each mesh cell for each iteration of the convective cooling boundary calculations. This boundary condition is mathematically represented at $r = R_o$ by Eq. (24).

$$q = h_a \left(T - T_a\right)\Big|_{r=R_o} \tag{24}$$

where h_a is the convective cooling coefficient of air, T_a was the air temperature in the room, and T was the temperature of the tube wall. Continuity of heat flux was assumed at the fluid/nanopaint surface ($r = R_i$) and at the nanopaint/tube wall interface ($r = R_w$). An example of this boundary condition is given at the water/nanopaint interface, R_i, via Eq. (25).

$$k_w \left(\frac{\partial T}{\partial r}\right)\Big|_{r=R_i} = k_{N\text{paint}} \left(\frac{\partial T}{\partial r}\right)\Big|_{r=R_i} \tag{25}$$

where k_w is the thermal conductivity of the water, and k_{Npaint} is the thermal conductivity of the nanopaint. The lower surface of the tube was capped and placed on a Styrofoam insulating cup, as shown in Fig. 20, so it was considered an insulated boundary by setting the heat flux equal to zero at this point. The thermal conductivity of the nanopaint was calculated using Maxwell's effective medium theory (Eq. (19) as 0.24 W m^{-1} K^{-1}.

Finally, a heat source value was assigned to the nanopaint using the volume fraction of NPs assumed in the paint, as well as the SLP value for 8.3 ± 4.3 nm particles. Sensitivity trials were performed to estimate the approximate weight percentage of NPs in the nanopaint. The original nanopaint mixture, prior to evaporation of the aromatic components, contained 20 wt% NPs; there was 30 wt% NPs following complete evaporation of the aromatics (assuming no aggregation of the NPs during nanopaint application to the tube). Twenty and thirty wt% were considered the lower and upper limits of NP concentration in the nanopaint in the sensitivity trials. There was also some uncertainty in the nanopaint thickness applied to the tube. Based on the number of paint coatings applied, the nanopaint thickness should have been ~400 – 600 μm based on manufacturer specifications. Sensitivity trials of the nanopaint thickness were performed in conjunction with the NP wt% sensitivity trials to estimate the heat source term, Q_p. The heat source term was calculated using Eq. (10) for a NP size distribution of 8.3 ± 4.3 nm and varying magnetic field strengths. The estimation of the magnetic field strength (H) input into Eq. (10) from Eqs. (1) – (3), as previously discussed, introduced another potential source of error. Via sensitivity trials, the wt% of NPs in the nanopaint and nanopaint thickness were adjusted to match observed experimental results. The wt% of NPs in the paint was estimated in this manner as ~30%, which corresponds to a volume fraction of 8.9%, and the nanopaint thickness was estimated as ~600 μm. The final parameters selected for the COMSOL model are displayed in **Table 12**.

Parameter	Abbrev.	Value	Unit
NP diameter	D_p	8.3 ± 4.3	nm
NP thermal conductivity	k_{NP}	9.7	W m^{-1} K^{-1}
weight %	wt%	30	-
volume %	vol%	8.9	-
Nanopaint density	ρ_{Npaint}	1536	kg m^{-3}
Nanopaint thermal conductivity	k_{paint}	0.24	W m^{-1} K^{-1}
Nanopaint specific heat capacity	$C_{p,paint}$	1086	J kg^{-1} K^{-1}
Air temperature	T_a	293	K
Convective heat transfer coeff. of air	h_a	80	W m^{-2} K^{-1}
frequency	f	430	kHz
Heat source, H = 4667 A m^{-1}	Q_p	$1.79 \cdot 10^7$	W m^{-3}
Heat source, H = 2778 A m^{-1}	Q_p	$6.36 \cdot 10^6$	W m^{-3}
Heat source, H = 1667 A m^{-1}	Q_p	$2.30 \cdot 10^6$	W m^{-3}

Table 12–Summary of parameters used for final nanopainted tube experimental model.

Tube radius	R_t	1.28	cm
Tube wall thickness	t_w	0.32	cm
Nanopaint thickness	t_N	600	μm
Nanopainted section length	L_N	4.5	cm
Tube length	L_t	6.75	cm
Water volume	V_w	25	mL
Tube (PVC) thermal conductivity	k_{tube}	0.15	W m^{-1} K^{-1}

Table 12–Summary of parameters used for final nanopainted tube experimental model cont.

The convective heat transfer coefficient of air, h_a, might seem large. The convective heat transfer coefficient of air is commonly reported in the range of 10 – 100 W m^{-2} K^{-1}; due to the potential for air currents in the room from the power supply cooling fan, a value of 80 W m^{-2} K^{-1}. This value was also selected by calibrating the temperature in the model at the outer tube wall to a qualitative touch estimate that was performed following experiments (to be explained).

The transient experimental models were analyzed for an experimental time period of 100 seconds, and the experimental data was truncated to the same time length. An example of the model temperatures following meshing and solving the differential equations for each element is shown in the temperature surface plot in **Fig. 38**.

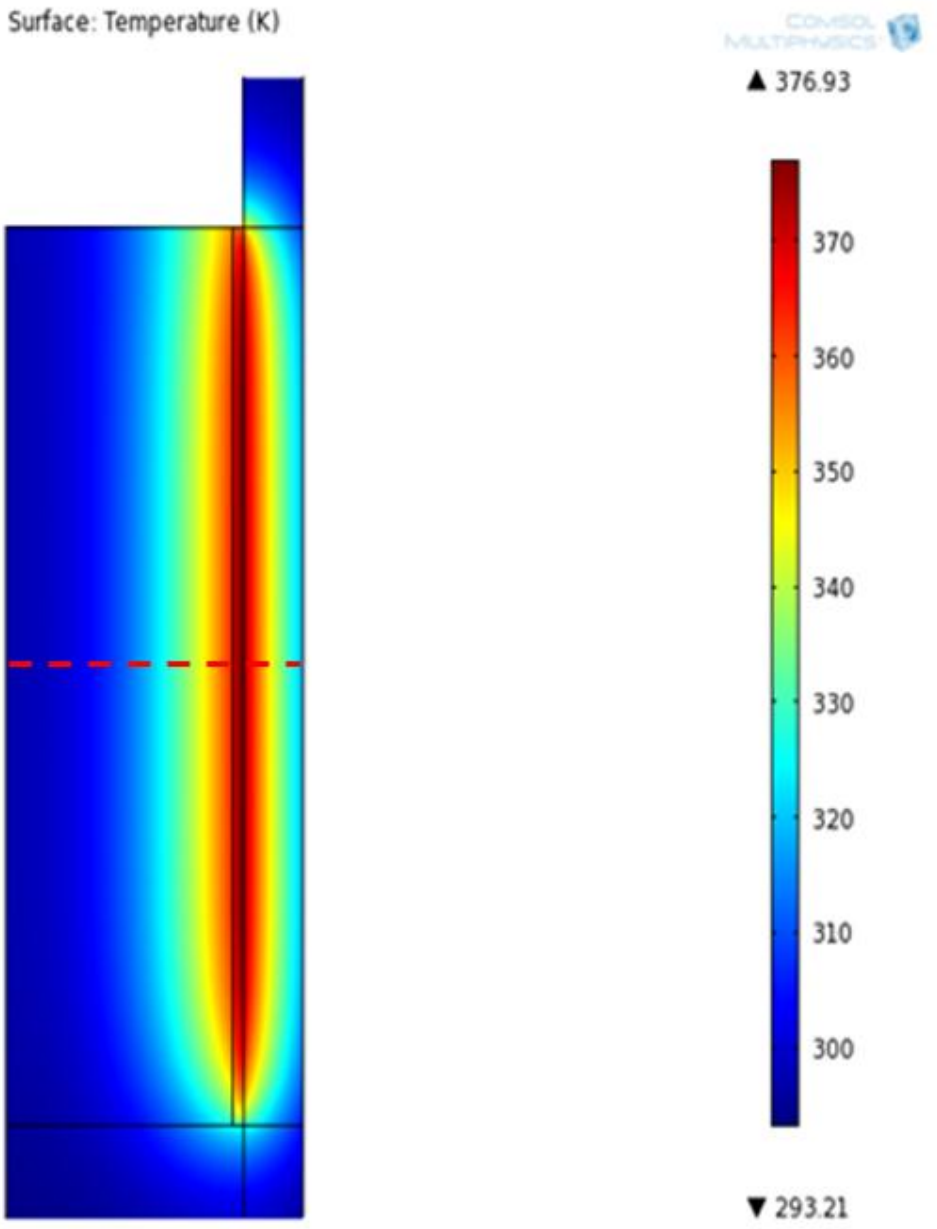

Figure 38–Temperature surface plot of solved nanopainted tube model for a nanopaint heat source value of $1.79 \cdot 10^{7}$ W m^{-3} (f = 430 kHz, H-field = 4667 A m^{-1}). The surface plot shown is at a time slice of 100 s. The dotted line represents the midpoint of the paint where radial temperature curves were generated (z = 3.5 cm from the bottom).

The surface plot shows that the highest temperatures occur within the nanopaint heat source. Some of the heat is transferred to the target fluid (water), while some is lost to the environment due to convection. An energy balance will be included in the discussion of modeling results to identify how efficient the heat transfer to the target fluid versus the tube wall and surrounding air is.

First, the transient heating curves as a function of radial position within the tube for varying magnetic field strength will be discussed. The heating curves were generated at a height at the midpoint of the nanopaint (z = 3.5 cm up from the tube cap). The transient radial heating curves overlain with experimental data for a magnetic field strength of 4667 A m^{-1} ($Q_p = 1.79 \cdot 10^7$ W m^{-3}) are shown in **Fig. 39**.

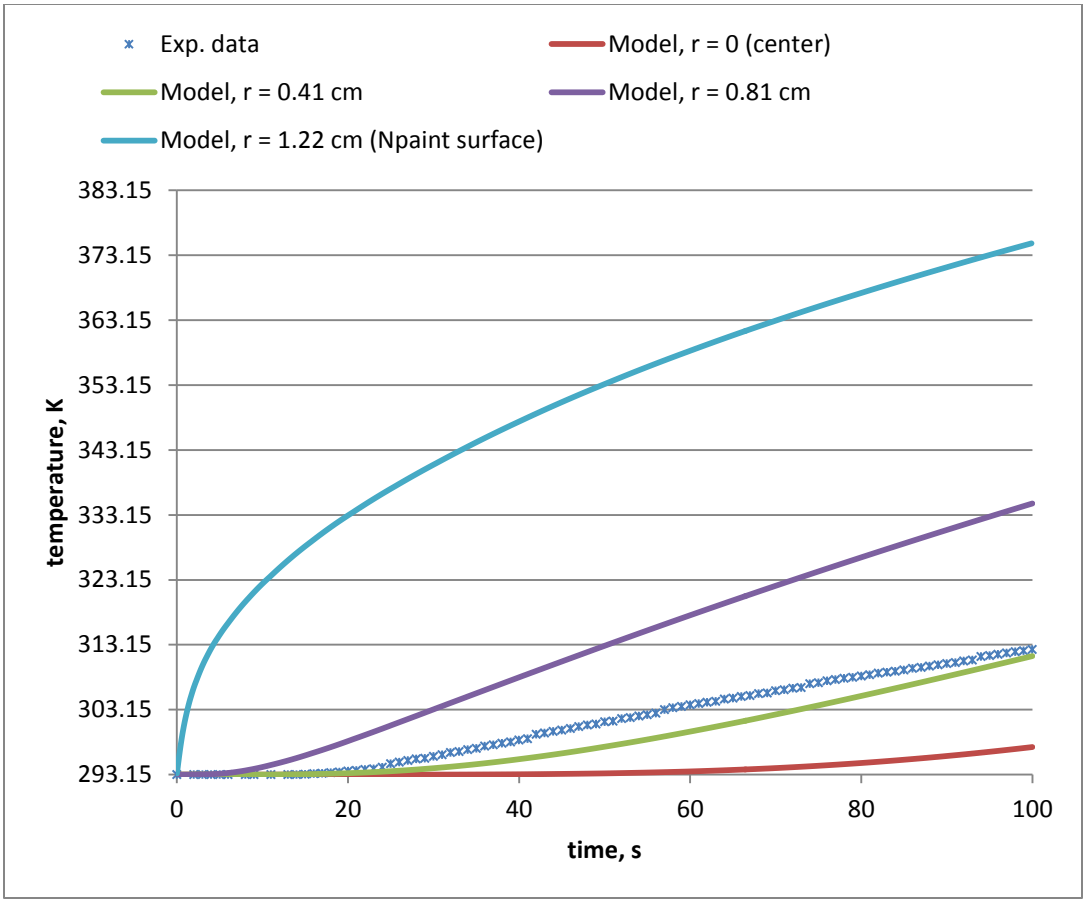

Figure 39–Transient heating curves overlain by experimental data at various radial positions within the nanopainted tube for a magnetic field strength of 4667 A m^{-1} (Q_p = $1.79 \cdot 10^7$ W m^{-3}).

The experimental data was taken at $0 < r < 1$ cm and $z = 3.5$ cm from the bottom of the tube (the approximate center of mass of the water). The uncertainty in the positioning was due to usage of a non-robust temperature anchor, which potentially moved slightly from experiment to experiment. Comparing the experimental data to the model indicates that the temperature at the center of the tube in the experiment increased slightly sooner than the $r = 0$ cm and $r = 0.41$ cm curves, but the heating rate was lower at later times than the model predicted. This could be due to particle magnetization lowering slightly as the nanopaint heated up, which was not accounted for in the purely heat transfer based

model. This possibility is indicated by the slight heating rate decrease starting at about 70 seconds. A lower particle magnetization results in lower magnetic susceptibility, which is the property that causes heat generation. Another important aspect of the model is that wall temperature at r = 1.22 cm; this is actually the temperature at the inner surface of the nanopaint. The model indicates that at 100 s, the wall temperature was ~383 °K, which is higher than the boiling point of water. Water in contact with the nanopaint surface would have been boiling, but this was not observed during the experiment. This is why the heat source term that was selected is considered the upper limit (based on maximum NP wt% in the nanopaint and largest mean NP size considered reasonable). Analysis of the lower field strength magnitude models later in this chapter will reveal why such large parameters were selected. **Figure 40** shows the full radial temperature profile at z = 3.5 cm all the way to the outer wall of the nanopainted tube at a time slice of 100 seconds.

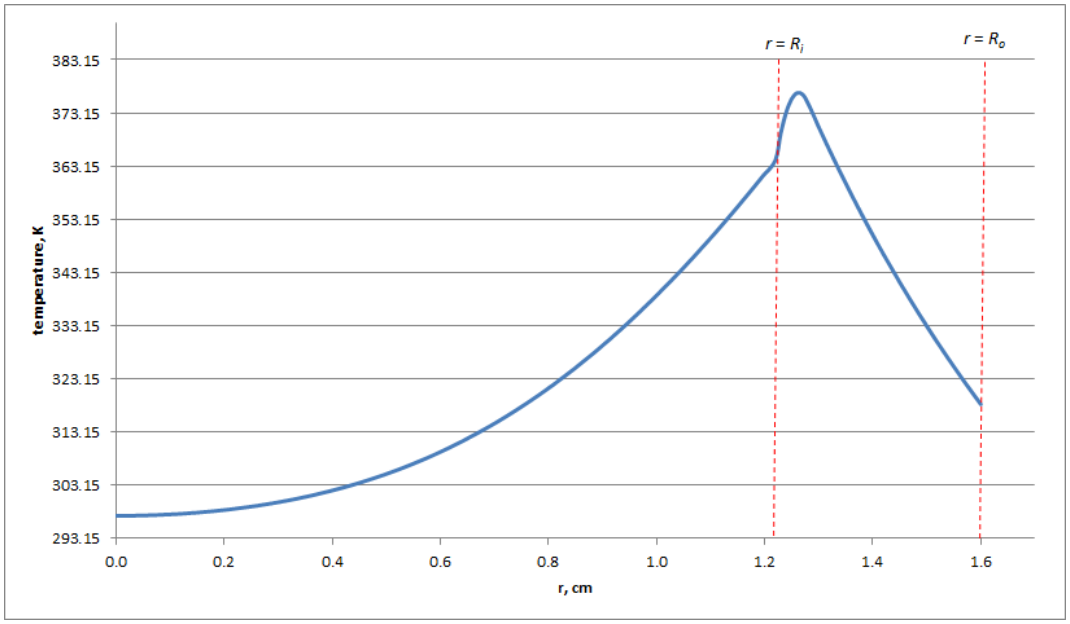

Figure 40–Radial temperature profile for nanopainted tube model at a height z = 3.5 cm, at a time of 100 seconds, and a magnetic field strength of 4667 A m^{-1}.

Figure 40 was used to calibrate the convective heat transfer coefficient at the outer surface of the tube nanopainted tube. General sources indicate that a temperature of ~315 K is too hot to touch. At the end of the experiment, the cylinder was too hot to handle, so it is assumed that it was around this temperature. A convective heat transfer coefficient of 80 W m^{-2} K^{-1} generated a temperature slightly higher than this in the model (~318 K), which is why it was deemed acceptable. Ideally, more advanced temperature sensors (pyrometer, IR camera) would have been used to measure the actual temperature, but none were readily available.

Next, the transient heating curves as a function of radial position for a magnetic field strength of 2778 A m^{-1} (Q_p = $6.36 \cdot 10^6$ W m^{-3}) were generated (**Fig. 41**); all other parameters were kept the same.

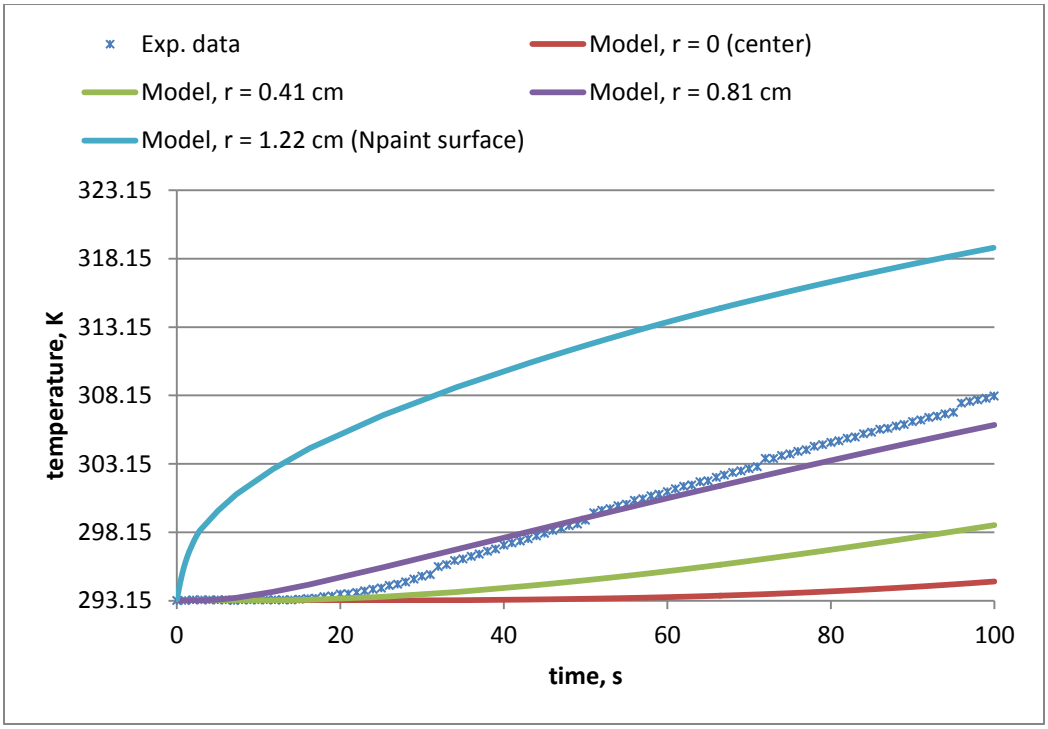

Figure 41–Predicted transient heating curves overlain by experimental data at various radial positions within the nanopainted tube for a magnetic field strength of 2778 A m^{-1} ($Q_p = 6.36 \cdot 10^6$ W m^{-3}).

Based on Fig. 41, the experimental data and model match at $r = 0$ until ~25 seconds. At this time, the experimental data indicates that the fluid at $r = 0$ absorbed more heat than predicted by the model; approximately as much as predicted by the model at $r = 0.81$ cm. The poor match between the model and experimental data led to the hypothesis that the nanoparticle heating was not actually proportional to the square of the magnetic field strength, H^2, as predicted by Eq. (10). Since the model heat generation term, Q_p was calculated using Eq. (10), an incorrect relationship in H would skew the model heating curves. At a frequency of 430 kHz, experimental hydrophobic NP dispersion heating results indicated a linear dependence in SAR on the magnetic field strength as shown in Fig. 14. The measured heating rate does not scale with H^2, however, it does show a strong

linear correlation. The experimental data for $r = 0$ in Fig. 39 approximately matched the r = 0.41 cm theoretical curve, which is thought to be within the uncertainty of the experimental temperature probe placement. Therefore, due to the strong experimental linear H dependence, the heat source term at 4667 A m^{-1} (Q_p = $1.79 \cdot 10^7$ W m^{-3}) was linearly scaled in H to determine if a better experimental to model match resulted for a magnetic field strength of 2778 A m^{-1}. This yielded a Q_p of $1.07 \cdot 10^7$ W m^{-3}. Equation (26) was used to linearly scale the heat source term in H.

$$Q_{p,new} = Q_{p,4667\,A/m} \frac{H_{new}}{4667} \tag{26}$$

The new Q_p term was input into the static nanopainted tube flow model; the new model data overlain by experimental data for 2778 A m^{-1} is shown in **Fig. 42**.

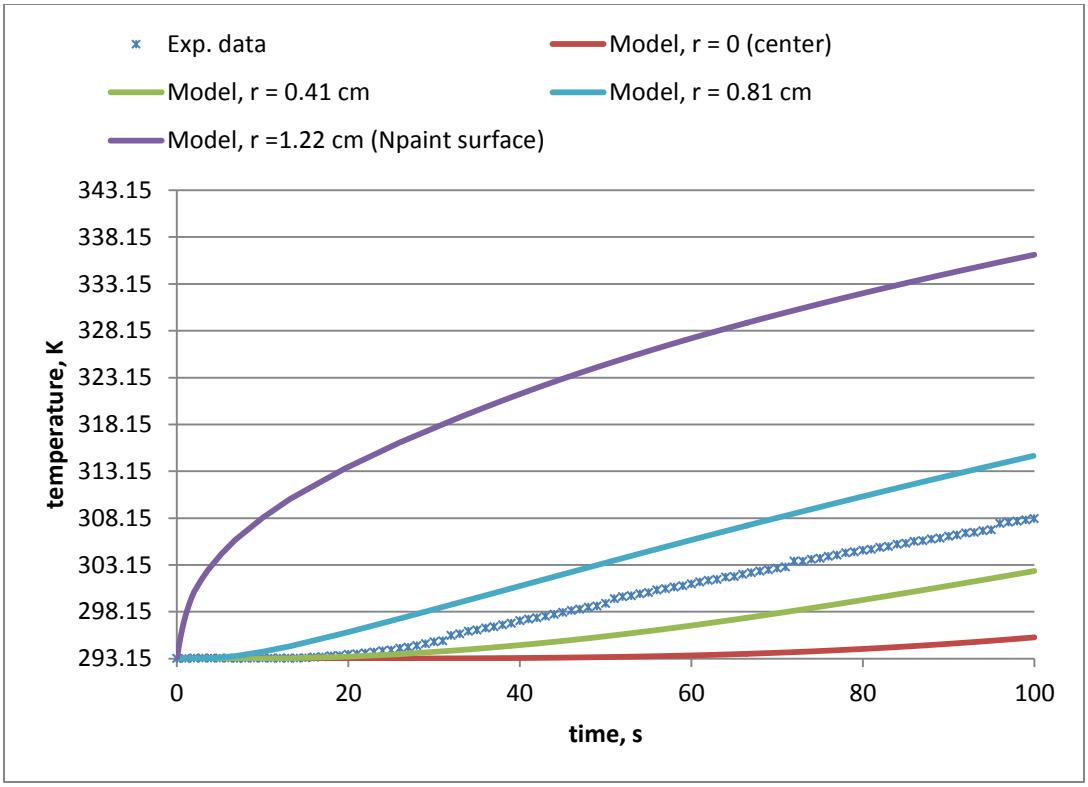

Figure 42–Predicted transient heating curves with Q_p linearly scaled in H ($Q_p = 1.07 \cdot 10^7$ W m^{-3}) overlain by experimental data at various radial positions within the nanopainted tube for a magnetic field strength of 2778 A m^{-1}.

The model data in Fig. 42 much more closely matches the experimental data than the model data in Fig. 41, however, a discrepancy still exists. It is assumed that the temperature probe remained stationary throughout the experiment, so another phenomenon caused improved heat transfer from the nanopaint to the center of the fluid, potentially convective over turn. Convective over turn occurs due to a density gradient in a fluid column. The radial temperature gradient in the static fluid nanopainted tube experiment would induce the fluid closer to the nanopaint surface (larger T) to tise, and the fluid at $r = 0$ (smaller T) to sink. Such a convection pattern would cause the circulation of fluid, which would increase heat transfer to the center of fluid. COMSOL

does not account for convective over turn, so it is a possible explanation for the larger experimental temperature at $r = 0$ relative to the model.

Last, the transient heating curves as a function of radial position for a magnetic field strength of 1667 A m^{-1} were generated for a $Q_p \sim H^2$ ($Q_p = 2.30 \cdot 10^6$ W m^{-3}) as well as $Q_p \sim H^1$ ($Q_p = 6.39 \cdot 10^6$ W m^{-3}) (**Fig. 43**). Again, the Q_p was linearly scaled in H using Eq. (26).

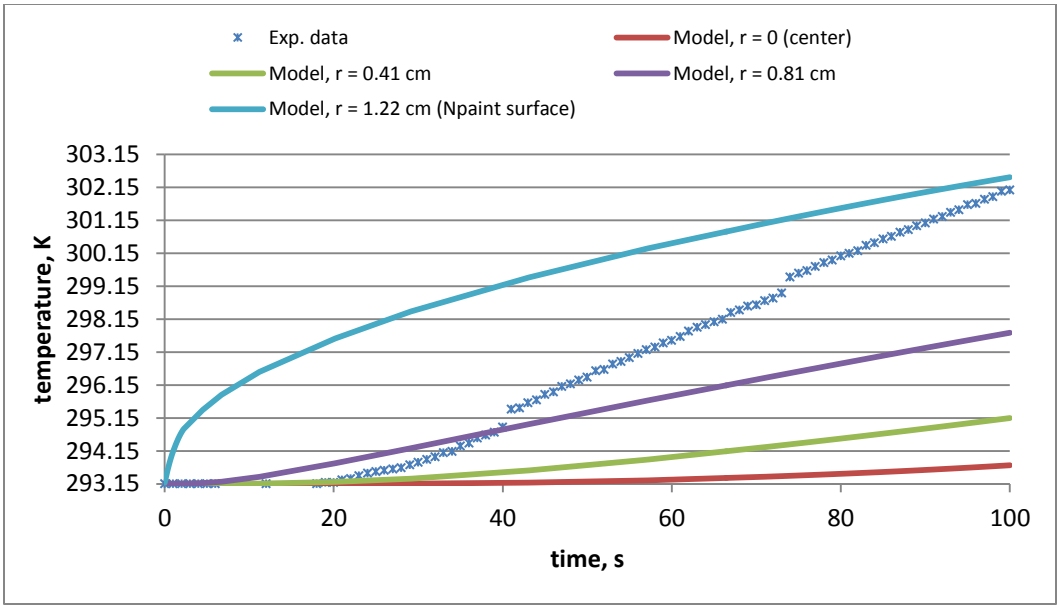

(a)

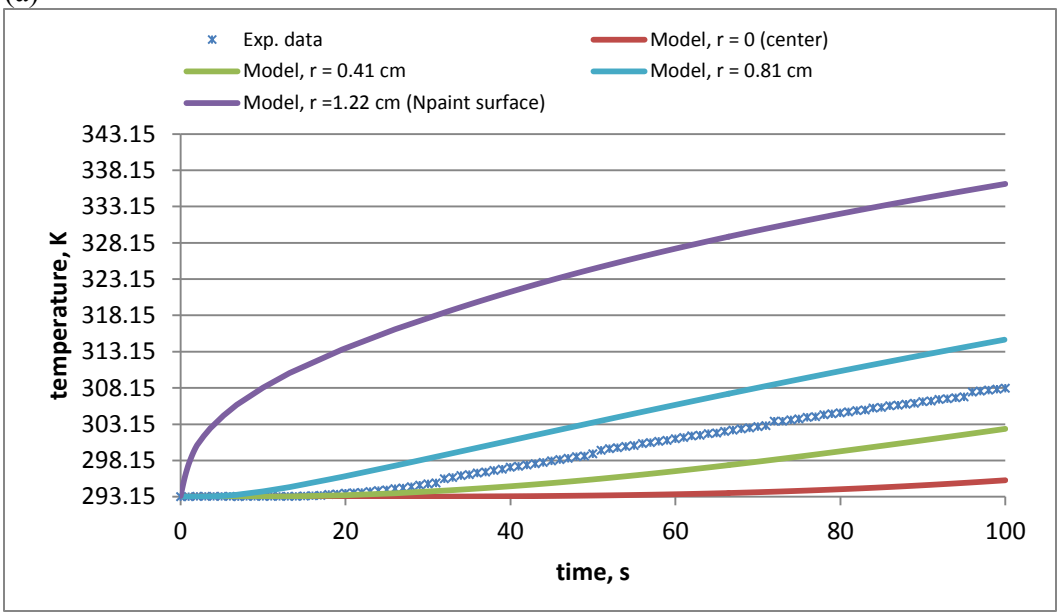

(b)

Figure 43–Transient heating curves overlain by experimental data at various radial positions within the nanopainted tube for a magnetic field strength of 1667 A m^{-1}. (a) $Q_p \sim H^2$, $Q_p = 2.30 \cdot 10^6$ W m^{-3}; (b) Q_p linearly scaled in H based on Eq. (26), $Q_p = 6.39 \cdot 10^6$ W m^{-3}.

Inspection of Fig. 43(a) shows an even more extreme difference between measured and predicted heating rate of the water at the center. Figure 40(b) shows a much better match. The improved match between the model and experimental data using linear H scaling suggests that the hydrophobic NPs likely have a linear H-field dependence on heat generation rather than a square dependence.

Once again, the initial experimental temperature response matches the experimental model curve at the center of the tube, but deviates at ~23 seconds due to an increased heating rate. Based on the constraints of the system (Q_p, k_w), this is an indicator that convective over turn again took place as the experiment progressed. Increasing the model Q_p value even more (by increasing the NP wt% in the nanopaint) would shift the curves upward, but doing so would shift the 4667 A m^{-1} experimental model beyond physical limits due to the nanopaint wall surface becoming too hot.

Several of the key uncertain variables have already been discussed with respect to sensitivity. In all, the variables considered uncertain were the nanoparticle wt% in the nanopaint, the nanopaint thickness, the convective heat transfer coefficient of air, radial positioning of the temperature probe, and the thermal conductivity of the nanopaint. The nanoparticle wt% in the paint was the percentage expected when experimentally prepared, which indicates that the aromatic components were able to adequately disperse them during the mixing process and then evaporate while curing. Increasing or decreasing the nanopaint thickness essentially changes the amount of heat introduced to the system since Q_p is an intensive property, thus it is equivalent to leaving the nanopaint thickness the same and increase/decreasing the value of Q_p. Adjusting the thermal conductivity of the paint has no impact on the heat transfer properties of the system, so it would be wasteful to invest in a thermally conductive resin for scale up experiments or

pilot tests. The sensitivity of the convective heat transfer coefficient has already been discussed in full.

Additionally, energy balances were performed by integrating the enthalpy of all of the COMSOL model domains. The energy balances for magnetic field strengths of 1667 A m^{-1}, 2778 A m^{-1}, and 4667 A m^{-1} are given in **Tables 13**, **14**, and **15**, respectively. The energy balances for the magnetic field strengths of 1667 A m^{-1} and 2778 A m^{-1} are from the models with a heat source term linearly scaled in *H*.

Domain	Heat (J)	% of Source
Paint Source	1205	
Water	836	69.4
Tube	214	17.8
Surroundings	155	12.9

Table 13: Static fluid, nanopainted tube energy balance for a magnetic field strength of 1667 A m^{-1} after 100 seconds based on experimental COMSOL model.

Domain	Heat (J)	% of Source
Paint Source	2008	
Water	1397	69.6
Tube	358	17.8
Surroundings	253	12.6

Table 14: Static fluid, nanopainted tube energy balance for a magnetic field strength of 2778 A m^{-1} after 100 seconds based on experimental COMSOL model.

Domain	Heat (J)	% of Source
Paint Source	4538	-
Water	3372	74.3
Tube	623.0	13.7
Surroundings	543.3	12.0

Table 15: Static fluid, nanopainted tube energy balance for a magnetic field strength of 4667 A m^{-1} after 100 seconds based on experimental COMSOL model.

To evaluate the accuracy of the energy balances, limiting case energy balances were also analytically calculated and applied to the simulation results assuming the water in the static nanopainted tube was well mixed. The well-mixed assumption will help indicate if convective over turn was likely taking place or not. The first energy balance was calculated assuming that all of the heat from the nanopaint source was transferred to the water. The second energy balance was calculated assuming convection equivalent to that in the model took place (so all of the heat was not transferred to the water). Comparison of these two calculations also reveals how dominant convective heat transfer in the system is, and how it influences the resulting water temperature. A standard enthalpy equation was used to determine what the "well mixed" temperature of the water would be based on the amount of heat transferred to it (Eq. (27)).

$$Q_f = m_f C_p \Delta T_f \tag{27}$$

where $Q_f = Q_p \cdot V_f \cdot t$ [J] and m_f is the mass of water in the tube [g]. **Tables 16** and **17** summarize the results of the change in water temperature for the "well mixed" fluid calculations.

***H*-field, A m^{-1}**	**Energy to fluid (insulated), J**	**Well-mixed ΔT, K**	**Exp. ΔT at $r = 0$, $z = 3.5$ cm, K**
1667	1205	12	9
2778	2008	19	15
4667	4538	43	20

Table 16–Well-mixed fluid temperature for an insulated, no convection system in which all of the heat generated by the nanopaint is transferred to the fluid. The experimental temperature shown is at a time of 100 seconds.

***H*-field, A m^{-1}**	**Energy to fluid (convection), J**	**Well-mixed ΔT, K**	**Exp. ΔT at $r = 0$, $z = 3.5$ cm, K**
1667	836	8	9
2778	1397	13	15
4667	3372	32	20

Table 17–Well-mixed fluid temperature for a system with convection characteristics as described by the COMSOL nanopainted tube model. The experimental temperature shown is at a time of 100 seconds.

To analyze these results, the expected behavior should be described. In the case of a well-mixed system, the ΔT should be higher than that at the experimental measurement point documented. The fluid layers closer to the nanopaint surface contain more heat, so

mixing all of the fluid in the tube would result in a fluid temperature greater than that at the center point, $r = 0$. For the case in which all of the heat generated by the nanopaint is transferred to the water, shown in Table 16, the well-mixed ΔT is greater than the experimental ΔT for all magnetic field strengths. For the case in which convection to the air on exterior surfaces was considered (h_a = 80 W m^{-2} K^{-1}), the well-mixed temperature is actually lower than the experimental temperature at r = 0 at magnetic field strengths of 1667 A m^{-1} and 2778 A m^{-1}. This result is in disagreement with the expected behavior. A likely explanation for this is that the convective heat transfer coefficient selected was actually too large.

Collectively, the energy balances in Tables 13, 14, and 15 show that from a theoretical heat transfer standpoint, the conductive properties of the system do not change as the magnetic field strength changes. They also show that the target fluid, the water, in all cases absorbs most of the energy even though the convective heat transfer coefficient applied is relatively high. This can likely be attributed to the high thermal conductivity and specific heat capacity of water. Inspection of the well-mixed case with convection also shows that more heat than predicted by the COMSOL model was likely transferred to the target fluid (since the well-mixed ΔT's were lower than the experimental ΔT's at two of the magnetic field strengths), so the likely absorbed closer to 80% of the heat generated by the nanopaint.

5.3 FLOWING FLUID HEATING VIA NANOPAINTED TUBE MODEL

A 2D axial-symmetric COMSOL model was also generated to simulate the experimental heating of a flowing fluid through the nanopainted tube presented in the experimental section of this paper. The same nanopainted tube was used for the static fluid heating experiments as for the flowing fluid experiments, so little additional matching of uncertain variables was necessary. The physics of the model are also similar to the static fluid model with respect to heat transfer; however, it was necessary to add a momentum transfer component to the model to represent the flowing fluid. The static fluid model was transient with respect to time, but the flowing fluid model is stationary since the fluid reached a steady state flow rate during each experiment. Similar to the static fluid model, the flowing fluid model the magnetic heating response of the nanopaint is represented through a heat source term, which was calculated based on the SLP of the hydrophobic nanoparticles at each magnetic field strength.

All of the flow rates experimentally tested were in the laminar flow regime, so the representative laminar flow equation was used by COMSOL to solve for the radial velocity profile down the tube.

$$u_r = \frac{\Delta P}{4\mu L}\left(1-\left(\frac{r}{R}\right)^2\right) \tag{28}$$

where ΔP is the pressure drop from the inlet to the outlet of the tube (or across a finite element), μ is the viscosity of the tube fluid (in this case, water), L is the total length of the tube or finite element, and R is the radius of the tube. COMSOL also uses the standard equation of mass continuity (Eq. (29)) to balance each finite element.

$$\nabla \cdot (\rho u) = 0 \tag{29}$$

Lastly, the steady state version of Eq. (17) is used by COMSOL to calculate the overall energy balance within the flow system.

$$\rho C_p u \cdot \nabla T = \nabla \cdot (k \nabla T) + Q \tag{30}$$

Equation (30) was used to calculate the energy balances within the solid and liquid components of the system, so the variables represent the properties within each respective domain. **Figure 44** is an illustration of the flow system including and immediately surrounding the nanopainted tube.

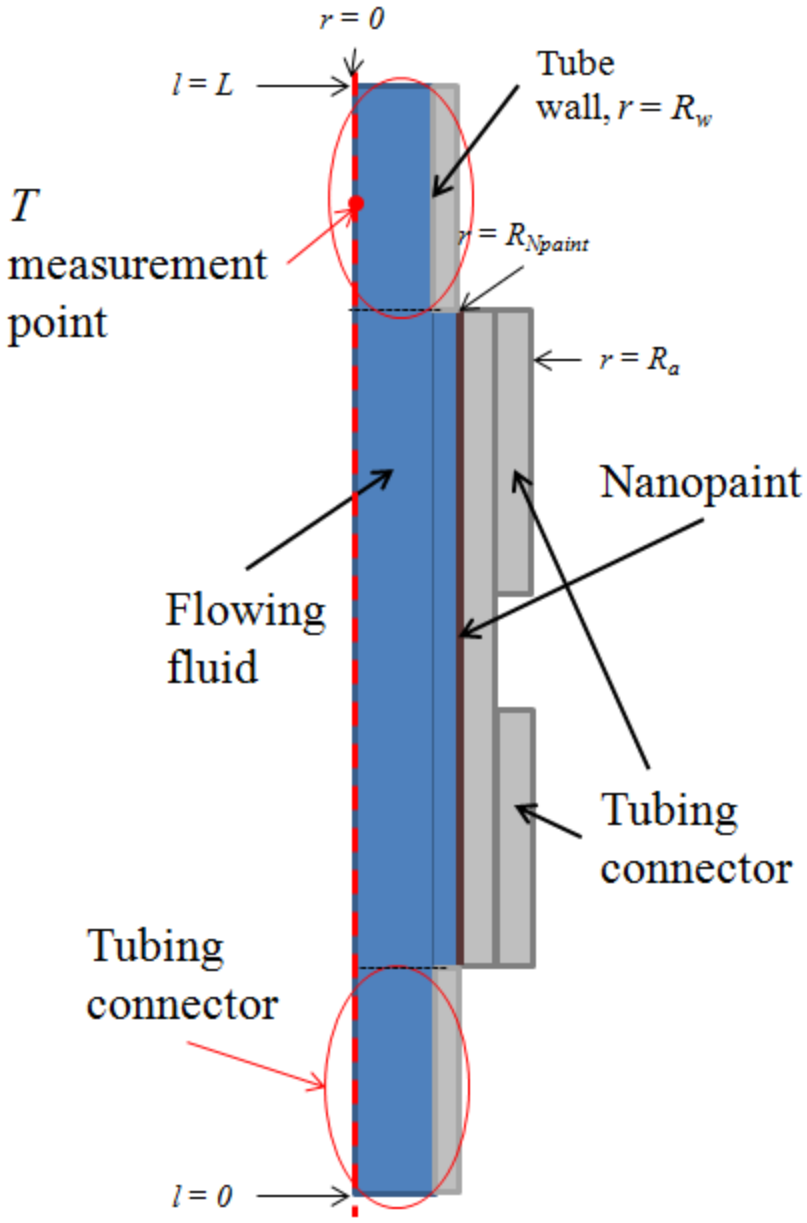

Figure 44–Illustration of the nanopainted tube and the tubing sections/connectors immediately surrounding it. There was an expansion entering the painted tube section, and a contraction of the flow pathway leaving it, which was represented by the circled sections in the model illustration.

The geometry shown in Fig. 44 was meshed using the same physics controlled procedure described for the static fluid nanopainted tube model. The meshed grid appears smaller

for the flowing fluid model because the system is longer and contains some finer geometric elements. The meshed COMSOL geometric model is shown in **Fig. 45**.

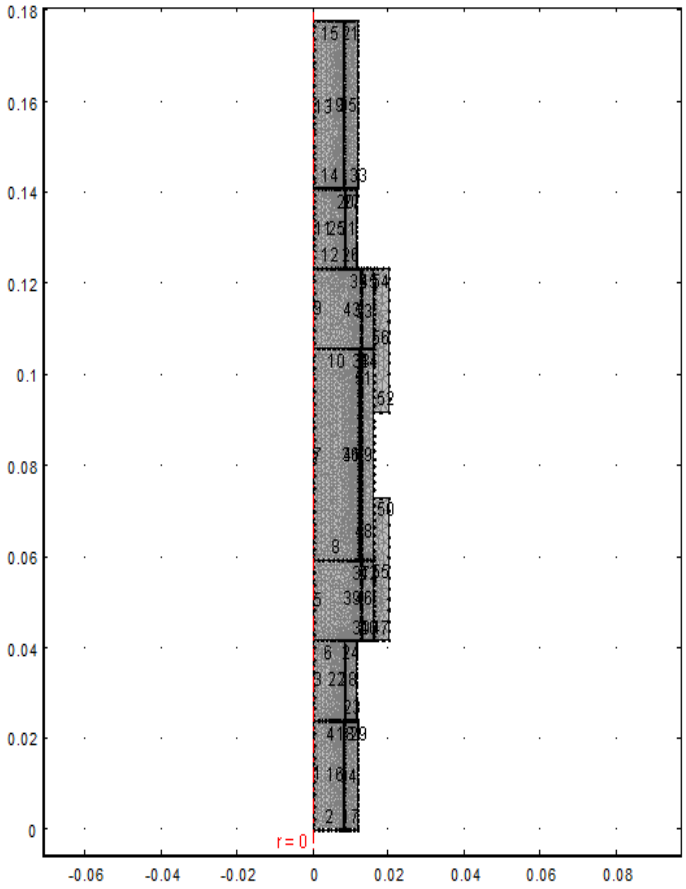

Figure 45–Meshed nanopainted tube geometry for the flowing fluid model.

The boundary conditions for the flowing system were very similar to those used for the static fluid model. Newton's law of cooling, represented in Eq. (24), was applied to all of the exterior tubing surfaces with h_a = 80 W m^{-2} K^{-1}. Continuity of flux was applied to the interior surfaces (at $r = R_{N\text{paint}}$ for example) using a relationship similar to Eq. (25), depending on the domain material. A symmetry boundary was applied at r = 0

due to the axial-symmetric nature of the model. A laminar flow inlet was applied at $l = 0$. The flow rate at this point was set according to the steady state flow rate recorded during the modeled experiments. The flow was set to achieve laminar flow 1 m upstream of the inlet (entrance length). Such a long entrance length may not have been most representative of the experimental conditions, which will be discussed. A no viscous stress boundary condition was set at the flow outlet ($l = L$). While not included in the model, both ends of the real experimental system were open to the atmosphere, so a significant pressure drop would not have occurred within the system. The system parameters input into the model are very similar to those from the static fluid model with a few minor changes; these are summarized in **Table 18**.

Parameter	Abbrev.	Value	Unit
NP diameter	D_p	8.3 ± 4.3	nm
weight %	wt%	30	-
volume %	vol%	8.9	-
Nanopaint density	ρ_{Npaint}	1536	kg m^{-3}
Nanopaint thermal conductivity	k_{paint}	0.24	W m^{-1} K^{-1}
Nanopaint specific heat capacity	$C_{p,paint}$	1086	J kg^{-1} K^{-1}
Air temperature	T_a	293	K
Convective heat transfer coeff. Of air	h_a	80	W m^{-2} K^{-1}
frequency	f	430	kHz
Heat source, H = 4667 A m^{-1}	Q_p	$1.79 \cdot 10^7$	W m^{-3}
Heat source, H = 2778 A m^{-1}	Q_p	$1.07 \cdot 10^7$	W m^{-3}
Heat source, H = 1667 A m^{-1}	Q_p	$6.39 \cdot 10^6$	W m^{-3}
Painted tube radius	R_t	1.28	cm

Table 18–Summary of parameters used for flowing fluid nanopainted tube model.

Tube radius at *T* measurement point	R_m	0.82	cm
Tube wall thickness	t_w	0.32	cm
Nanopaint thickness	t_N	600	μm
Nanopainted section length	L_N	4.5	cm
Modeled tubing length	L_t	17.8	cm

Table 18–Summary of parameters used for flowing fluid nanopainted tube model cont.

Some of the experimental flow rates within the range shown in Table 8 were modeled to determine the validity of the experimental conclusions.

An example of a temperature surface plot and velocity profile is shown in **Fig. 46** for a flow rate of 5 mL/s and a magnetic field strength of 4667 A m^{-1} ($Q_p = 1.79 \cdot 10^7$ W m^{-3}).

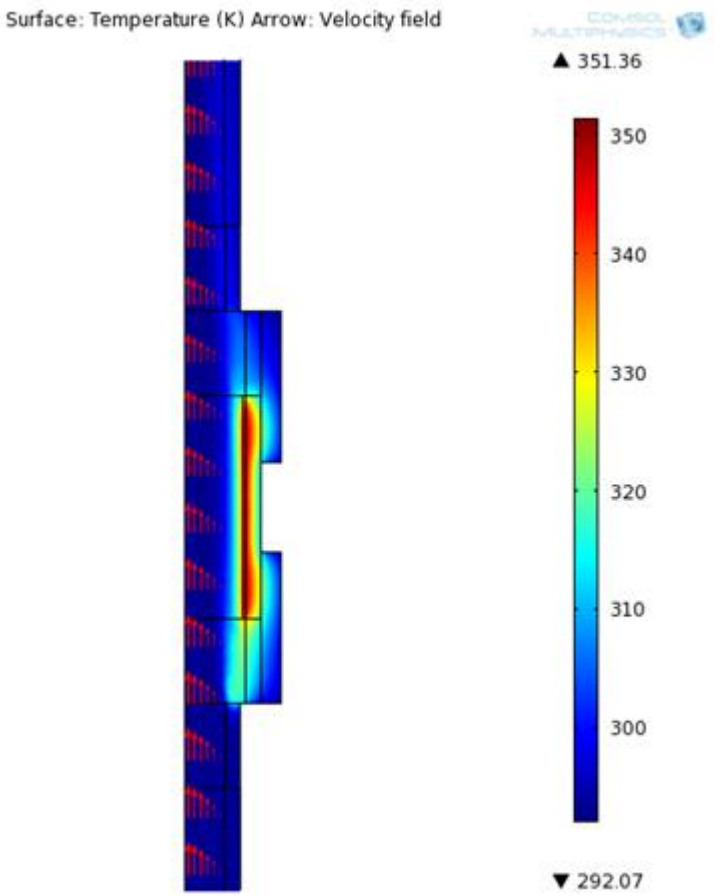

Figure 46–Surface temperature plot overlaid with the fluid flow velocity (arrows) for the nanopainted tube model at a flow rate of 5 mL s^{-1} and a magnetic field strength of 4667 A m^{-1}.

The surface plot shows that while some significant heat was transferred to the fluid layers immediate in position to the nanopaint, the laminar flow regime prevents substantial mixing and further transfer of the heat to interior fluid layers. The highest temperatures once again occurred within the nanopaint layer, but they did not achieve the same magnitude as in the static fluid model (~377 °K). This can be attributed to the flowing

fluid removing more heat from the nanopaint surface due to a more favorable temperature gradient for heat transfer in the non-static fluid case.

A radial temperature profile at the experimental temperature measurement point indicated in Fig. 44 was first plotted against the experimental data at a magnetic field strength of 4667 A m^{-1} and a flow rate of 5 mL s^{-1} (**Fig. 47**).

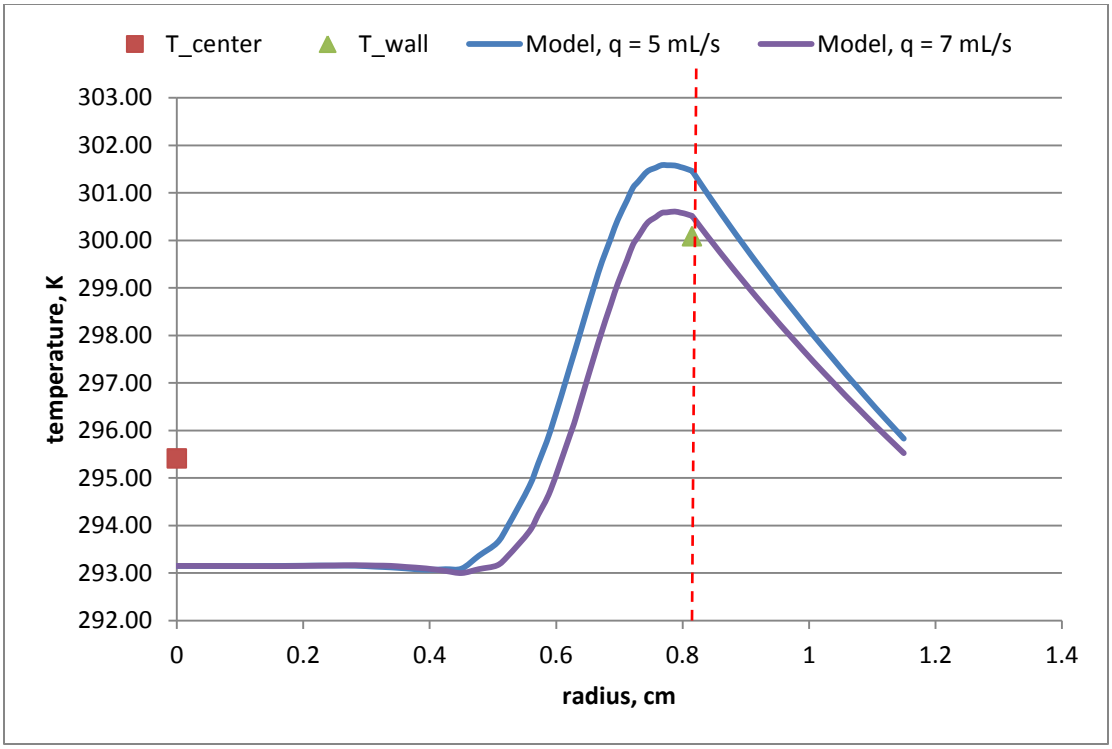

Figure 47–Flowing fluid model radial temperature profile plotted against experimentally measured temperatures at the center of the flow pathway (T_center; 5 mL s^{-1}) and at the tube wall (T_wall; 7 mL s^{-1}) for a magnetic field strength of 4667 A m^{-1} and a flow rate of 5 mL s^{-1}. The model temperatures represent those at the approximate position where experimental temperatures were recorded, R_m (15.4 cm downstream of the model inlet). The red dotted line indicates the position of the tube wall in the model.

One discrepancy between the model and experimental temperatures that stands out is the temperature difference at the center of the flow pathway. Experimentally, a steady state

temperature increase of ~2.5 °K was measured at the center of the flow pathway; however, the model predicts that for a laminar flow regime, no temperature change at the center of the flow pathway should have occurred. The flow model yielded a closer temperature match at the nanopaint surface where only a 0.5 °K discrepancy between the model and experimentally recorded temperature resulted. The model depicts that a small change in flow rate (2 mL/s) produces a notable difference in the fluid temperature at the wall (r ~ 0.81 cm; ~1 °K) relative to the total temperature change (~7.5 °K). Results for the flowing fluid were also generated for flow rates of 10 mL/s and 12 mL/s at magnetic field strength of 4667 A m^{-1} (**Fig. 48**).

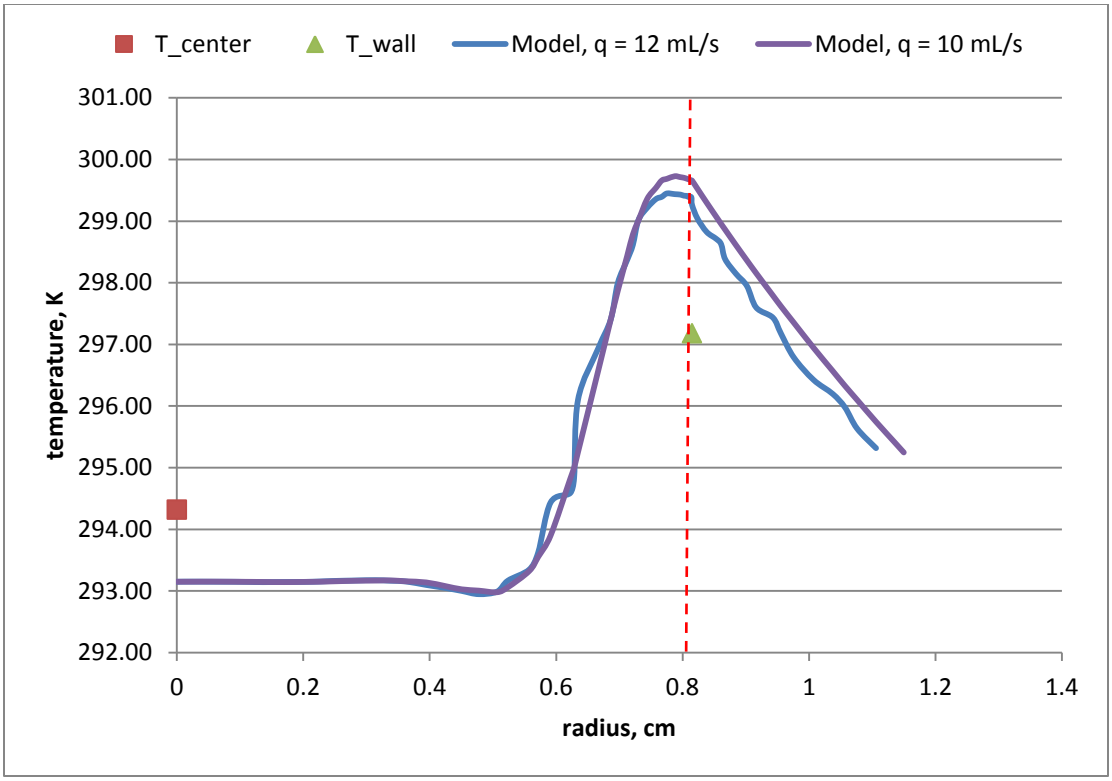

Figure 48–Flowing fluid model radial temperature profile plotted against experimentally measured temperatures at the center of the flow pathway (T_center; 12 mL s^{-1}) and at the tube wall (T_wall; 10 mL s^{-1}) for a magnetic field strength of 4667 A m^{-1} and flow rates of 12 and 10 mL s^{-1}. The red dotted line indicates the position of the tube wall in the model.

Comparison of T_wall in Fig. 47 to Fig. 48 shows that the experimental temperature response at the wall is much more sensitive to the flow rate than the model predicts. A significant decrease in ΔT at the wall (~3 °K) occurred experimentally relative to the model predciction (~1 °K) when the flow rate was approximately doubled. As expected, at higher flow rates, the model is unable to account for the fluid temperature increase at the center of the flow rate; this is expected relative to lower flow rates since the residence time of the fluid in contact with the nanopaint is lower at higher flow rates. The model fluid temperature at the tube wall is also less sensitive to flow rate than at lower flow rates (compare Fig. 47 to Fig. 48).

The model indicates a lack of temperature response at the center of the flow pathway combined with an increased sensitivity in temperature response towards the wall indicates one possible scenario–some aspects of a turbulent flow regime were actually occurring during the experiments. Mixing is the primary process that could have experimentally occurred that would cause an experimental increased temperature response at the center of the flow pathway by redistributing some of the heat at the nanopaint surface (causing a reduced temperature at the surface). Mixing could have been caused by two design constraints inherent to the apparatus that aren't sufficiently accounted for in the model: (1) laminar flow had not completely developed prior to entering the painted section of the piping system due to a relatively short distance from the pumping tank (rapid contraction into the tubing) to the painted section inlet (~2 ft.); (2) the tubing connector at $l = 0$ in Fig. 41 was immediately preceded by a 60° elbow. COMSOL did not indicate heavy mixing within the painted section due to the contraction/expansion and expansion/contraction of the tubing connectors surrounding the painted section (Fig. 41), so it isn't thought that this was a key contributor to the mixing.

The model was also run to simulate experimental trials where magnetic field strengths of 2778 A m^{-1} ($Q_p = 1.065 \times 10^7$) and 1667 A m^{-1} ($Q_p = 6.39 \times 10^6$) were applied to the system. The Q_p values indicated represent the linearly scaled values calculated and discussed from the static fluid nanopainted tube model. The simulation at a magnetic field strength of 2778 A m^{-1} and a flow rate of 3 mL s^{-1} is shown in **Fig. 49**.

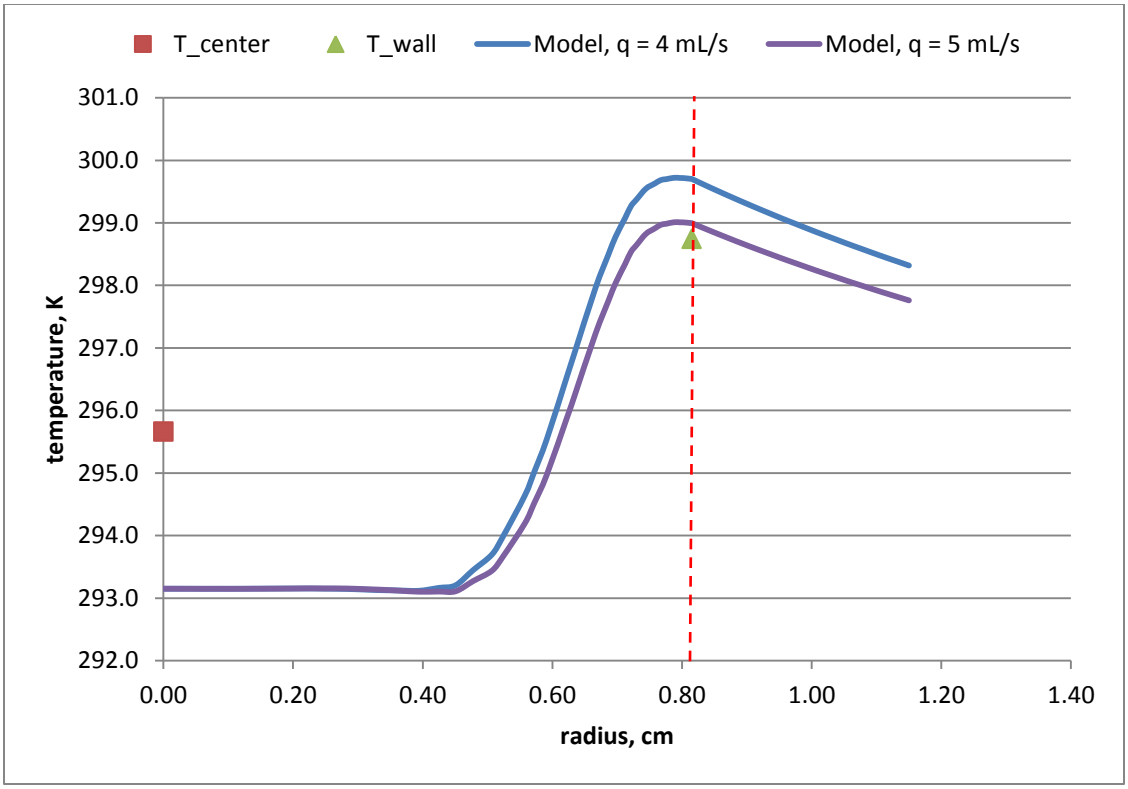

Figure 49–Flowing fluid model radial temperature profile plotted against experimentally measured temperatures at the center of the flow pathway (*T_center*; 4 mL s^{-1}) and at tube wall (*T_wall*; 5 mL s^{-1}) for a magnetic field strength of 2778 A m^{-1} and a flow rates of 4 and 5 mL s^{-1}. The red dotted line indicates the position of the tube wall in the model.

Experimentally, Fig. 49 shows that the temperature profile from the center to the wall looks similar to the profiles at 4667 A m^{-1}. Comparison of the model to the experimental data indicates that the scaled model closely predicts the fluid temperature at the tube wall (within ~1 °K), but again, cannot account for the temperature change at the center of the flow pathway. If the scaled Q_p value had not been used, the model would have greatly under predicted the temperature at the wall.

The simulation at a magnetic field strength of 1667 A m^{-1} and a flow rate of 3 mL s^{-1} is shown in **Fig. 50**.

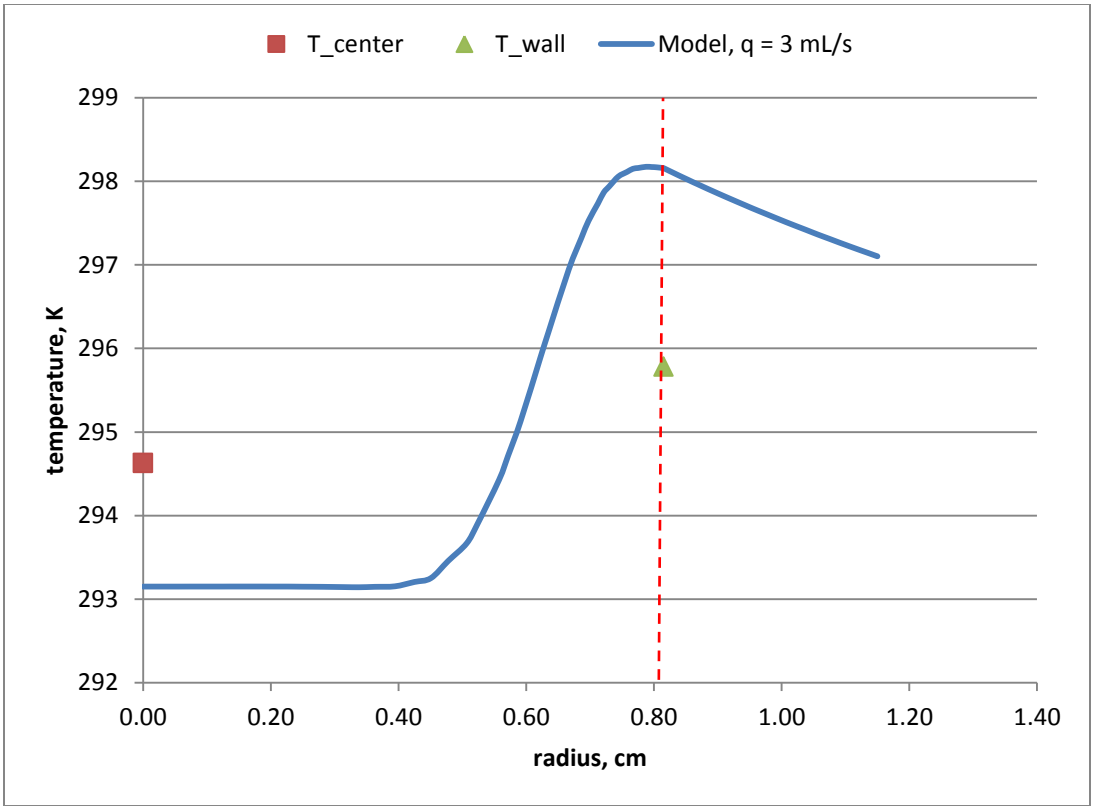

Figure 50–Flowing fluid model radial temperature profile plotted against experimentally measured temperatures at the center of the flow pathway (*T_center*; 3 mL s^{-1}) and at tube wall (*T_wall*; 3 mL s^{-1}) for a magnetic field strength of 2778 A m^{-1} and a flow rate of 3 mL s^{-1}. The red dotted line indicates the position of the tube wall in the model.

Comparison of the experimental data and simulated model in Fig. 50 shows that while the model maintains a similar temperature profile to the other magnetic field strengths, the experimental temperatures approach a temperature profile representative of turbulent flow. The variation in fluid temperature between the center of the flow pathway and the tube wall decreased compared to the higher magnetic field strengths, which supports the occurrence of mixing even more.

As a baseline, to indicate if mixing was a possibility, the model radial temperature curves integrated to find the cup-average mixing temperature. If mixing were occurring, then the cup-average mixing temperature should fall between *T_center* and *T_wall*. The

model temperature curves should give an approximate estimate of the cup-average mixing temperature since heat source term appeared approximately accurate from the static fluid nanopainted tube models after making the Q_p scaling adjustment. Some inaccuracy may exist from using a convective heat transfer coefficient that is larger than could be accounted for in the static fluid energy balances. The cup-average mixing temperature was calculated for one of the flow rates at each magnetic field strength by integrating the respective curve (Eq. (31)).

$$\overline{T} = \frac{\int_0^r V(r) 2\pi r T(r) dr}{\int_0^r V(r) 2\pi r dr} \tag{31}$$

Table 19 summarizes the results of the cup-average mixing temperature calculations for the nanopainted tube flowing fluid model. The experimental temperatures with a flow rate documented in parentheses were recorded at that flow rate rather than the model flow rate for which the cup-average mixing temperature was calculated; the slight discrepancy in flow rate of 1 - 2 mL/s should not have a significant impact for the baseline comparison.

H-field, A/m	Flow rate, mL/s	Cup-avg. mixing T, K	Exp. T_center, K	Exp. T_wall, K
1667	3	296.3	294.6	295.8
2778	5	296.7	295.7	298.7 (4 mL/s)
4667	5	298.4	295.6 (7 mL/s)	300.1

Table 19–Resulting cup-average mixing temperatures calculated from the flowing fluid nanopainted tube model radial temperature curves.

In all cases but the 1667 A m^{-1} case, the calculated cup-average mixing temperature fell between the experimental centerline and wall temperatures, which supports that mixing potentially took place. In the 2778 and 4667 A m^{-1}, the calculated average mixing temperature fall nearly in the middle of the center and wall temperatures. In the case of the lowest magnetic field strength, 1667 A m^{-1}, the average mixing temperature was 0.5 °K higher than the experimental wall temperature. This was the magnetic field strength with the poorest match between the experimental and model data, which is why the average mixing temperature is skewed past the high side of the temperature profile.

The flowing fluid model was used to calculate a power balance. The power balance helps indicate where the energy flows, and if excessive energy was being lost to the environment rather than the target fluid. A summary of the power balances calculated at 4667 A m^{-1} and flow rates of 5 mL s^{-1} and 12 mL s^{-1} are shown in **Tables 20** and **21**, respectively.

Domain	Power (W)	% of source
Nanopaint source	47.08	
Target fluid	34.23	72.71
Surroundings	13.53	28.74

Table 20–Summary of energy flow from the nanopaint source at 4667 A m^{-1} and a flow rate of 5 mL s^{-1}.

Domain	Power (W)	% of source
Nanopaint source	47.08	
Target fluid	34.39	73.05
Surroundings	12.80	27.19

Table 21– Summary of energy flow from the nanopaint source at 4667 A m^{-1} and a flow rate of 12 mL s^{-1}.

The power balance showing energy flow for the flowing system is nearly identical to the energy balance for the static fluid system. Approximately 73% of the energy generated in the nanopaint flows into the target fluid, while the rest is lost to the surroundings due to convection. Referring back to Figs. 47 and 48 shows why the power balances are so similar. A two-fold increase in flow rate in the model only resulted in a maximum temperature decrease (at the wall) of ~2 °K. Experimentally, a much higher sensitivity in temperature to flow rate was seen, which is indicative of different amounts of mixing occurring at different flow rates. The power balances resulted in similar energy flows to the target fluid since a smaller amount of heat was transferred from the nanopaint to the water, but over a shorter time interval (smaller residence time). The model energy balance is likely only useful for indicating a minimum amount of energy transferred from the nanopaint source to the fluid since it could not account for the fluid temperature change at the center of the flow pathway. It's possible that a greater amount of heat was transferred to the fluid due to the potential mixing that took place.

The power necessary for the power supply to generate a magnetic field strength of 4667 A m^{-1} is ~9.2 kW. Considering the amount of power output from the nanopaint according to the model was only 47 W, such a high power input for such little output seems highly inefficient (~0.5% efficient). The overall efficiency of the process in this

case, however, is not relevant due to the geometry of the nanopaint source, NP loading, and method of EM energy delivery. The apparatus was driven at a constant power load, so regardless of the amount of nanoparticles to heat, the same amount of energy was input. Performing experiments in this manner wastes most of the magnetic energy to the environment since a given mass of NP can only transform a finite amount of magnetic energy into heat. The overall energy balance reveals that using a short, low turn coil to heat a small layer of magnetic nanoparticles is highly energy inefficient. If a long, high turn coil that required much less current to generate the same magnetic field strengths were used, the process would be significantly more efficient. Utilizing a waveguide is another means to minimize the amount of magnetic energy wasted. This method of EM energy delivery will be discussed in the next chapter.

The flowing fluid nanopaint model results did not match experimental results as well as the dispersion and static fluid nanopaint models, but they still yielded valuable results and insight. First, the experimental temperature change at the center of the flow pathway for all magnetic field strengths tested could not be reproduced via the laminar flow model. This suggests that mixing caused additional heat transfer to the center flow layer of the fluid. An apparatus with a much longer laminar entrance and less contractions/expansions around the heated section length could help confirm or deny this conclusion. Second, the flow model was used to evaluate the energy flow from the nanopaint source to its surroundings at the highest magnetic field strength. This evaluation indicated that high power source combined with a low turn coil is a highly inefficient means to deliver magnetic energy to a small mass of nanoparticles. A more efficient apparatus design should be used in the future for evaluation of field applicability.

Chapter 6: Modeling of Electromagnetic Energy Delivery via Waveguide

A key challenge to making magnetic NP heating commercially viable for energy industry applications is finding an efficient and convenient means to deliver the magnetic energy to the NPs. Inserting a coil and painted inserts into a pipeline would be an enormous endeavor that most would not accept as feasible. Wrapping a coil around the pipeline is also impractical due to the skin depth of steel. At the frequencies of interest, the skin depth of steel is so shallow that magnetic waves would not penetrate to the interior of the pipeline where the target fluid is, but rather just propagate along the outside of the steel. As well, the flowing fluid experimental models showed that using a coil to thin annular layers of nanopaint would likely be highly inefficient. Elimination of these approaches leaves an option that is not invasive to the flow pathway, and maximizes the transformation of magnetic energy to heat–using the pipeline as a waveguide. This chapter contains some preliminary results to give an indication of the feasibility of using pipelines as waveguides.

A waveguide is a device used to guide electromagnetic energy from one location to another. Waveguides function as high pass filters, so any electromagnetic energy above a minimum frequency, or cutoff frequency, propagates through the waveguide, while energy below this frequency attenuates. The applicable wave propagation mode is the transverse electric, or TE wave mode (Kong, 1986). For this mode, the magnetic field propagates along the axis of the waveguide, and electric field is orthogonal to the magnetic field; these waves are often called H waves for this reason. Waveguides are highly advantageous for delivering magnetic energy at great distances because above the cutoff frequency, the waves travel without attenuation similar to wave propagation in a vacuum. In the case of a wave traveling down a nanopainted steel pipe, the NPs would

absorb magnetic energy and convert it to heat. The EM wave would lose magnetic field amplitude as it travels down the pipeline due to the nanopaint absorbing and converting the magnetic energy. In this scenario, additional magnetic energy would need to be supplied along the pipeline where calculations show that most of the magnetic energy has been absorbed by the nanopaint. An illustration depicting the delivery of magnetic energy through a pipeline acting as a waveguide is shown in **Fig. 48**.

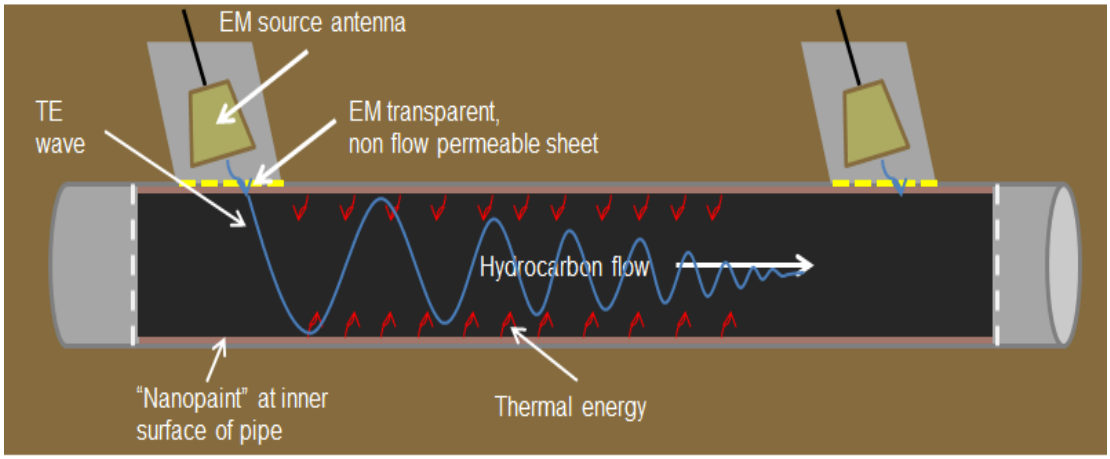

Figure 51–Depiction of hypothetical magnetic energy delivery down a nanopainted pipeline. The pipeline acts as a waveguide to guide the magnetic energy without attenuation losses.

The magnetic energy in Fig. 51 is supplied by electromagnetic source antennae that would be installed into a T-joint in the pipeline. A high strength, non-metallic material could be used as an EM transparent membrane to prevent fluid flow into the T-joint.

Maxwell's wave equation is the defining theory for describing the propagation of a TE wave down a waveguide. The modeling work was executed in the frequency domain to convey the sensitivity of frequency with respect to the cutoff frequency, as

well as the influence of frequency on power transmission within the waveguide. The frequency domain wave equation solved by COMSOL is shown in Eq. (32).

$$\nabla \times \mu_r^{-1}(\nabla \times \mathbf{E}) - k_O^2(\varepsilon_r - \frac{j\sigma}{\omega\varepsilon_O})\mathbf{E} = 0 \tag{32}$$

where

$$k_O = \omega\sqrt{\varepsilon_O \mu_O} = \frac{\omega}{c_O} \tag{33}$$

and μ_r is the relative magnetic permeability, $\boldsymbol{E}$ is the electric field [V m^{-1}], k_O is the wave number of free space (described by Eq. 33), ε_r is the relative electric permittivity, ω is the angular frequency ($2\pi f$), σ is the electric conductivity [S m^{-1}], and c_O is the speed of light in a vacuum ($3 \cdot 10^8$ m s^{-1}).

The pipeline was modeled via COMSOL with a 2D axial-symmetric geometry. Cylindrical waveguides have a cutoff frequency described by Eq. (34).

$$f_c = \frac{1.8412}{2\pi a\sqrt{\mu\varepsilon}} \tag{34}$$

where a is the pipe radius [m], $\mu = \mu_O\, \mu_r$ [m kg s^{-2} A^{-2}], and $\varepsilon = \varepsilon_O\, \varepsilon_r$ [m^{-3} kg^{-1} s^4 A^2]. The cutoff frequency is what generally restricts the use of waveguides to the microwave frequency range. As an example, a pipeline with a 3 ft. diameter, filled with air, would have a cutoff frequency of ~190 MHz. Even for a large diameter pipeline, frequencies 1000 times larger than those experimentally tested would be necessary. Electromagnetic

frequencies in this range are commonly produced by an antenna. The design of such antennae is beyond the scope of this research.

The 2D axial-symmetric model built in COMSOL has a simple geometry consisting of the pipeline containing a fluid (static) within the pipeline wall. The velocity (or lack thereof) of non-magnetic fluids does not affect the wave equation calculations. The introduction of electromagnetic energy to the pipeline waveguide is through a coaxial port for which an input power is defined. An outlet port is also used at the waveguide exit to discontinue the wave excitation. The pipeline used to demonstrate the functionality of a waveguide is 1 ft. in diameter, has a 1 inch pipe wall thickness, and is 5 m in length. COMSOL does not have a magnetic relaxation physics module to represent relaxational losses, so this model will only serve to depict the use of a pipeline as an electromagnetic waveguide. An illustration of the pipeline geometry is shown in **Fig. 52**.

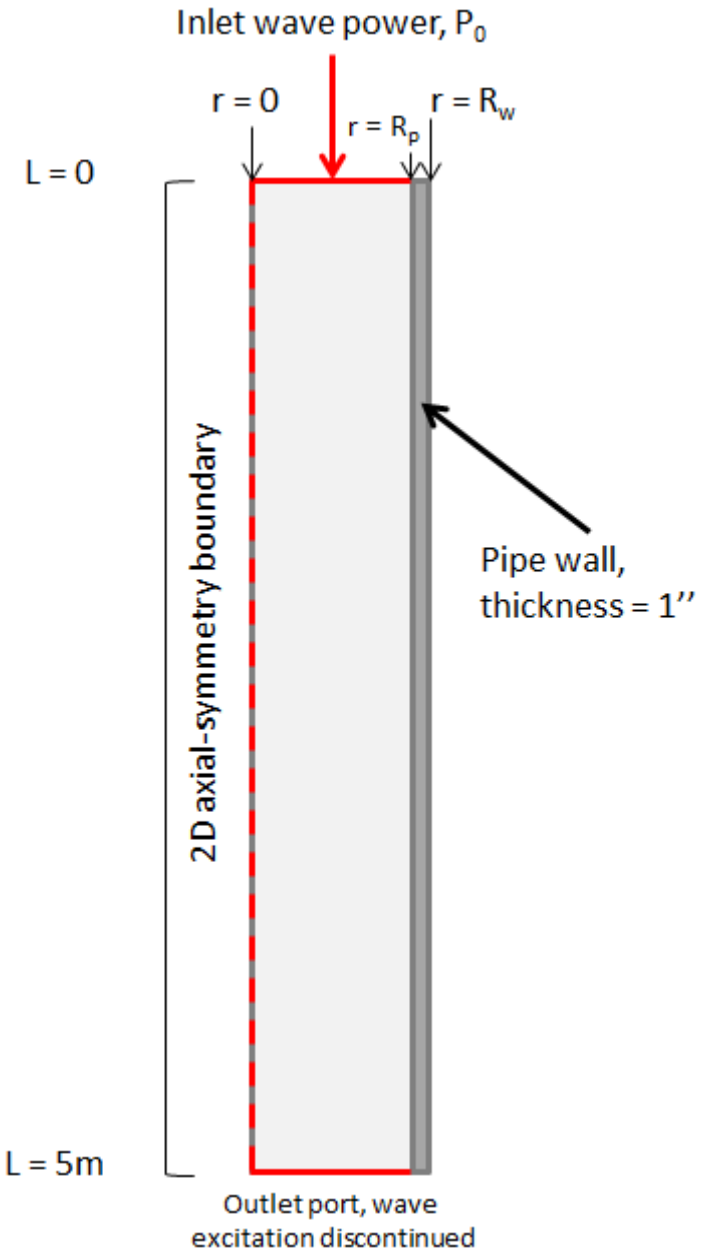

Fig. 52–Pipeline geometry used to model waveguide concept in COMSOL.

The actual thickness of the pipe wall is not what induces the reflections of the electromagnetic wave down the pipeline, but rather the electrical properties of the pipe

itself, in this case steel. Specifically, the large electrical conductivity of steel (~$4 \cdot 10^6$ S m^{-1}) is what enables it to be a suitable material for a waveguide.

The boundary conditions for the model geometry shown in Fig. 52 are simple and aim to focus the study on waveguide operation. As in the previous 2D axial-symmetric models discussed, a symmetry boundary condition was applied at the center of the pipe, or $r = 0$. A wave excitation port was assigned at $L = 0$ for $0 < r < R_p$. This boundary condition is mathematically described by Eq. (35).

$$S = \frac{\int_{\partial\Omega} (\mathbf{E} - E_1) \cdot \mathbf{E}_1}{\int_{\partial\Omega} \mathbf{E}_1 \cdot \mathbf{E}_1} \tag{35}$$

where S is the scattering parameter (S-parameter), which describes the frequency dependent transmission and reflection of electromagnetic energy, $\boldsymbol{E}$ is the electric field vector, E_1 is the first component of the electric field scalar, and $\boldsymbol{E_1}$ is the first component of the electric field vector. They are often used in conjunction with waveguides to describe the energy transmission from antennae, ports, and transmission lines (COMSOL Multiphysics, 2010). A similar port boundary condition was used at $L = 5$ m and $0 < r < R_p$ to describe the termination of the electromagnetic wave; the termination port is mathematically described by Eq. (36).

$$S = \frac{\int_{\partial\Omega} \mathbf{E} \cdot \mathbf{E}_2}{\int_{\partial\Omega} \mathbf{E}_2 \cdot \mathbf{E}_2} \tag{36}$$

where $\boldsymbol{E_2}$ is the second component of the electric field vector. Last, a perfect electric conductor boundary was applied at $r = R_w$ and 0 m $\leq L \leq$ 5 m. This type of boundary

condition sets the tangential component of the electric field to zero. It's used to describe the behavior of a lossless metallic conductor, which is applicable for the outer wall of a waveguide since the magnetic energy is reflected at the interior wall (COMSOL Multiphysics, 2010). The perfect electric conductor boundary condition is mathematically described by Eq. (37)**.**

$$\mathbf{n} \times \mathbf{E} = 0 \tag{37}$$

where *n* is the unit normal vector directed out of the perfect conductor surface.

This model will demonstrate waveguide sensitivity to frequency, and how important attaining a minimum cutoff frequency for wave propagation. The model dimensions are those shown in Fig.52. The internal pipe fluid in this case is air; simulations with applicable pipeline fluids will also be discussed later to demonstrate that they do not degrade waveguide performance. An inlet power of 5 kW was used at the wave excitation port (L = 0 m). For a TE wave propagating in a cylindrical waveguide, the azimuthal (θ) component of the magnetic field propagates in the direction of the waveguide axis.

Figure 53 shows surface plots of the magnetic field strength for frequencies between 550 MHz and 900 MHz. The cutoff frequency is theoretically ~576 MHz for a 1 ft. diameter pipe, however, the COMSOL simulations calculates it to be somewhat higher.

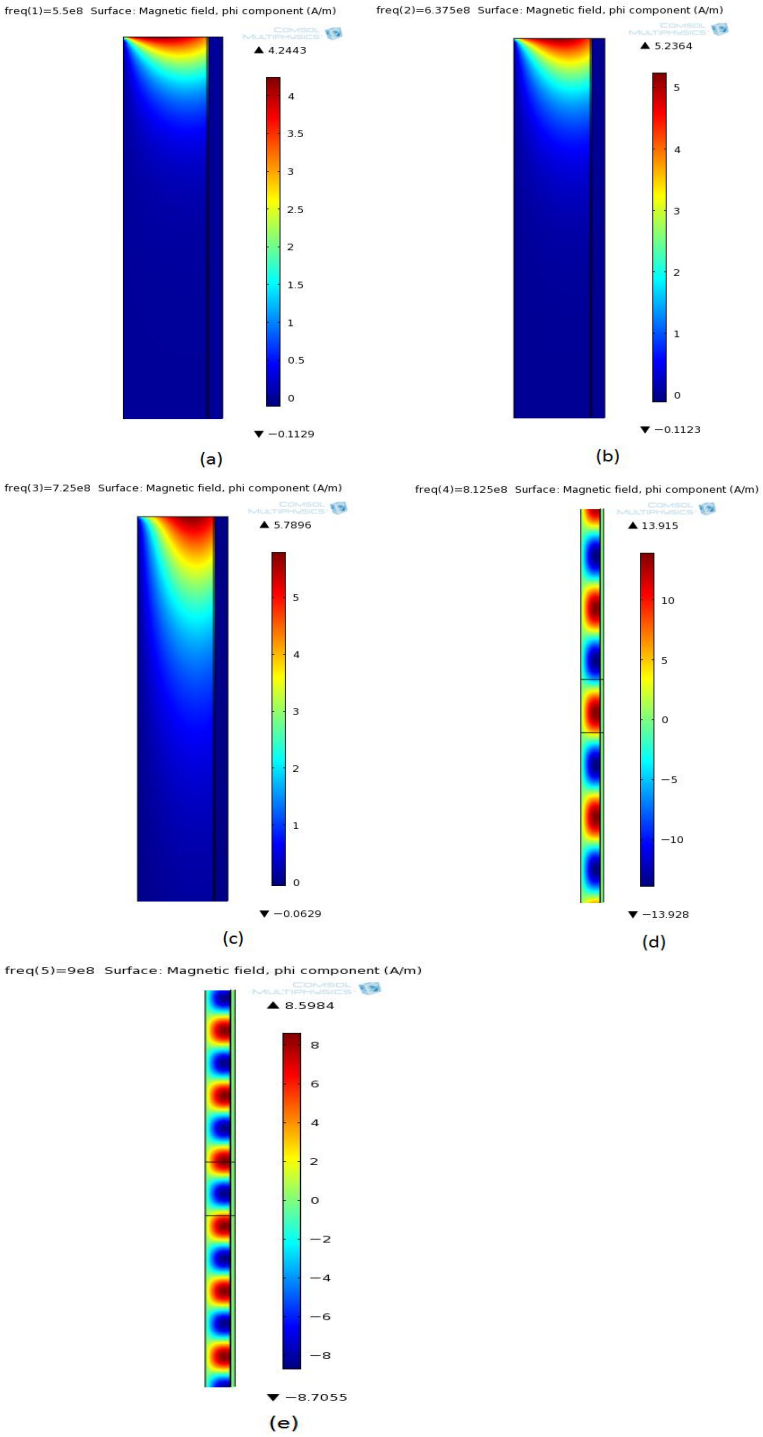

Figure 53–Surface plots of phi component of magnetic field strength down 1 ft. inner diameter pipeline waveguide filled with air for frequencies of (a) 550 MHz, (b) 638 MHz, (c) 725 MHz, (d) 813 MHz, and (e) 900 Mhz.

It's apparent that the cutoff frequency has not been achieved for frequencies from 550 MHz – 725 MHz. The magnetic field strength quickly dissipates within a few feet (length) of the source boundary. As the frequency increases, the wavelength shortens, and the magnetic field propagates slightly further and at a higher strength. At a frequency of 813 MHz, the cutoff has been attained and the TE wave propagates endlessly without attenuation unless poor joints or pipe imperfections cause standing waves in the pipe. As stated before, the wave will also dissipate due to the conversion of magnetic energy to heat when the superparamagnetic NP paint is present. The alternating maximum and minimum magnetic field strength hot spots are present due to the sinusoidal shape of the TE wave propagating down the axis of the pipe. The maximum field strength zones correspond to the peaks of the sine wave, while the minimum zones correspond to the troughs. Inspection of (d) and (e) reveal that an optimum frequency was surpassed between 813 MHz and 900 MHz, which is indicated by the decrease in the maximum magnetic field strength propagating at the inner pipe surface. The cutoff frequency was actually also found to be the optimum frequency at which the highest magnetic field strength propagates as shown. **Figure 54** shows that this frequency is at 758 ± 5 MHz.

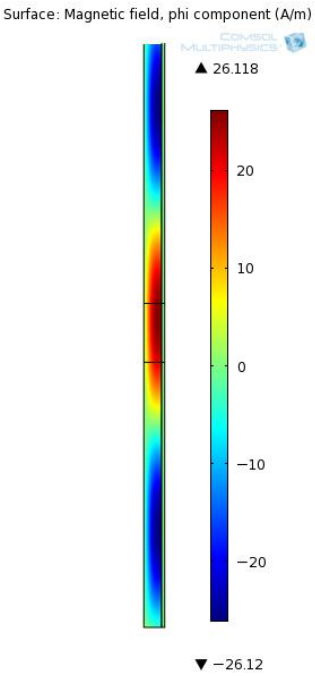

Figure 54–Surface plot of the phi component of the magnetic field strength at the cutoff frequency for a 1 ft. inner diameter steel pipe filled with air. COMSOL calculates the cutoff frequency as 758 ± 5 MHz.

The maximum magnetic field strength of the propagating wave in Fig. 54 is ~26 A m^{-1} compared with ~14 A m^{-1} at a frequency of 813 MHz shown in Fig. 53(d). For the 5m section of pipe, the length over which the wave in Fig. 54 has a magnetic field strength greater than 15 A m^{-1} is ~1.5 m, whereas in Fig. 53(d) the wave has a magnetic field strength of ~8 – 13 A m^{-1} for ~1.5m of the pipe length. **Figure 55** shows how the magnetic field strength varies as a function of length down the pipe for a frequency range of 750 MHz – 780 MHz.

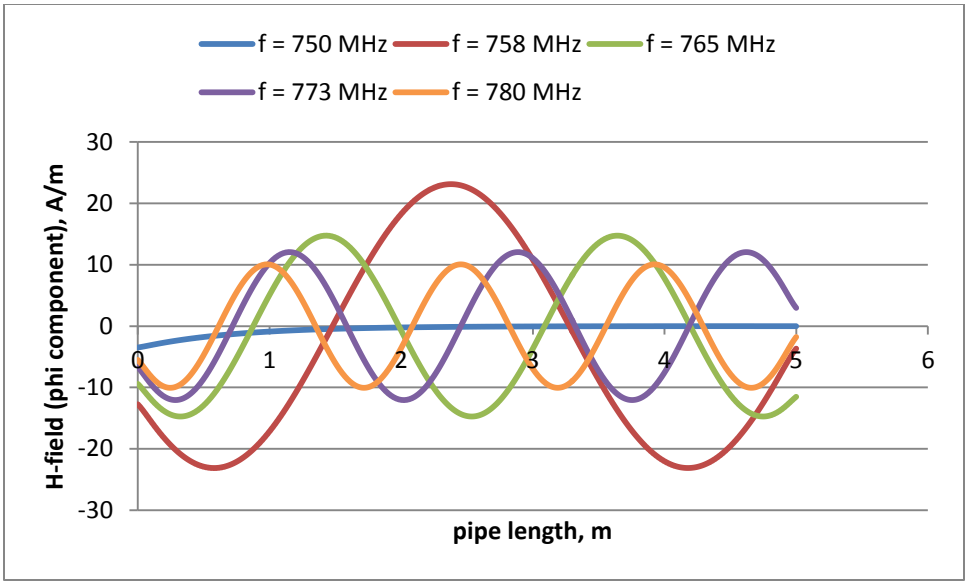

Figure 55–Variance of magnetic field strength as a function of length down the 1 ft. diameter pipe for a frequency range of 750MHz – 780 MHz.

Beyond the cutoff frequency at 758 MHz, an increase in frequency results in a decrease in the peak magnetic field strength of the wave. For magnetic heating, the power dissipated has a quadratic dependence on the magnetic field strength (see Eq. (10); not always true experimentally, as demonstrated previously), so wave propagation right at the cutoff frequency is ideal.

The magnetic field strengths shown in Fig. 55 are two orders of magnitude smaller than the theoretical experimental H-fields tested. This is an effect of using an excitation port boundary condition with 5 kW of power to introduce the TE wave to the waveguide. For a cutoff frequency of 758 MHz, the ideal Fe_3O_4 NP diameter is 10 nm. At this size, a magnetic field strength of 200 A m^{-1} yields an SLP from the NPs of ~5 W/g. This would likely be the minimum magnetic field strength desired for adequate pipe heating to occur over long times, even though, this is a design parameter to be designed for each scenario. Using a custom built antenna for which the power of the wave resulted

in high magnetic field amplitudes would remedy this issue, but this is beyond the scope of the current work.

Next, simulations were performed to evaluate the effect of introducing different fluids into the pipe. For field applications, the presence of water or brine, a hydrocarbon gas, and a hydrocarbon liquid inside of the pipe are of most interest. All of these fluids have a relative magnetic permeability of ~1 due to their non-magnetic nature, but all have different electric permittivities which influence the cutoff frequency. According to Eq. (34), the larger the electric permittivity of the fluid, the lower the cutoff frequency. Materials with a higher electric permittivity better store charges from electric fields and transmit the energy, so EM waves travel more efficiently within these materials (Kong, 1986). **Table 22** summarizes the fluids used for the simulations and their corresponding theoretical and COMSOL derived cutoff frequency for a 1 ft. ID steel pipe.

Fluid at 293 °K (phase)	μ_r	ε_r	**Theoretical f_c, MHz**	**COMSOL f_c, MHz**	**Max H-Field, A/m**
Brine (*l*)	1	88	61	80.5	34
Decane or Gasoline (*l*)	1	2	408	534	97
Methane (*g*)	1	1	576	758	23
Air (*g*)	1	1	576	758	23

Table 22– Summary of relevant magnetic and electric fluid constants for calculating waveguide cutoff frequencies for various applicable pipeline fluids.

Most liquid hydrocarbons have a relative electric permittivity of ~2, which is why decane/gasoline were selected as the representative liquid hydrocarbons for this study. Table 22 indicates that COMSOL calculates the cutoff frequency to be ~31% higher than the theoretical cutoff frequency. It also shows that as the relative electric permittivity increases, the cutoff frequency decreases as discussed previously. Since methane and water have approximately the same relative magnetic permeability and electric permittivity, they behave the same in a waveguide at 293 °K. As the frequency approaches the precisely ideal cutoff frequency, the field maximum H-field that propagates in the azimuthal direction also approaches a maximum as seen for the decane or gasoline case. The magnetic field strength as a function of distance down the pipe waveguide at the approximate cutoff frequency is shown for the simulated fluids in **Fig. 56**.

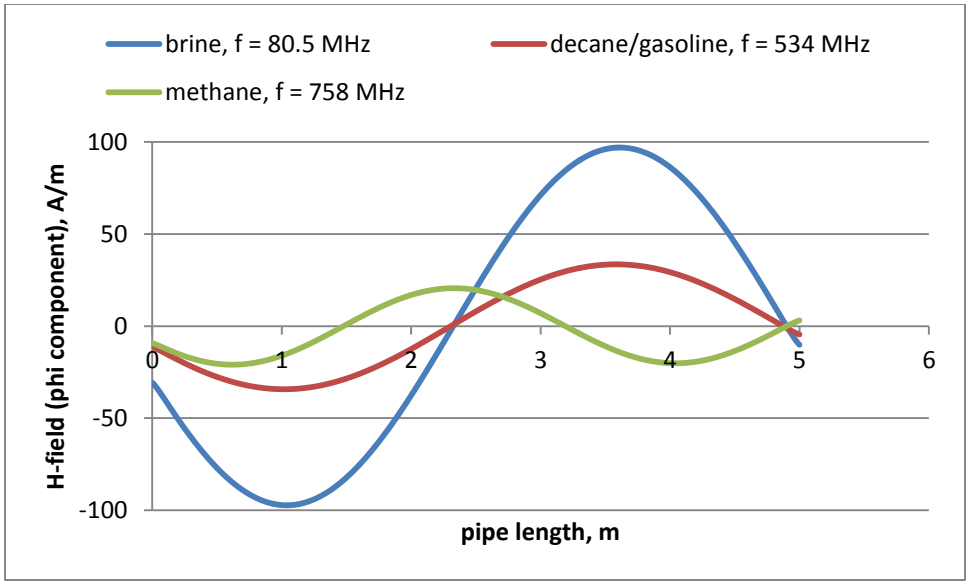

Figure 56–Variance of magnetic field strength as a function of waveguide length for brine, decane/gasoline, and methane at their approximate cutoff frequencies (±1 MHz).

The curves shown in Fig. 56 represent a pipe filled completely with a single fluid. In real applications, a pipeline would likely have a mixture of fluids and phases in which case the magnetic and electric properties would be weighted based on the volume fractions of the fluids present. While not demonstrated in this study, the cutoff frequency is proportional to the inverse of the pipeline diameter, so larger diameter pipes would have lower cutoff frequencies, and smaller diameter pipes would have higher cutoff frequencies.

The feasibility of utilizing a steel pipeline as a waveguide for directing magnetic energy from a source location to a desired heating location has been demonstrated. The importance of designing the wave source for the pipeline fluid and pipeline diameter has been discussed. A wave source generator that produces a wave precisely at the cutoff frequency with a maximal magnetic field strength is essential to converting as much magnetic energy to heat as possible. As well, the NPs in the nanopaint will also need to be designed to produce the most heat at the waveguide cutoff frequency.

Chapter 7: Conclusions

7.1 Experimental Conclusions

- Proof-of-concept experiments for the nanoparticle (NP) dispersion heating experiments were initially performed using 10 nm hydrophilic NPs (commercially provided) dispersed in water. The experiments performed the low frequency tests (down to 1 kHz) throughout the experimental work and at a theoretical magnetic field amplitude of 11.2 kA m^{-1}. Results indicated that the nanoparticles heated the dispersing fluid at a rate linearly dependent on the nanoparticle dispersion

concentration. As well, the results showed that the nanoparticles generate heat even at frequencies as low 1 kHz (as predicted by Rosensweig). Even at nanoparticle dispersion concentrations as high as 27 wt%, the SAR was only ~0.10 W/g Fe_3O_4 (ΔT = 1.8 °C), which was not deemed adequate for the target applications, so higher frequencies were explored.

- Higher frequency (390 kHz – 930 kHz) nanoparticle dispersion experiments were also conducted at varying magnetic field strengths (500 A m^{-1} – 5000 A m^{-1}) to characterize the nanoparticle heating response to varying frequency and magnetic field strength. Experiments were conducted with hydrophilic nanoparticles dispersed in water and hydrophobic nanoparticles dispersed in hexane and THF; both types of particles were commercially provided at a nominal Fe_3O_4 core size of 10 nm. Both hydrophilic and hydrophobic NP experiments showed a significant increase in SAR values (from ~10 – 200 W/g and ~5 – 40 W/g, respectively) for increasing magnetic field strength, but the expected quadratic trend in SAR with H-field was not seen. As well, hydrophobic experiments showed a slightly positive trend in SAR with frequency, while hydrophilic experiments showed a slightly negative trend in SAR with frequency where a positive trend in SAR with frequency was expected according to Rosensweig's theory. These deviations from theory led to the conclusion that Rosensweig's theory, which considers a single nanoparticle, inadequately handles a system of multiple nanoparticles dispersed in a fluid medium. Furthermore, it was concluded that the large difference in heating rate between the hydrophilic and hydrophobic nanoparticles was due to deviations from the expected NP size of 10 nm. From a single NP perspective, small deviations in particle size result in large differences in theoretical heating rates. The dispersing fluid properties other than

the specific heat capacity might have minor effects on experimental heating rates, but modeling shows that fluid thermal conductivity has no affect at the experimental time scale used.

- By operating at frequencies higher than 100 kHz, stationary particle heating via Neel relaxation can be achieved. This concept was proved by embedding the particles in a solid epoxy resin substrate dubbed “nanopaint”, and performing fluid heating experiments using the nanopaint. Localized heating at specific surfaces was made possible by use of nanopaint.
- Nanopaint experiments with a static fluid were conducted by coating the interior of a PVC tube with nanopaint, and recording the transient heating behavior of the fluid. It was found that there was a decrease in heating effectiveness with increased magnetic field amplitude. While more heat was generated at higher field amplitudes, the geometry of the experiments caused the system to be conduction limited, so the total additional amount of heat generated was not transferred to the center of the fluid (temperature measurement point), but rather to the PVC tube and convected to the air. Based on these findings, it’s possible to design an “optimal” batch heating system given the dimensions and time scale over which heating is to take place, so the heat lost to the atmosphere is minimized and conduction is not a limiting factor.
- Static fluid experiments as a whole (dispersed particles and embedded particles) indicate that the spatial distribution of particles with respect to the target medium, as well as the thermal properties of the dispersing/embedding medium greatly affect the magnitude of resulting SAR values. For a given frequency and field amplitude, SAR values were up to five times higher for NPs dispersed throughout the target fluid (water in this case) than for particles at the periphery of the target

fluid. This is likely due primarily to heat being generated in small spherical domains throughout the target fluid (relatively small diffusion distance) rather than conducting from the exterior to the interior of the fluid (relatively large diffusion distance), and secondarily due to the fluid/paint thermal properties.

- Steady-state flowing fluid experiments were also performed using a nanopainted PVC tube. Experimental results indicated that efficient heat transfer could not take place outside of the laminar flow regime for the dimensions of the apparatus and spatial placement of the nanopaint. The following system parameters are important for optimization of a flowing system with heat transferred from nanopaint at the tube wall: flow rate, tube diameter, nanopaint thickness/concentration, and the length of the painted tube section. Three of these four quantities affect the residence time for fluid contact with the heating surface. It was found that the heating rate of the flowing fluid was up to three times higher than that of the static fluid. In this case**,** mixing effects combined with an increased temperature gradient between the nanopaint and the flowing fluid were the key factors which improved heat transfer.

7.2 MODELING CONCLUSIONS

- Microscopic dispersion heating models were generated to simulate a single nanoparticle generating heat surrounded by a finite sphere of fluid. The size of the surrounding fluid sphere was dictated by the NP diameter and the wt% of the nanoparticle dispersion to be simulated. The heat generation value assigned to the nanoparticle is the SAR obtained from the respective experiment or the SLP estimated via Rosensweig's equation. The models generated for water and THF at

400 kHz and 5000 A/m closely matched the experimental temperature vs. time data, while the model for hexane produced larger temperatures (~28%) for a given time than experimentally seen. The reduced experimental temperature compared to the model was attributed to poor dispersion quality (NP settling). The slope of the linear portion of the heating rate curves approximately matched for the models and experiments generated in all cases, so it was concluded that consideration of a particle within an adiabatic fluid sphere adequately models the dispersion experiments.

- Modeling results indicated that the radial dependence of temperature for the NP/fluid sphere system disappears at the "macro" or experimental time scale for all dispersion wt%'s tested. This indicates that the "transient" nature of the problem disappears at the experimental time scale, and the thermal conductivity of the fluid has no influence on the system at these times.
- Modeling results showed that increasing the radius of the fluid sphere surrounding the NP by a factor of 4 increased the time required to reach the same temperature by 64 times. This indicates that the fluid sphere temperature is linearly dependent on the volumetric heat generation of the NP (cubic relationship for sphere).
- The size of the fluid sphere surrounding the NP is a function of the wt% of the nanodispersion. The radius of the fluid sphere was adjusted to model 1 wt%, 0.1 wt%, and 0.01 wt%. Results showed that radial temperature differences within the sphere became negligible at times cubicly dependent on the size difference between the fluid spheres for each nanodispersion concentration; e.g., from 1 wt% to 0.1 wt%, there is approximately a two-fold increase in the fluid sphere radius, so the radial temperature distribution within the sphere became negligible 8 times later for the 0.1 wt% case. This further confirms that the dispersion heating rate is

purely dependent on the volumetric heat generation of the NP and the wt% of the dispersion.

- A model was generated to simulate the transient heating of a nanopainted tube filled with static fluid (water). It was found that the thermal conductivity of the fluid largely dictated the time at which the center of the fluid showed a temperature response to the nanopaint heat generation. As well, the thermal conductivity of the nanopaint has no noticeable influence on the transient behavior of the system. The convective heat transfer coefficient of air only has a substantial influence on the temperature of the PVC tube and no noticeable influence on the temperature profile of the fluid.
- Further sensitivity analysis of the nanopainted tube model with a static fluid helped verify some of the uncertain nanopaint properties. It was found that the nanopaint NP concentration was 30 wt% and had a thickness of 600 μm, which confirmed the original nanopaint formulation and drying thickness mentioned in the methods section of Chapter 4.
- Comparison of the nanopaint tube model with a static fluid to experimental results indicated that linearly scaling the Q_p value for a magnetic field strength of 4667 A m^{-1} down for the models at lower magnetic field strengths produced a much better experimental to model match. A linear relationship between SAR and H was experimentally observed for the hydrophobic NPs at 430 kHz, which justified scaling the heat source term at lower magnetic field strengths in this manner. Experimental results still showed a larger amount of heat was transferred to the center of the fluid at the lower magnetic field strengths than the model could account for even after the Q_p scaling adjustment. It was hypothesized that convective over turn contributed to convective mixing taking place in the system,

which enhanced heat transfer to the center of the fluid. Calculation of the "well-mixed" water temperature for the system, based on model energy balances, supported the potential for the occurrence of convective over turn.

- The static fluid nanopainted tube model also showed that from a purely heat transfer perspective, the conduction/convection behavior of the system did not vary with increasing magnetic field strength. For all theoretical magnetic field strengths tested, the model showed that ~74% of the nanopaint heat flowed into the target fluid, while 26% flowed into the tube and surroundings. This hints that the reason for the experimental decrease in heating efficiency with increased magnetic field strength was likely due to the actual magnetic field strength being less than theoretically calculated or the magnetic response of the NPs decreasing at higher nanopaint temperatures.
- The matched model values from the static fluid nanopainted tube model were used to generate a flowing fluid nanopainted tube model. Comparison of the experimental temperature data to the model data indicated that the model could not account for the experimental fluid temperature change at the center of the flow pathway in laminar flow conditions. From this it was concluded that the upstream head pump (bucket) inlet and a 60° tubing bend likely induced some turbulent mixing that perpetuated downstream to the nanopaint heating zone and caused heat transfer to the center of the flow path. Calculation of the cup-average mixing temperature of the water from integrating the model radial temperature curves supported the hypothesis that turbulent mixing occurred in the flow system. The cup-average mixing temperature fell between the experimental centerline and wall temperatures at each magnetic field strength.

- Modeling of a hypothetical steel pipeline as a waveguide yielded some valuable insight. It was found that the closer the EM wave frequency is to the pipe cutoff frequency, the higher the magnetic field strength that propagates down the pipe (for a given EM wave power source). It was also found that common pipeline liquids lower the cutoff frequency required for wave propagation in the pipe due to having a relative electric permittivity greater than 1, while common pipeline gases do not affect the pipe cutoff frequency relative to air.

7.3 FUTURE WORK

- To help refine the NP heating characterization experiments that were performed, the actual magnetic field strengths in all coils tested should be measured using an H-field probe. This would help distinguish if improper theoretical H-field values were being applied to experimental curves, or if another source of error was causing a mismatch between experiments and theory.
- For the nanopainted tube flow experiments, it was concluded that mixing effects at the inlet of the nanopaint section caused heating at the center of the flow pathway in contrast to what the models predicted should happen. The apparatus should be refined so that the nanopainted tube section is far downstream from any bends, expansions, or contractions that could lead to flow stream mixing. This would help differentiate if mixing effects or other phenomena contributed to enhanced heat transfer to the fluid.
- Using the high frequency induction heating apparatus described in Chatper 3, several experiments can still be performed to further understanding. Construction and installation of a longer coil would enable experiments with longer

nanopainted pipe sections to be performed. With the appropriate nanopaint heating length, the effects of turbulent flow rates could be quantified since the residence time of the fluid in contact with the nanopaint would be higher. As well, the ability of superparamagnetic nanoparticles adsorbed to the interior walls of rock cores could be evaluated for heating heavy oil.

- Models that couple the nanoparticle transformation of electromagnetic energy to heat energy via relaxational physics to momentum transfer need to be developed. This type of model could predict the distance down a waveguide pipeline that a given wave could propagate before all of its energy were converted from magnetic to heat energy by a nanopaint coating. Such modeling work would establish how many wave source stations along a pipeline would be needed for a given length to heat the entire pipe length.
- Much development is needed on the electromagnetic hardware side of the research. It is currently unknown to the researchers what the maximum wave power a given antenna can generate at a given frequency. It is also unknown how this power input translates to the magnetic field strength of the wave. Full characterization of different antennae types with the ability to produce TE waves, coupled with the modeling work, would enable full scale efficiency calculations to be performed, and thus the feasibility of the project being economically validated.

Appendices

APPENDIX A: ADDITIONAL IMAGES.

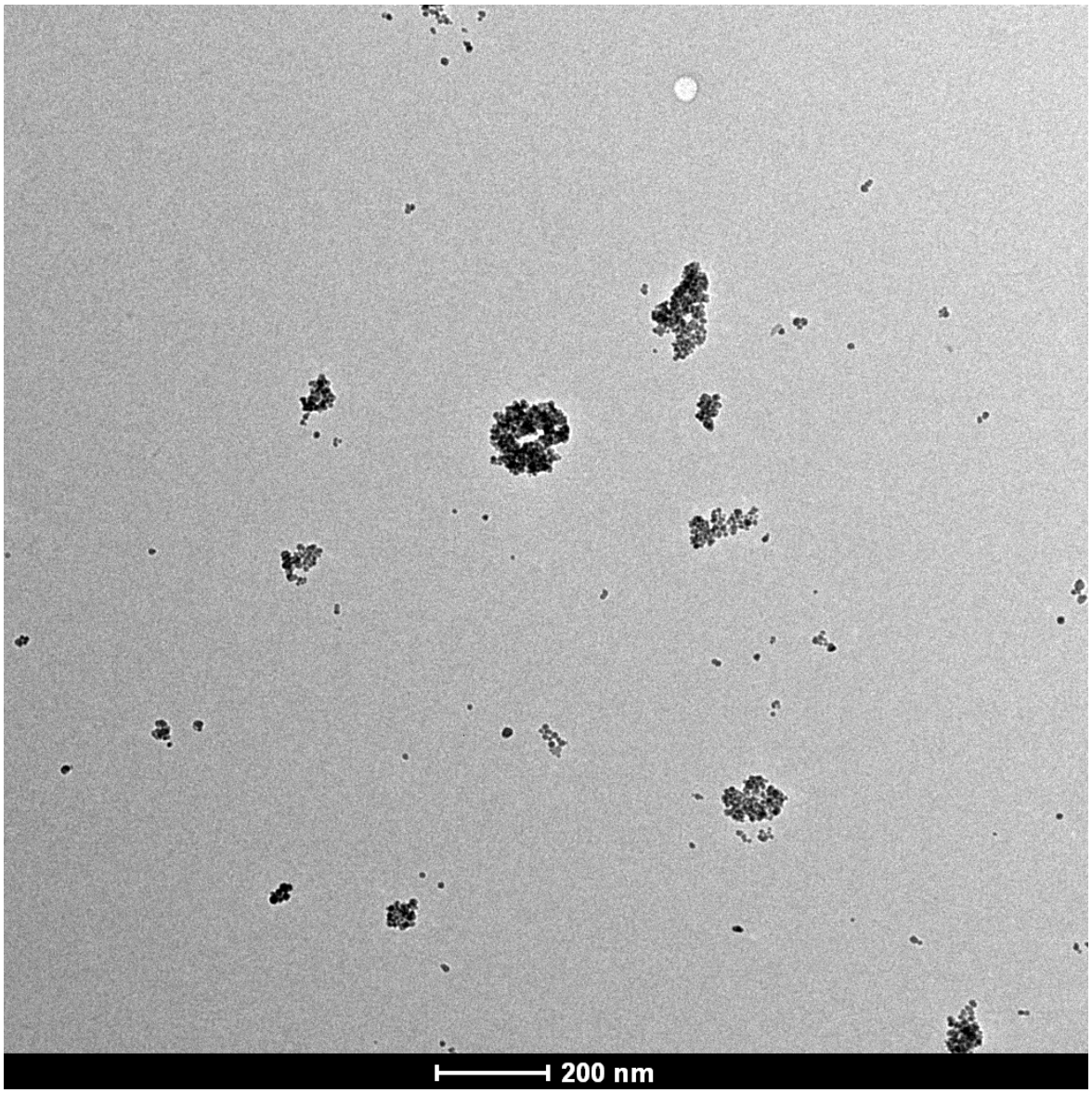

Figure A1–Additional hydrophobic TEM image used for determining hydrophobic mean NP size. The mean NP size resulting from the analysis of this image was 11.4 ± 6.6 nm. This image was not zoomed as far as the other images taken which resulted in a higher degree of uncertainty in the analysis.

APPENDIX B: COMSOL MODELING GUIDE

An extensive modeling guide with access to examples and additional walkthroughs can be found on the COMSOL website (http://www.comsol.com). Included here is a basic step-by-step guide for setting up a model, and analyzing the output. This walkthrough will demonstrate as an example how the "Dispersed Nanoparticle Experimental Model" from Chapter 5.1 was set up.

1) To set up a new model, first open an accessible version of COMSOL; in this walkthrough, COMSOL v4.1a will be used. Upon opening, the COMSOL model wizard will prompt you to select a Space Dimension. For this example, choose the 3D space dimension.
2) Next, you will select the appropriate physics that describe your system. Multiple physics modules can be added to a single model if coupled physics is necessary. Some coupled physics modules already exists, e.g., the Non-Isothermal Flow module combines momentum and heat transfer. This is the module that was used for the flowing fluid nanopainted tube model in Chapter 5.3. Physics modules can also be added to a model after the model has been created. For this example, we will choose "Heat Transfer (ht)" and then select "Heat transfer in fluids (ht); next click the "+" symbol to add the physics to your model. Also selected "Heat transfer in solids (ht)" and click the "+" symbol. Consideration of solid and fluid heat transfer is necessary for this system since we are considering a solid nanoparticle surrounded by a fluid medium.
3) Next, you will be prompted for the study type. In this case, we're interested in investigating the transient behavior of the system since the dispersions

were heating with time. In the case of a steady-state, flow experiment, a stationary study type would be appropriate. The COMSOL graphic user interface that appears upon finalizing the study type is shown in **Fig. B1**.

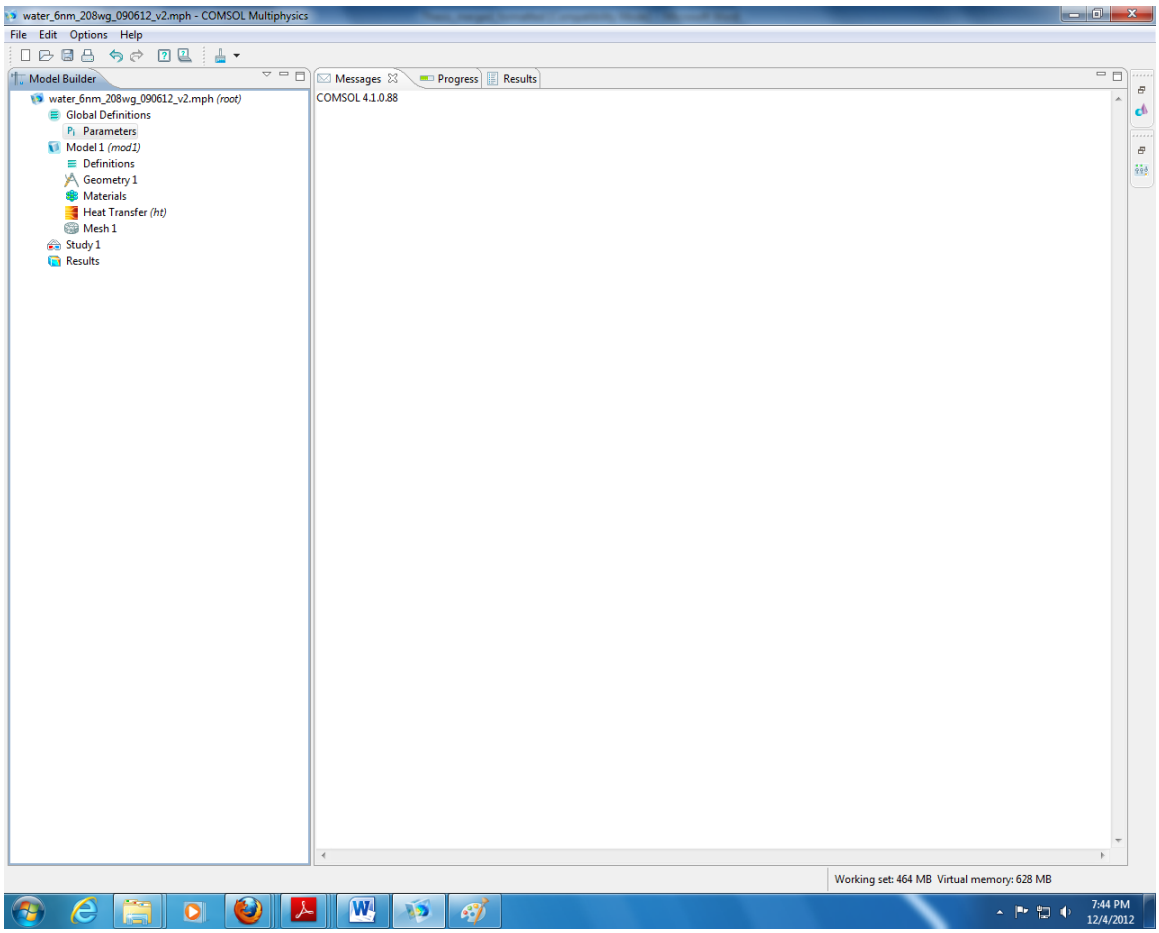

Figure B1–COMSOL graphic user interface from which models are built.

4) Next, right click the "Global Definitions" tab on the "Model Builder" menu at the right side of the interface and click "Parameters." This will enable the addition of constants to the model. Constants can be entered as a function of

other constants, and COMSOL will automatically compute the value. It is wise to also specify the units of the constants, and appropriately label what they signify in the "Description column." Variable names already used by COMSOL cannot be set as constant parameters without inducing an error in COMSOL; e.g. *T* cannot be used as a parameter in the heat transfer models because COMSOL already uses the variable for temperature. In the case of the dispersion model, we'll need to set the heat source term for the nanoparticle, Q_p, the radius of the nanoparticle, *a*, the radius of the enclosing fluid sphere, *b*, the intial system temperature (set to 0 K so that the temperature difference can be easily calculated), T_i, the thermal conductivity of the NP, *k_NP*, the density of the NP, *rho_NP*, and the specific heat capacity of the NP, *Cp_NP*. The parameters list is shown in **Fig. B2**.

▾ Parameters

Name	Expression	Value	Description
Qp	1.077E9[W/m^3]	1.077E9 W/m³	NP heat gen
a	6.9*10^(-9)[m]	6.9E-9 m	NP radius, m
b	25.74*10^(-9)[m]	2.574E-8 m	fluid shell radius, m
T_in	0[K]	0 K	initial temp
k_NP	9.7[W/m/K]	9.7 W/(m·K)	thermal cond. of NP
rho_NP	5180[kg/m^3]	5180 kg/m³	density of NP
Cp_NP	653.42[J/kg/K]	653.4 J/(kg·K)	Spec. heat cap. of NP

Figure B2–Example of parameters list used for NP dispersion heating model.

5) Next, the coordinate system and geometric view preferences can be specified in the "Definitions" tab. The coordinate system will depend on the dimensional modeling space selected. In this case, a 3D geometry was used,

and only behavior in the r-direction is of interest, so Global Cartesian coordinates are sufficient. If necessary, variable names, and functions can also be defined in the Definitions tab. A more explicit guide for creating variable functions can be found in the COMSOL manual.

6) Now the model geometry can be defined. In this case a sphere of radius *a* enclosed by a sphere of radius *b* sufficiently describes the system. Right click the "Geometry" tab and add a sphere to the model. An interface similar to the one in **Fig. B3** will appear, and in this case, should be filled in according to the NP dispersion model dimensions.

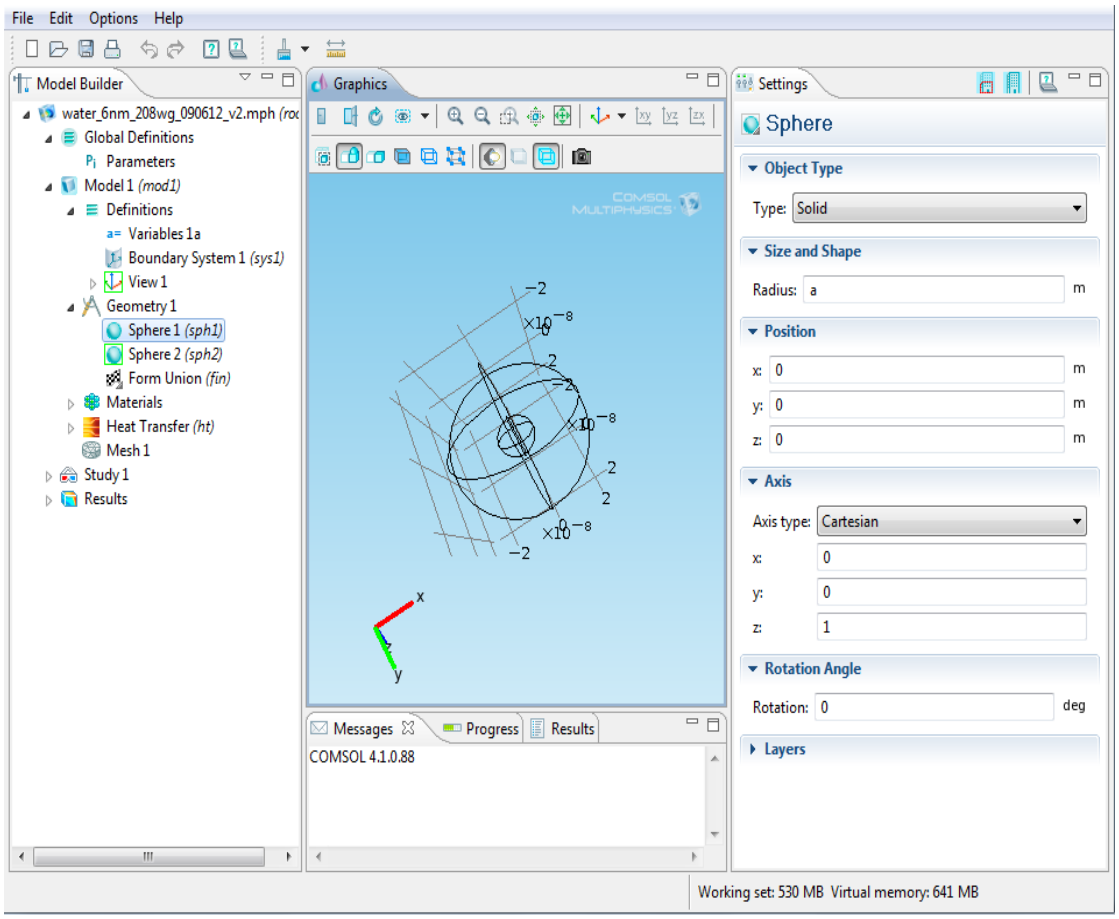

Figure B3–COMSOL Geometry interface for adding shapes of varying dimensions to the model. In the case of the NP dispersion heating model, spherical geometries described the system.

7) After defining the appropriate geometries, the materials that define those geometries must be input to the model. Right click the "Materials" tab and open the material browser. Search to see if COMSOL has pre-defined a material to be used in the model. In this case, liquid water has already been defined in the material library. Right click the water listing and add it to the model. The COMSOL Material Browser Library is shown in **Fig. B4**.

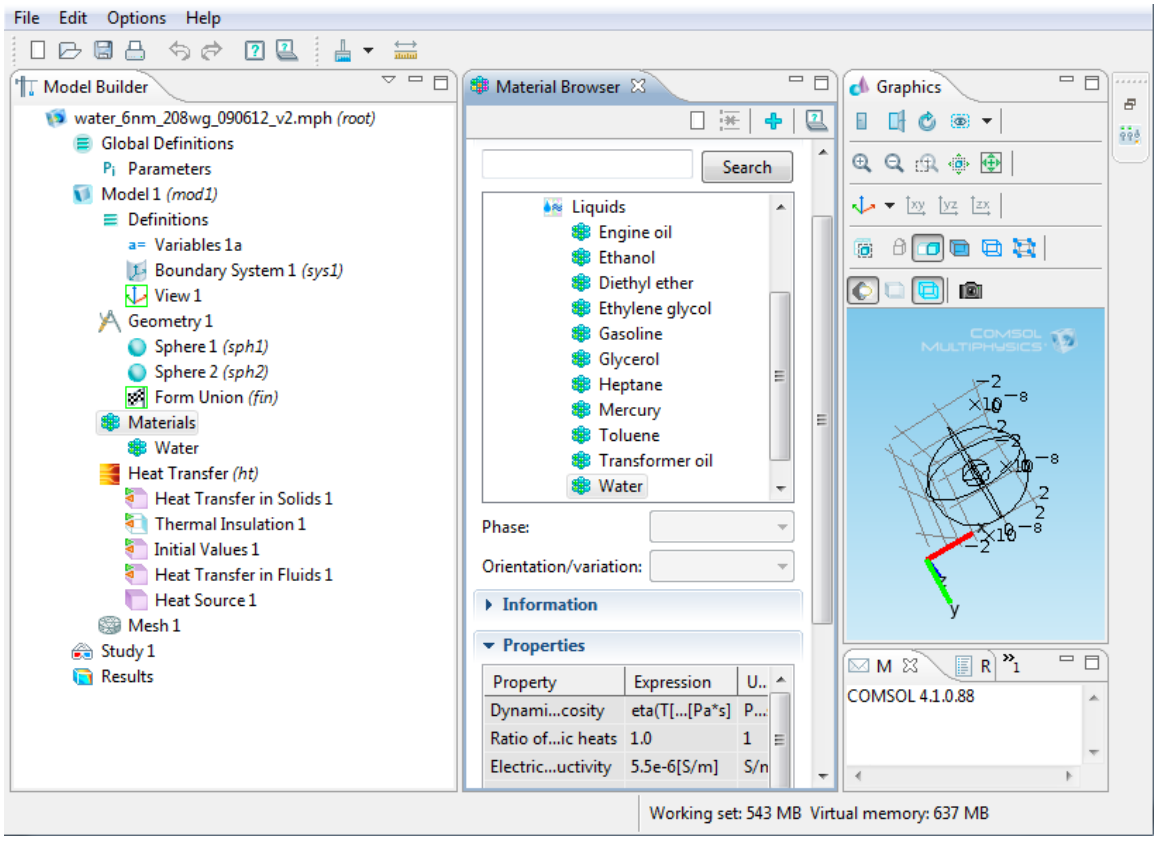

Figure B4–COMSOL Material Browser Library used to add pre-defined materials to models.

Custom materials can also be added to the material library with user defined properties. Properties can also be defined based on functions/expressions and input as custom material properties. COMSOL does not have Magnetite pre-defined in the material library, thus, we will input user defined properties from the parameters list upon defining domains in the next step. To define a domain geometry by a material added to the model, select the material from the Model Builder Menu, then physically select the appropriate domain in the "Graphics" view and right click it. That domain will now be defined by the selected material.

8) Next, the physics and boundary conditions will be defined. The model should already contain the physics for “Heat transfer in solids 1,” “Heat transfer in Fluids 1,” and “Initial Values” based on the initial model selection. Additionally, if it is not already present, right click the “Heat Transfer” tab and add the “Thermal Insulation” boundary condition and the “Heat Source” physics. The thermal insulation boundary condition will be applied to the external fluid sphere surface to describe the no heat-flux condition across this boundary. The heat source physics will be applied to the NP sphere. To define physics for a domain or geometry, click the desired physics from the Model Builder Menu, selected the domain geometry and right click the geometry. The selected physics should now be applied to that domain. For a domain defined by a material that was not input from the material browser, here is where it will be defined by the user. Select the domain, which should now be defined by the appropriate physics; in this case, it will be “Heat Transfer in Solids 1.” As seen in **Fig. B5**, there will be properties still to be defined: the density, thermal conductivity, and specific heat capacity. Select “User defined” from the drop down menu and input the property as defined from the Parameters defined in Step (4).

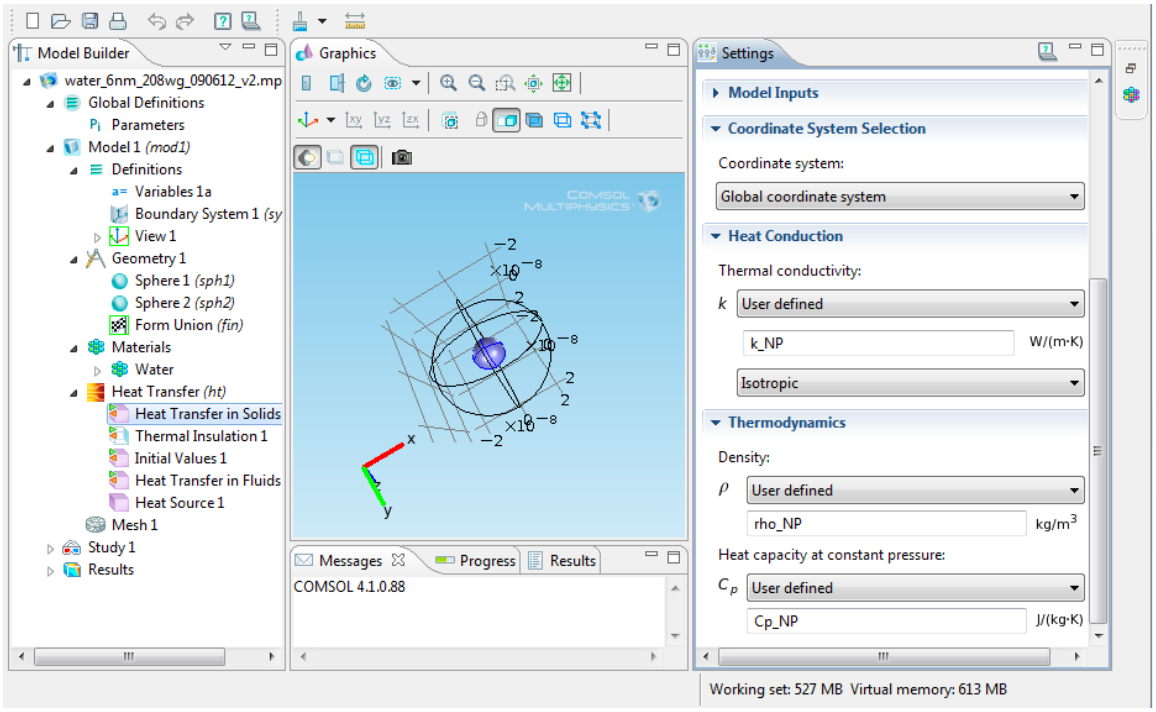

Figure B5–Example of a geometric domain with user defined properties, in this case, the magnetite sphere.

9) Now that the physics and boundary conditions have been defined, the model geometry is ready for meshing. The easiest way to mesh a model geometry is to click the “Mesh” tab from the Model Builder menu, select “Physics-controlled” from the “Sequency type” from down menu, and select a mesh size. Physics-controlled meshing means that COMSOL will automatically insert small size mesh elements near important physics boundaries to improve calculation accuracy. The mesh size can be adjusted based on the model results, and re-meshing can be implemented if refined results are desired. Meshing can be performed on a custom basis by meshing specified geometries or domains separately using a different mesh type; this is not recommended for a novice user as it could inhibit the model from

converging is done improperly. Complicated 3D geometries often encounter meshing issues so this is one of the first places to look if a complicated geometry has convergence issues. A completed triangular, physics-controlled mesh is shown in **Fig. B6**. Only the externtal fluid sphere is visible in this view.

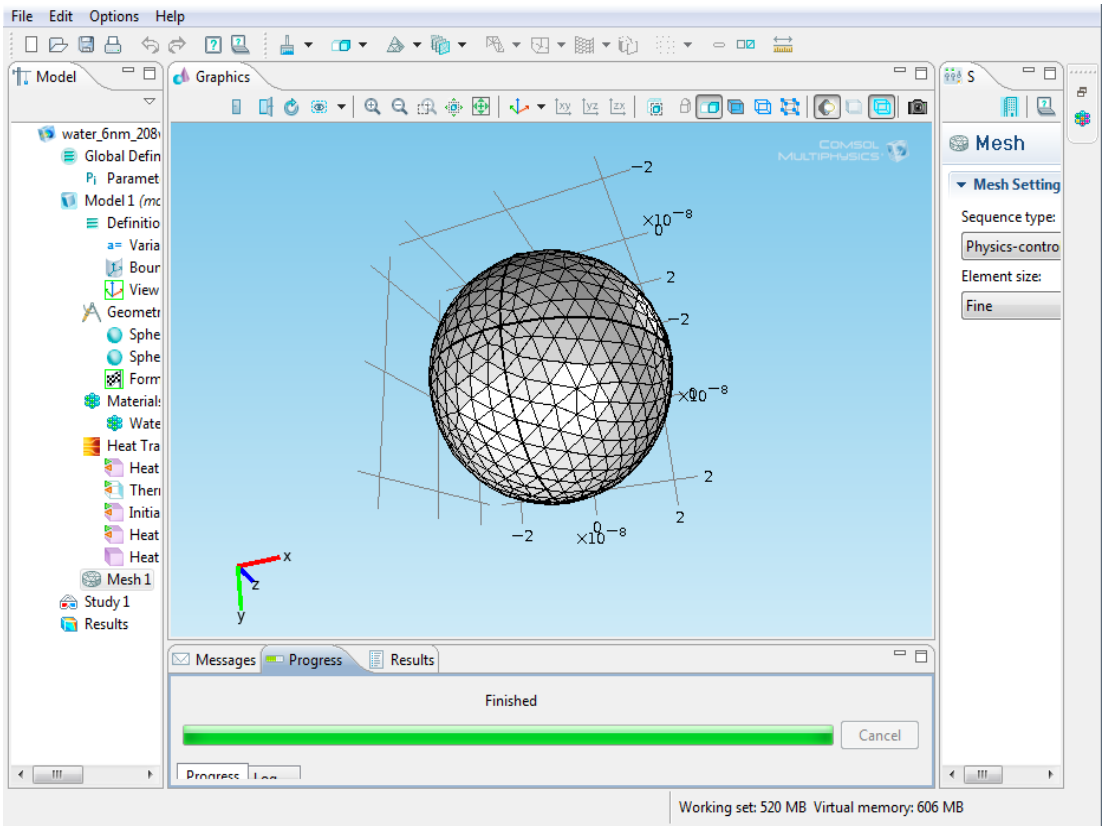

Figure B6–Completed, physics-controlled, triangular meshing of NP dispersion geometry.

10) The model is ready to be simulated. Right click the "Study" tab from the Model Builder menu and select "compute." If a parametric sweep of a parameter is desired, this is that tab where that sweep is defined. Running a

parametric sweep enables COMSOL to run multiple simulations without the user re-executing the simulation for each parameter.

11) Finally, and most importantly, the results can be analyzed. Right click the "Results" tab from the Model Builder menu and add a 1D Plot Group to the results. Next, calculated data needs to be pulled from simulation to plot. Right click the "Data sets" tab and add a Cut Line 3D. in This case, the model is symmetric in all three dimensions, so we're only interested the temperature data that spans from the center of the magnetite sphere to the boundary of the external fluid sphere along a line. Specify the cut line along the *x*-coordinate from 0 to *b* as shown in Fig. B7.

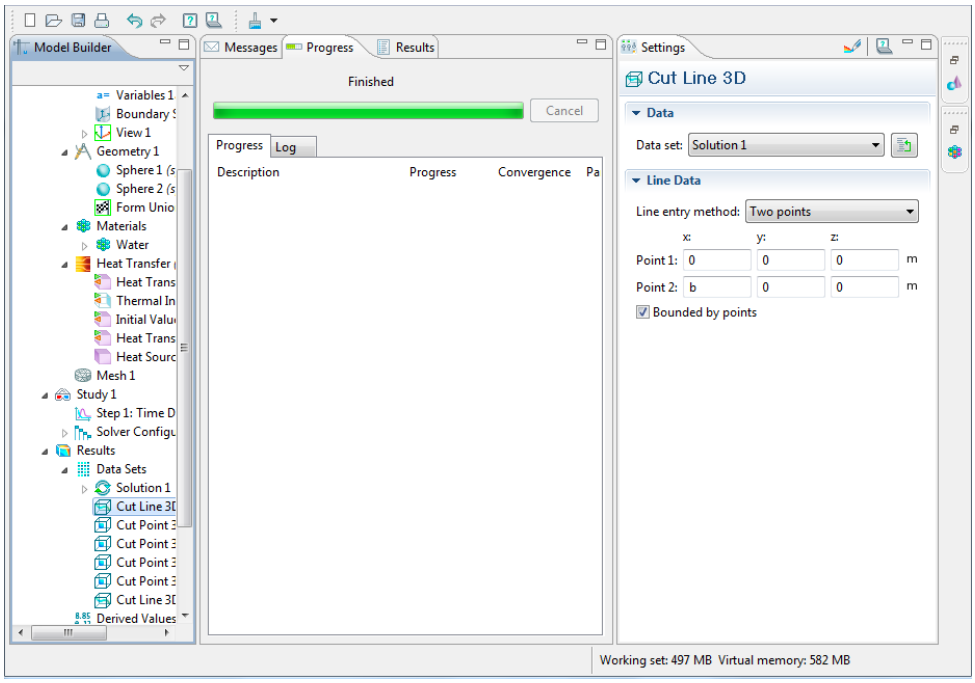

Figure B7–Example of cut line selection from which simulation data is plotted.

Now that the 3D cut line has been defined in the desired location, right click the 1D Plot Group tab added previously, and insert a Point Graph. From the Data Set drop down menu, select the previously made 3D cut line, and for the Expression, select *T* (in this case, we're interested in the radial temperature profile). A plot similar to the one in Fig. B8 will result.

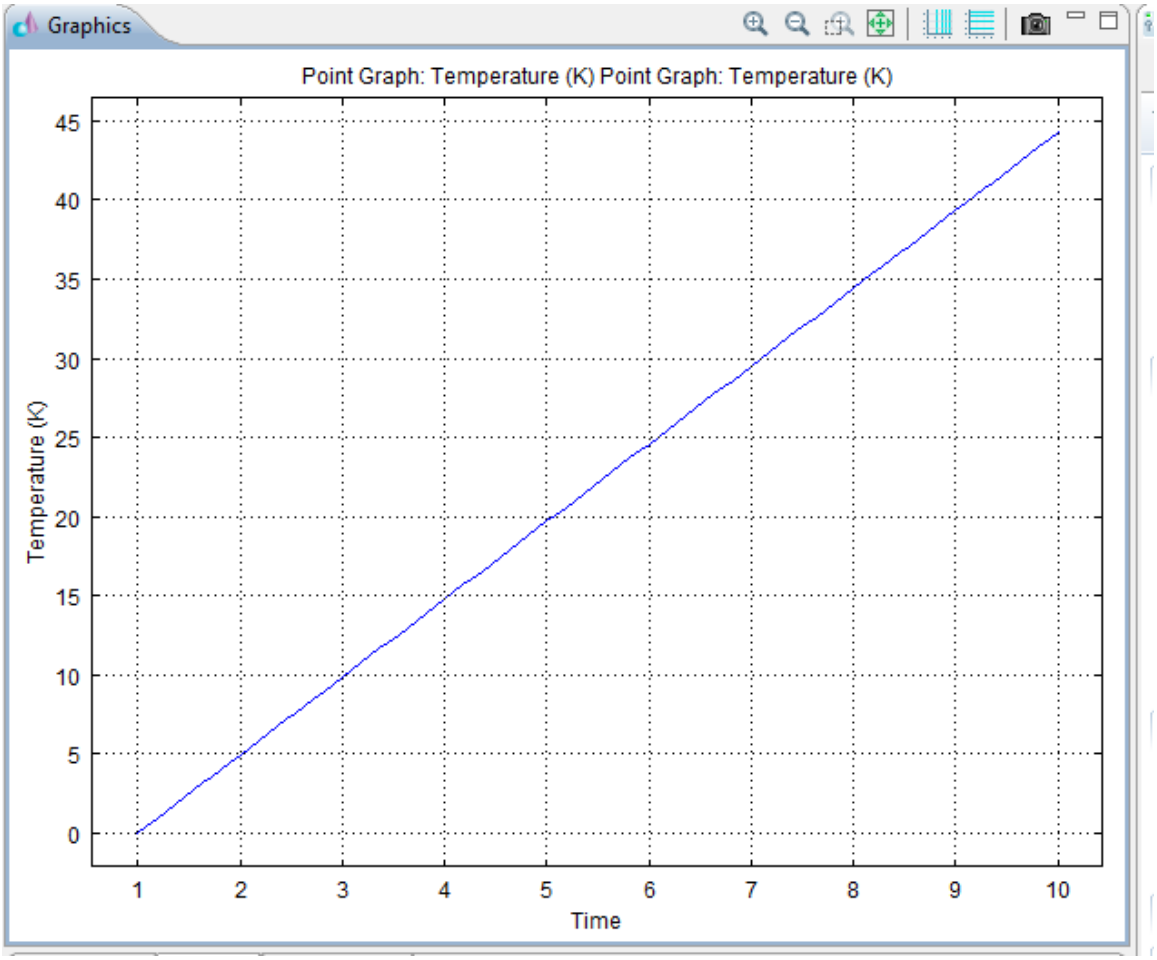

Figure B8–Example temperature vs. time plot of cut line data from the NP dispersion heating model.

Various different variables and expressions can be analyzed and plotted in this manner. Surface plots are also a useful means of visually analyzing data as shown in the modeling portion of this thesis. They can be added to the Results section of the Model Builder in the same manner that the 1D Plot Group was. To export the plotted COMSOL data for additional plotting and analysis in other software such as Excel, right click "Report" from the Model Builder menu and add a Plot. From the Plot Group drop down menu, select the plot with the data that you wish to export, the specific plotted curve, and a file location. The Data format should be set to Spreadsheet for exportation to excel. Now right click the created plot under the Report tab and click export. COMSOL will export the data to a .txt file. The text data can be copied and pasted in to Excel and the Excel data processing tool can be used to split it into columns.

NOMENCLATURE

μ	=	Magnetic permeability, m kg s^{-2} A^{-2}
N	=	Number of coil turns
I	=	Current, A
L	=	Length, m
μ_0	=	magnetic permeability of free space, H m^{-1}
H	=	Magnetic field strength (amplitude), A m^{-1}
M	=	Magnetization, A m^{-1}
B	=	Induced magnetic field, T
E	=	uniaxial anisotropy, kJ
K_v	=	NP volume anisotropy, kJ m^{-3}
V	=	NP volume, m^3
K_s	=	NP surface anisotropy, kJ m^2
SA	=	NP surface area, m^2
τ_N	=	Neel relaxation time constant, s
τ_0	=	Characteristic time constant, s
k_b	=	Boltzmann's constant, m^2 kg s^{-2} K^{-1}
T	=	Temperature, K
τ_m	=	Characteristic magnetization time, s
τ_B	=	Brown relaxation time, s
η	=	Fluid/gel viscosity, Pa s
r_h	=	Hydrodynamic radius, m
τ	=	Effective relaxation time constant, s
U	=	Internal energy, J
H_0	=	Maximum magnetic field strength, A m^{-1}
χ”	=	loss component of magnetic susceptibility
f	=	frequency, Hz
m	=	magnetic moment, A m^2
d_c	=	NP core diameter, m
q	=	Heat flux, W m^{-2}
k	=	thermal conductivity, W m^{-1} K^{-1}
c_p	=	Specific heat capacity, J kg^{-1} K^{-1}
t	=	time, s

Q	=	heat source, W m^{-3}
τ_{yx}	=	shear stress, Pa
p	=	pressure, Pa
σ	=	deviatoric stress tensor, Pa
F	=	body force per unit volume, Pa
D_p	=	NP diameter, nm
w_{Fe3O4}	=	Weight fraction of magnetite in dispersion
SLP	=	Specific loss power of NP, W g^{-1}
SAR	=	Specific absorption rate of fluid, W g^{-1}
ρ	=	density, kg m^{-3}
$\dot{V}$	=	volumetric flow rate, mL s^{-1}
m_{Fe3O4}	=	mass of magnetite, g
R_{NP}	=	NP radius, nm
R_f	=	Fluid radius, nm
k_{NP}	=	NP thermal conductivity, W m^{-1} K^{-1}
k_f	=	fluid thermal conductivity, W m^{-1} K^{-1}
$C_{p,\,NP}$	=	NP specific heat capacity, J g^{-1} K^{-1}
$C_{p,\,f}$	=	Fluid specific heat capacity, J g^{-1} K^{-1}
Q_{NP}	=	NP heat source, W m^{-3}
ρ_{Npaint}	=	Nanopaint density, kg m^{-3}
k_{paint}	=	Nanopaint thermal conductivity, W m^{-1} K^{-1}
$C_{p,paint}$	=	Nanopaint specific heat capacity, J kg^{-1} K^{-1}
T_a	=	Air temperature, K
h_a	=	Convective heat transfer coefficient of air, W m^{-2} K^{-1}
Q_p	=	Nanopaint heat source, W m^{-3}
R_t	=	Nanopainted tube radius, cm
t_w	=	Nanopainted tube wall, cm
t_N	=	Nanopaint thickness, cm
L_N	=	Nanopaint section length in tube, cm
L_t	=	Length of nanopainted tube, cm
u	=	fluid velocity, m s^{-1}
μ_r	=	relative magnetic permeability

E	=	Electric field, V m^{-1}
k_O	=	wave number of free space
ε_r	=	relative electric permittivity
ω	=	angular frequency, Hz
σ	=	Electric conductivity, S m^{-1}
c_O	=	speed of light in a vacuum, m s^{-1}
f_c	=	cutoff frequency, Hz
ε	=	electric perimittivity, m^{-3} kg^{-1} s^4 A^2
a	=	pipe radius, m
R_p	=	Internal pipe radius, m
R_w	=	External pipe radius, m
S	=	Scattering parameter

REFERENCES

Batlle, X., Labarta, A. (2002). Finite-size effects in fine particles: magnetic and transport properties. *Journal of Physics D: Applied Physics*, 35(6), R15-R42.

Bertotti, G. (1998). *Hysteresis in Magnetism.* London: Academic

Bird, R.B., Stewart, W.E., Lightfoot, E.N. (2007). *Transport Phenomena* (Revised Second Edition ed.). John Wiley & Sons.

Callister, W. D., Jr. (2007). Magnetic Materials. In *Materials Science and Engineering: An Introduction*. York, PA: John Wiley and Sons, Inc.

McCabe, W., Smith, J., Harriot, P. (2004) *Unit Operations of Chemical Engineering* (Seventh Edition). McGraw Hill Chemical Engineering Series.

COMSOL Multiphysics (Version 4.1a) [Computer software manual]. (2010). COMSOL AB.

Das, S. (2008). Electro-Magnetic Heating in Viscous Oil Reservoir. Paper SPE 117693 presented at the 2008 SPE International Thermal Operations and Heavy Oil Symposium, 20-23 October.

Fannin, P. C., Kinsella, L., & Charles, S. W. (1999). Wide-band complex magnetic susceptibility measurements of magnetic fluids as a function of temperature. *Journal of Magnetism and Magnetic Materials, 201*, 91 - 94.

Gilchrist, R.K., Medal, R., Shorey, W. D., Hanselman, R. C., Parrot, J. C., Taylor, C. B. (1957). Selective Inductive Heating of Lymph Nodes. *Annals of Surgery*, 146(4), 596-606.

Gubin, S. P. (2009). *Magnetic Nanoparticles*. (Original work published 2009). Wiley-VHC.

Hallouet, B., Wetzel., B., Pelster, R. (2007). On the Dielectric and Magnetic Properties of Nanocomposites. *Journal of Nanomaterials*, 2007.

Hascakir, B., Acar, C., Demiral, B., & Akin, S. (2008). Electro Magnetic Heating in Viscous Oil Reservoir. Paper IPTC 12536 presented at the 2008 International Petroleum Technology Conference, 3-5 December.

Hergt, R., Andra, W., d'Ambly, C. G., Hilger, I., Kaiser, W. A., Richter, U., Schmidt, H. G. (1998). Physical Limits of Hyperthermia Using Magnetite Fine Particles. *IEEE Transactions on Magnetics*, 34(5), 3745-3754.

Hergt, R., Hiergeist, R., Hilger, I., Kaiser, W. A., Lapatnikov, Y., Margel, S., & Richter, U. (2003). Maghemite nanoparticles with very high AC-losses for applications in RF-magnetic hyperthermia. *Journal of Magnetism and Magnetic Materials*, 270, 345-357.

Hergt, R., Dutz, S., Muller, R., Zeisbeger, M. (2006). Magnetic particle hyperthermia: nanoparticle magnetism and materials development for cancer therapy. *Journal of Physics: Condensed Matter*, 18(38), S2919-S2934.

Hergt, R., Dutz, S., & Röder, M. (2008). Effects of size distribution hysteresis losses of magnetic nanoparticles for hyperthermia. *Journal of Physics: Condensed Matter*, 20, 1-12.

Kong, J. A. (1986). *Electromagnetic Wave Theory*. Canda: John Wiley & Sons, Inc.

Kronmuller, H., Fahnle, M. (2003). *Micromagnetism and the Microstructure of Ferromagnetic Solids*. Cambridge:

Cambridge University Press.

Laurent, S., Dutz, S., Hafeli, U. O., Mahmoudi, M. (2011). Magnetic fluid hyperthermia: Focus on superparamagnetic oxide nanoparticles. *Advances in Colloid and Interface Science*, 166 (1-2), 8-23.

Morrish, A.H. (2001). *The physical principles of magnetism*. New York: IEEE Press.

Moskowitz, B. M., Frankel, R. B., Walton, S. A., Dickson, D. P. E., Wong, K. K. W., Douglas, T., Mann, S. (1997) *Journal of Geophysical Research*, 102(B10), 22, 671-22, 680.

Neel, L. (1949). Theorie du trainage magnetique des ferromagnetiques en grains fins avec applications aux terres cuites, *Annals of Geophysiques*, 5, 99-136.

Rosensweig, R. E. (2002). Heating magnetic fluid with alternating magnetic field. *Journal of Magnetism and Magnetic Materials*, 252, 370-374.

Roth, R. F. (2011). Direct Electrical Heating of Flowlines - Guide to Uses and Benefits. Paper OTC 22631 Presented at the 2011 Offshore Technology Conference, 4-6 October.

Roti Roti, J. L., Kampinga, H. H., Malyapa, R. S., Wright, W. D., VanderWaal, R. P., Xu, M. (1998). Nuclear matrix as a target for hyperthermia killing of cancer cells. *Cells Stress Chaperones*, 3(4), 245-255.

Rovers, S. A., van der Poel, L. A., Dietz, C. H., Noijen, J. J., Hoogenboom, R., Kenmere, M. F., Keurentjes, J. T. (2009). Characterization and Magnetic Heating of Commercial Superparamagnetic Irox Oxide Nanoparticles. *Journal of Physical Chemistry*, 113.

Sierra, R., Tripathy, B., Bridges, J. E., & Ali, S. (2001). Promising Progress in Field Application of Reservoir Electrical Heating Methods. Paper SPE 69709 Presented at the SPE International Thermal Operations and Heavy Oil Symposium, 12-14 March.

Urdahl, O., Børnes, A. H., Kinnari, K. J., & Holme, R. (2003). Operational Experience by Applying Direct Electrical Heating for Hydrate Prevention. Paper OTC 15189 Presented at the 2003 Offshore Technology Conference, 5-8 May.